

**PARTICULATE FLOWS AND HETEROAGGREGATION STUDIED BY
OPTICAL IMAGING AND FLUORESCENCE SPECTROSCOPY**

by

KAPIL V. DESHPANDE

A dissertation submitted to the

Graduate School – New Brunswick

Rutgers, The State University of New Jersey

in partial fulfillment of the requirements

for the degree of

Doctor of Philosophy

Graduate Program in Chemical and Biochemical Engineering

written under the direction of

Dr. Nina C. Shapley

and approved by

New Brunswick, New Jersey

January 2014

ABSTRACT OF THE DISSERTATION

Particulate Flows and Heteroaggregation Studied by Optical Imaging

and Fluorescence Spectroscopy

By KAPIL V. DESHPANDE

Dissertation Director:

Dr. Nina C. Shapley

The production of multiscale heteroaggregates of microparticles coated with nanoparticles has generated renewed interest in recent literature due to the wide-ranging applications of such structured particles. These applications include particle stabilization, nanotemplating, and drug delivery, among others. In the past, the majority of heteroaggregation studies and associated applications have involved rigid, spherical particles. However, as part of a multiscale heteroaggregate, hydrophilic hydrogel particles can be used to open a whole range of new applications. These hydrogel particles have also been of great interest recently due to their significant microencapsulation capabilities and variety of delivery mechanisms. This dissertation is focused on gaining understanding of the heteroaggregation of hydrogel microparticles and nanoparticles and of particulate flows that could potentially be used to influence aggregate formation.

First, concentrated noncolloidal particle suspensions undergoing oscillatory torsional flow between parallel plates were studied using optical imaging. Much of the

work focuses on the effect of moderate strain amplitude and frequency on particle migration. Also explored were various effects that can lead to enhanced or reduced particle migration in the flow.

Next, a new quantitative application of fluorescence spectroscopy was developed in order to study the interaction of oppositely charged hydrogel microparticles and nanoparticles in suspensions. Optical microscopy was first used to determine the type of aggregate morphology formed by mixtures of alginate microparticles and fluorescently tagged chitosan nanoparticles at different concentration levels. It was hypothesized that due to fluorophore and particle interaction properties that fluorescence spectroscopy would be able to quantify the boundaries between different types of interactions in the system. With this new technique, the effect of the concentration ratio of nanoparticles to microparticles and the total overall particle concentration was also explored.

Finally, after developing the application of fluorescence spectroscopy for quantifying particle interaction, varying the pH of the interaction environment where heteroaggregation occurs was studied. pH is an important parameter in hydrogel microcapsule and nanocapsule delivery and in heteroaggregation behavior. The change in interaction behavior of alginate and chitosan particles was explored and the capabilities and limits of fluorescence spectroscopy were determined.

Acknowledgements

I would first and foremost like to thank my advisor, Dr. Nina Shapley, for her unwavering support, enthusiastic guidance, and her ability to keep me even-keeled through the best and especially the worst of times. I have known her since my undergraduate days at Columbia University and she has been a constant source of wisdom without which I would not be where I am today. I would also like to thank Dr. Fernando Muzzio for his support and wisdom as well.

I would, then, like to thank the number of friends and colleagues I have had the privilege of getting to know and work with: Athanas Koynov, Sara Koynov, Keirnan LaMarche, Chris Rasmussen, Alisa Vasilenko, Sebastian Vega, Jeff Barminko, and George Dorfman. I would especially like to single out Frank Romanski and Eric Jayjock, not only for their friendship, but for their willingness to help me formulate ideas on how to tackle my research. I would also like to thank my fellow lab mates, Kristin Steeley, Kun Yu, and Shiwen Sun for helping me in my research.

Next, I would like to thank my roommates during the bulk of my graduate school experience: Dominik Naczynski and Dan Duffield. They definitely helped me get through the emotional ups and downs of grad school.

Also, I would like to Dr. Maria Corradini – and by extension Dr. Richard Ludescher – for allowing me to use the fluorescence spectrometer in her lab. Without her accommodations I would not have come close to completing my work. I cannot thank her enough for saving me from the brink.

Finally, I would like to thank the numerous undergraduate and Master's students that I have been able to mentor: David Park, Brett Kuestermeyer, Jennifer Liguori, Nhan Pham, Adam Cham, Louis Ruggieri, Danielle Mazza, Jenna Lo, Eric Somers, and Chinmay Pathak. I would especially like to thank Jonathan Liu and Samyukta Budumuru. I have had the privilege of watching them turn into brilliant researchers and their help on my work has been immeasurable.

Dedication

I dedicate this work to my family who have given me so much love and support through all the years and have given me the strength, wisdom, and ambition I needed to complete my work and get my degree. My parents, Vikas and Padmaja, have consistently been there for me and have never asked for anything in return but I still know I am forever indebted to them for all the time and effort they have spent and still spend on me. My autistic brother, Mandar, has reached points in life he was never supposed to reach and he has always been source of inspiration. My uncle, Milind Pradhan, his wife, Madhura Pradhan, and my cousins, Saaket and Nishant Pradhan have welcomed me into their family and people do not know how lucky I am to be able to have not just one but two families that give me unconditional love and support. Last, but not least, my girlfriend, Denise Wang, has given me so much love and care over our years together that I can only hope that I have the chance to repay her in kind in the future.

Prior Publications

Several sections of this dissertation have been published elsewhere or are being prepared for publication. The following are acknowledged:

- Chapter 2 has been published in full under the citation:

Deshpande, K. V. & Shapley, N. C. 2010. Particle migration in oscillatory torsional flows of concentrated suspensions. *Journal of Rheology*, 54, 663-686.

- Sections of Chapter 3 are being prepared for publication under the citation:

Deshpande, K.V.; Liu, J.; Budumuru, S.; and Shapley, N.C. “Fluorescence spectroscopy characterization of heteroaggregates of alginate microbeads and chitosan nanoparticles.”

Table of Contents

ABSTRACT OF THE DISSERTATION.....	ii
Acknowledgements.....	iv
Dedication.....	vi
Prior Publications.....	vii
Table of Contents.....	viii
List of Tables	xii
List of Figures.....	xiii
Chapter 1 Introduction.....	1
1.1 Motivation.....	2
1.2 Background.....	5
1.2.1 History of Suspension Flows	5
1.2.2 Colloidal Science Theory in Heteroaggregation.....	13
1.2.3 Experimental Studies in Heteroaggregation	15
1.2.4 Micro- and Nanoencapsulation Using Chitosan and Alginate.....	17
1.2.5 Background and Applications of Fluorescence Spectroscopy	20
Chapter 2 Particle Migration in Oscillatory Torsional Flows of Concentrated Suspensions	24

2.1	Introduction.....	25
2.2	Experimental Methods	25
2.2.1	Materials	26
2.2.2	Experimental Apparatus and Procedure.....	27
2.2.3	Fluid Rheology.....	30
2.2.4	Image Analysis.....	32
2.3	Results.....	36
2.3.1	Radial Drift Velocity.....	36
2.3.2	Torque Evolution	40
2.4	Discussion	45
2.4.1	Comparison of Oscillatory and Steady Torsional Flows	46
2.4.2	Comparison with Model Calculations	47
2.4.3	Viscoelastic Effects.....	52
2.4.4	Oscillation Amplitude Effects on Microstructure.....	53
2.5	Summary	56
Chapter 3 Applying Fluorescence Spectroscopy to Distinguish Between		
Particle Interaction Regime Transitions		58
3.1	Introduction.....	59
3.2	Experimental Methods	60
3.2.1	Materials	60

3.2.2 Instrumentation	62
3.2.3 Experimental Procedure.....	63
3.3 Results.....	66
3.3.1 Interaction Regime Boundaries.....	66
3.3.2 Fluorescence Spectroscopy Results	79
3.4 Discussion	91
3.5 Summary	99
Chapter 4 Determining Particle Interaction Regime Boundaries using Fluorescence Spectroscopy at Varying pH.....	101
4.1 Introduction.....	102
4.2 Experimental Methods	102
4.2.1 Materials	102
4.2.2 Experimental Procedure.....	104
4.3 Results and Discussion	105
4.3.1 Fluorescence Spectroscopy Results without Buffers.....	106
4.3.2 Fluorescence Spectroscopy Results with Buffers	115
4.4 Summary	125
Chapter 5 Conclusions and Future Work	127
5.1 Conclusions.....	128
5.2 Future Work	130

References.....132

List of Tables

Table 2.1. Parameters for oscillatory flow experiments.	29
Table 3.1. Levels of chitosan for each sample and corresponding water volumes.....	64
Table 3.2. Levels of alginate and water for each corresponding level of chitosan.....	65
Table 3.3. Comparison of experimental and calculated interaction regime transition boundaries shown as ratio of alginate particles to chitosan particles.	97
Table 4.1. Buffers used to control pH.....	103
Table 4.2. Levels of chitosan for each sample and corresponding buffer volumes.....	105

List of Figures

Figure 1.1. Illustration of pH dependence of FITC reproduced from Johnson (2010).	21
Figure 1.2. Stokes shift of FITC reproduced from Lakowicz (2007).	22
Figure 2.1. Schematic view of the oscillating parallel plate experimental setup.....	28
Figure 2.2 (a) Steady shear rheology of the suspending fluid (solid diamonds) and $\phi_{bulk}=0.4$ particle volume fraction suspension (hollow triangles); (b) Elastic and loss moduli of the suspending fluid at 5% strain amplitude.	32
Figure 2.3. Three images demonstrating radial particle drift during oscillatory flow with strain amplitude = 0.2 and frequency = 0.333 s^{-1} . Particles used for drift velocity calculation are marked A, B, C. The images were acquired (i) 1500 sec; (ii) 6000 sec; (iii) 12,000 sec after the start of oscillatory flow. The radial direction is vertically upward in the images.	33
Figure 2.4. Evolution of radial trajectories of the three particles shown in Figure 2.3 at each time after the start of oscillatory flow. The time axis has the same meaning as in Figure 2.3 above, without any shifting of the origin.....	35
Figure 2.5. Radial drift velocity (a) and radial displacement per cycle (b) as a function of strain amplitude γ_0 , for oscillation frequencies of 0.333 s^{-1} (solid squares) and 1 s^{-1} (hollow squares).....	37
Figure 2.6. Radial drift velocity (a) and radial displacement per cycle (b) as a function of oscillation frequency, strain amplitude $\gamma_0 = 0.415$. In (b), the solid line represents the function $(0.011 / f^2)$ and the dashed line represents the function $(0.013 / f^2 - 0.0001222 / f^4)$	39
Figure 2.7. Normalized torque evolution curve, strain amplitude $\gamma_0 = 1.6$ and frequency = 0.333 s^{-1}	41
Figure 2.8. Normalized torque value (a) as a function of strain amplitude, the ratio of final torque to initial minimum torque for frequency = 0.333 s^{-1} (solid triangles) and 1 s^{-1} (hollow squares), and the ratio of torque at a total strain of 1930 and initial minimum torque for 0.333 s^{-1} (hollow triangles) and 1 s^{-1} (X). The dashed line represents the calculated final torque ratio based on the fully developed concentration profile predicted by the suspension balance model. (b) Final / minimum torque ratio as a function of oscillation frequency, strain amplitude = 0.415.....	44
Figure 2.9. Measured radial drift velocity for oscillation frequencies of 0.333 s^{-1} (solid squares) and 1 s^{-1} (hollow squares), and strain amplitude of 0.415 (stars), compared with the estimated initial migration velocity in steady flow, based on the suspension balance model, at the same average velocities corresponding to the oscillatory flows (solid line).	

The estimated secondary flow velocity for a Newtonian fluid at low Reynolds number in the infinite plate limit (McCoy and Denn, 1971) is also shown (dashed line). 51

Figure 3.1. Microscope image of a sample mixture of 2.31×10^6 (0.05 g) alginate particles and 3.06×10^{10} (6.25 μL) chitosan particles. The sample is in the dispersed, uncoated regime 67

Figure 3.2. Microscope images of sample mixtures of (a) 2.31×10^6 (0.05 g) alginate particles and 6.11×10^{10} (12.5 μL) chitosan particles and (b) 2.31×10^6 (0.05 μL) alginate particles and 1.22×10^{11} (25 μL) chitosan particles. This is the dispersed, uncoated/agglomerated regime boundary. 68

Figure 3.3. Microscope images of sample mixtures of (a) 2.31×10^6 (0.05 g) alginate particles and 9.78×10^{11} (200 μL) chitosan particles and (b) 2.31×10^6 (0.05 g) alginate particles and 1.96×10^{11} (400 μL) chitosan particles. This is the agglomerated/dispersed, coated interaction regime boundary. 70

Figure 3.4. Microscope images of samples mixtures of (a) 2.31×10^6 (0.05 g) alginate particles and 3.91×10^{12} (800 μL) chitosan particles and (b) 2.31×10^6 (0.05 g) alginate particles and 7.82×10^{12} (1600 μL). The samples are in the dispersed, coated interaction regime. 71

Figure 3.5. Microscope images of sample mixtures of (a) 4.63×10^6 (0.1 g) alginate particles and 1.22×10^{11} (25 μL) chitosan particles and (b) 4.63×10^6 (0.1 g) alginate particles and 2.44×10^{11} (50 μL) chitosan particles. This is the dispersed, uncoated/agglomerated interaction regime boundary. 73

Figure 3.6. Microscope images of sample mixtures of (a) 4.63×10^6 (0.1 g) alginate particles and 1.96×10^{12} (400 μL) chitosan particles and (b) 4.63×10^6 (0.1 g) alginate particles and 3.91×10^{12} (800 μL) chitosan particles. This is the dispersed agglomerated/dispersed, coated interaction regime boundary. 74

Figure 3.7 Microscope image of a sample mixture of 9.26×10^6 (0.2 g) alginate particles and 1.22×10^{11} (25 μL) chitosan particles. The sample is in the dispersed, uncoated interaction regime. 75

Figure 3.8. Microscope images of sample mixtures of (a) 9.26×10^6 (0.2 g) alginate particles and 2.44×10^{11} (50 μL) chitosan particles and (b) 9.26×10^6 (0.2 g) alginate particles and 4.89×10^{11} (100 μL) chitosan particles. This is the dispersed, uncoated/agglomerated interaction regime boundary. 76

Figure 3.9. Microscope images of sample mixtures of (a) 9.26×10^6 (0.2 g) alginate particles and 3.91×10^{12} (800 μL) chitosan particles and (b) 9.26×10^6 (0.2 g) alginate particles and 7.82×10^{12} (1600 μL) chitosan particles. This is the agglomerated/dispersed, coated interaction regime boundary. 78

Figure 3.10. Resulting interaction regime diagram from experiments. 78

Figure 3.11. (a) Initial re-zeroed raw spectrum data for sample 4.36×10^6 (0.1 g) alginate particles and 1.96×10^{12} (400 μ L) chitosan particles. (b) The zoomed in region from 500-650 nm.	80
Figure 3.12. Re-zeroed raw spectrum data for new batch of FITC tagged chitosan particles at a level of 4.36×10^6 (0.1 g) alginate particles and a level of (a) 1.96×10^{12} (400 μ L) chitosan particles. (b) The zoomed in region from 500-650 nm.	81
Figure 3.13. Raw spectrum data for sample 4.36×10^6 (0.1 g) alginate particles and 1.96×10^{12} (400 μ L) chitosan particles.....	82
Figure 3.14. The average intensity integral from the maximum intensity to the half maximum intensity for each constant alginate level plotted against the number chitosan particles.	83
Figure 3.15. Average maximum to half maximum intensity integral plotted against the ratio of alginate to chitosan particles for constant alginate levels with the points for the interaction regime transitions from dispersed, coated to agglomerated (dashed) and agglomerated to dispersed, uncoated (solid) circled.....	85
Figure 3.16. Average maximum to half maximum intensity integral plotted against the ratio of alginate to chitosan particles for constant chitosan levels. The dispersed, coated regime (—), the agglomerated regime (...), and the dispersed, uncoated regime (—■) are circled.....	86
Figure 3.17. Average maximum to half maximum intensity integral normalized to zero alginate value plotted against the ratio of alginate to chitosan particles for constant chitosan levels.....	89
Figure 3.18. Normalized maximum to half maximum intensity integral plot	90
Figure 3.19. Plot of the slope of the maximum intensity to half maximum intensity integral curve from chitosan level to chitosan level.	91
Figure 3.20. DLVO curves for (a) two interacting covered alginate particles and (b) two interacting chitosan particles.....	96
Figure 4.1. Illustration of the integral from the maximum intensity to the half maximum intensity.....	106
Figure 4.2. (a) Average intensity integral from maximum intensity to half maximum intensity for each pH plotted against number of chitosan particles at an alginate level of 4.63×10^6 (0.1 g) particles. (b) Normalized average intensity integral from maximum intensity to half maximum intensity for each pH plotted against number of chitosan particles at an alginate level of 4.63×10^6 (0.1 g) particles.	107
Figure 4.3. Slope of the normalized average intensity integral from maximum intensity to half maximum intensity curve from each chitosan level to level for each pH without a buffer.....	108

Figure 4.4. Microscope image of 4.63×10^6 (0.1 g) alginate particles and 9.78×10^{11} (200 μL) chitosan particles at pH 2.3.....	109
Figure 4.5. Microscope images of 4.63×10^6 (0.1 g) alginate particles and (a) 3.91×10^{12} (800 μL) and (b) 1.56×10^{13} (3200 μL) chitosan particles at a pH of 2.3. The samples are in the agglomerated regime.....	110
Figure 4.6. Microscope images of 4.63×10^6 (0.1 g) alginate particles and (a) 3.91×10^{12} (800 μL) and (b) 7.82×10^{12} (1600 μL) chitosan particles at a pH of 3.5. This the agglomerated/dispersed, coated regime.	112
Figure 4.7. Microscope images of 4.63×10^6 (0.1 g) alginate particles and (a) 1.96×10^{12} (400 μL) chitosan particles and (b) 3.91×10^{12} (800 μL) at a pH of 4.8. This is the potential agglomerated/dispersed, coated interaction regime boundary.....	113
Figure 4.8. Microscope image of 4.63×10^6 (0.1 g) alginate particles and (a) 7.82×10^{12} (1600 μL) chitosan particles. The sample is in the dispersed interaction regime.....	114
Figure 4.9. (a) Average intensity integral from maximum intensity to half maximum intensity for each pH plotted against number of chitosan particles at an alginate level of 4.63×10^6 (0.1 g) particles. (b) Normalized average intensity integral from maximum intensity to half maximum intensity for each pH plotted against number of chitosan particles at an alginate level of 4.63×10^6 (0.1 g) particles.	116
Figure 4.10. Slope of the normalized average intensity integral from maximum intensity to half maximum intensity curve from each chitosan level to level for each pH with a buffer.....	117
Figure 4.11. Microscope images of 4.63×10^6 (0.1 g) alginate particles and (a) 3.91×10^{12} (800 μL) and (b) 1.56×10^{13} (3200 μL) chitosan particles in a pH 2.2 0.2 M glycine/0.2 M HCl buffer.	119
Figure 4.12. Microscope image of 4.63×10^6 (0.1 g) alginate particles and 3.91×10^{12} (800 μL) chitosan particles in pH 2.8 0.2 M glycine/0.2 M HCl buffer.	120
Figure 4.13. Microscope images of 4.63×10^6 (0.1 g) alginate particles and (a) 7.82×10^{12} (1600 μL) and (b) 1.56×10^{13} (3200 μL) chitosan particles in a pH 2.8 0.2 M glycine/0.2 M HCl buffer. This marks an interaction regime transition from agglomerated to dispersed, coated.	121
Figure 4.14. Microscope imagees of 4.63×10^6 (0.1 g) alginate particles and (a) 3.91×10^{12} (800 μL) and (b) 1.56×10^{13} (3200 μL) chitosan particles in a pH 3.5 0.2 M glycine/0.2 M HCl buffer.	123
Figure 4.15. Microscope images of 4.63×10^6 (0.1 g) alginate particles and 7.82×10^{12} (1600 μL) chitosan particles in (a) pH 4.8 and (b) pH 5.6 0.2 M acetic acid/0.2 M sodium acetate buffer.....	124

Chapter 1

Introduction

1.1 Motivation

The aggregation of dissimilar types of particles has been a long studied phenomenon in the field of colloid science. There has been a recent renewed interest in the phenomenon as pertaining to interactions between microparticles and nanoparticles in aqueous solutions. In particular, the renewed interest focuses on heteroaggregates, in which the surface of each freely suspended microparticle is coated with a layer of nanoparticles (Mohraz et al., 2008, Tohver et al., 2001a). The applications of microparticles coated with nanoparticles are quite widespread. They can be used as particle stabilizers (Tohver et al., 2001b). In environmental applications they can be used for water purification as flocculating agents or for encapsulating harmful toxins (Yu et al., 2013). The microparticles that the nanoparticles coat can be used for nanotemplating (Zubitur et al., 2009). They can also be used in pharmaceuticals as a drug delivery application (Agnihotri et al., 2004).

Previous studies of heteroaggregation have typically involved rigid spherical particles, where at least one particle type is strongly hydrophobic (e.g. polystyrene). In contrast, the model system examined in this study consists of hydrophilic hydrogel particles which are soft and strongly oppositely charged. Interactions between hydrogel microcapsules and nanocapsules have typically not been studied in depth. In this system, there is a different balance of colloidal interactions compared to the typical system studied previously. Electrostatic interactions between alginate hydrogel microparticles and chitosan hydrogel nanoparticles tend to be large compared to van der Waals interactions, which is the opposite of the usual situation. In addition, there is current

great interest in alginate and chitosan as biocompatible and naturally abundant materials, with potentially sustainable applications in food, pharmaceuticals and environmental processes.

In terms of pharmaceutical technology, hydrogel microcapsules and nanocapsules are of particular interest because of the possibility of triggered delivery mechanisms. They can have pH dependent release of payloads (Agnihotri et al., 2004). Temperature can also be used for release (Ichikawa and Fukumori, 2000). A certain level of mechanical shear can be required to rupture the capsule (Zanina et al., 2002). Even a set time can be used as a factor to control release where the payload is released over a designated time frame (Stein et al., 2006). It can even be envisioned that heteroaggregates of microparticulates and nanoparticulates, particularly microcapsules coated by nanocapsules, can be utilized for novel controlled release systems. For example, the nanocapsules (or microcapsules) can be triggered to release a payload by the methods listed above, which in turn triggers the other capsule to release its payload. However, before studying such a complex hydrogel system properly, one needs to understand heteroaggregation behavior in detail.

The goal of this thesis is to gain understanding regarding the heteroaggregation of hydrogel microparticles and nanoparticles and regarding particulate flows that could be used to influence aggregate formation. The operating conditions at which interaction regime transitions between distinct heteroaggregate morphologies occur in batch systems were determined, in terms of the concentration of microparticles and nanoparticles, the solution pH, and the ionic strength of the solution. Experimental measurements of particulate flows and heteroaggregation in batch systems were obtained by using optical

imaging and fluorescence spectroscopy. A detailed discussion of the experimental procedures, results and analysis follows this introductory chapter, as described below.

In Chapter 2, highly loaded suspensions of large colloidal particles were studied under oscillatory shear flow. The aim was to enhance understanding of the rheology of concentrated suspensions resulting from the particle microstructure formed during oscillatory flow. The results of this flow study could potentially be used to create a better yield of microparticles coated by nanoparticles as the coating is hampered at higher concentrations in static systems.

In Chapter 3, a new, quantitative fluorescence spectroscopy method was developed to study the interaction behavior of oppositely charged hydrogel microparticles and nanoparticles. Most of the previous studies involving heteroaggregates of oppositely charged microparticles and nanoparticles have used optical microscopy to observe the variation of aggregate morphologies with operating conditions. However, optical microscopy has two major limitations under some circumstances, due to the fact that a sample must be extracted from the particulate suspension and placed on a microscope slide for suitable visualization. First, microscopy cannot be performed *in situ* or in real time in a vial or in a flow. Also, the extracted sample may not have a composition identical to the particulate suspension, and may therefore reflect different operating conditions, leading to a different aggregate morphology observed compared to that present in the particulate suspension. Therefore, fluorescence spectroscopy, which is not constrained by the same limitations, was applied to study the heteroaggregation behavior of a simple model system of alginate microparticles and chitosan nanoparticles. The system was observed over a range of microparticle and nanoparticle concentrations in

order to map the aggregate morphology interaction regime boundaries and validate the fluorescence spectroscopy measurements against optical microscope images.

Subsequently, in Chapter 4, after developing the fluorescence spectroscopy method, changing the pH of the interaction environment where heteroaggregates were formed was studied. pH variation is an important factor for orally ingested microcapsules and nanocapsules. By varying the pH of the suspending solution, a new parameter affecting the heteroaggregation behavior can be studied and also the viability of fluorescence spectroscopy within the low pH environment can be tested. The solution ionic strength was also varied by comparing results from buffered and unbuffered solutions. In Chapter 5, conclusions and potential future work are discussed.

1.2 Background

In order to understand where the work fits into a historical context, first a history of suspension flows is examined. Then a background on colloidal science theory and how it forms the basis of heteroaggregation studies is explored. Also, a snapshot of the experimental work in heteroaggregation behavior is provided. Then the use of alginate and chitosan in encapsulation is described. Finally, there is a general background on fluorescence spectroscopy and its applications in order to show how it can have other applications like the one being developed in this work.

1.2.1 History of Suspension Flows

Shear flow between rotating parallel plates is typically used to measure rheological data for fluids with suspended solid particles. As the particle concentration increases, the flow behavior becomes more complex due to the high frequency of particle interactions, and may potentially include nonuniform particle distributions or ordered structure formation. The majority of flow studies concerning suspensions of neutrally buoyant, noncolloidal spheres in viscous Newtonian liquids focus on unidirectional shear flows, such as concentric cylinder Couette cells (Abbott et al., 1991, Breedveld et al., 1998, Chow et al., 1994), circular pipes (Hampton et al., 1997, Han et al., 1999), and rectangular channels (Koh et al., 1994, Lyon and Leal, 1998). Gadala-Maria and Acrivos (1980) first discovered that for concentrated noncolloidal suspensions of neutrally buoyant particles the apparent viscosity changed as they were sheared in a Couette cell. Leighton and Acrivos (1987) demonstrated that the viscosity change was caused by shear-induced particle migration, where particles that are initially uniformly distributed are driven into a nonuniform spatial configuration by flow inhomogeneities. In addition, suspension researchers have recognized the need for model calculations and experimental data obtained from complex geometries (Altobelli et al., 1997, Corbett et al., 1995, Miller and Morris, 2006, Moraczewski and Shapley, 2006, 2007, Moraczewski et al., 2005, Rao et al., 2007, Rao et al., 2002, Subia et al., 1998, Xi and Shapley, 2008) and evolving flows (Ingber et al., 2009, Miller and Morris, 2006, Stickel et al., 2007) in order to gain more insight into particle dynamics when the shear stress has multiple components and to provide more challenging tests for the predictions of existing suspension flow models.

Torsional flow of suspensions in rotating parallel plate geometries seems to be a simple viscometric flow, yet has been less well understood than the thoroughly studied

unidirectional flows where the velocity only varies with a single coordinate. The rotating parallel plate geometry is typically used to determine the rheology of suspensions. Therefore, sufficient understanding of the complexities of suspension behavior in this flow is needed to properly interpret the data. For example, the partially filled horizontal concentric cylinder Couette device would be expected to generate a planar flow and yet for suspensions produces striking, symmetry-breaking concentration bands and corresponding convection patterns along the axial direction (Jin and Acrivos, 2004, Tirumkudulu et al., 1999).

Initial measurements in the rotating parallel plate geometry indicated that shear-induced migration did not occur in steady torsional flow of a monodisperse suspension with a Newtonian suspending fluid, and the particles remained uniformly distributed (Chan and Powell, 1984, Chapman, 1990, Chow et al., 1994). Chow *et al.* (1994) used nuclear magnetic resonance imaging (NMRI) to study steady torsional flow for Newtonian suspending fluids. They found that for a bulk particle volume fraction $\phi_{bulk}=0.5$ suspension in the parallel plate geometry there was no detectable inhomogeneity in the particle distribution at steady state but there was a change in the apparent viscosity as shearing progressed. The optical imaging measurements of Chapman (1990) and rheological measurements at lower concentrations ($\phi_{bulk}=0.1$ to 0.3) of Chan and Powell (1984) supported the findings of Chow *et al.* (1994), where a uniform distribution of particles was observed.

At the time, the observed lack of radial migration was unexpected, because the diffusive flux model (Phillips et al., 1992) predicted that particles would migrate radially inward toward low shear rate regions of the flow. Further exploration of bidisperse

suspensions by Krishnan *et al.* (1996) suggested that a flux arising from the curved streamlines opposed the shear rate gradient flux for a monodisperse suspension, and that marked particle size separation occurred in bidisperse suspensions. (Krishnan *et al.*, 1996) The concept of a curvature or normal stress difference driven flux leading to the absence of migration in steady torsional flow of monodisperse suspensions is a concept incorporated into multiple suspension models and used to fit model coefficients (Fang *et al.*, 2002, Krishnan *et al.*, 1996, Morris and Boulay, 1999).

Recently, another shift occurred in the understanding of phenomena taking place in the rotating parallel plate geometry for concentrated suspensions. Reports of observations of outward radial particle migration during steady flow started to appear in the literature. Merhi *et al.* (2005) used light absorption techniques with tracer particles to reveal outward radial migration under steady shear conditions for a suspension of 0.4 bulk particle volume fraction. Similar results were found by Kim *et al.* (2008). Kim *et al.* (2008) developed a modified diffusive flux and curvature flux model that predicted outward radial particle migration up to 50% bulk solids loading, and showed good agreement with their experimental video imaging observations of steady torsional flow. Kim *et al.* (2008) explained how their work resolves some of the discrepancies between previous and current measurements in steady torsional flow. Kim *et al.* (2008) found that radially outward particle migration in steady torsional flow is more apparent at lower bulk particle concentrations, with dramatic concentration gradients at bulk particle volume fractions of 0.1 to 0.25. However, the extent of radial migration decreases with the bulk concentration, so that the extent of migration at $\phi_{bulk}=0.5$ is essentially negligible. Since the earlier measurements (e.g. (Chapman, 1990, Chow *et al.*, 1994)

involved suspensions with $\phi_{bulk}=0.5$, it is not surprising that no migration was observed. In the more recent measurements at a lower concentration of $\phi_{bulk}=0.4$, radially outward migration is apparent. Ramachandran and Leighton (2008) also showed that when the experimental measurements of Zarraga *et al.* (2000) are substituted directly into the stress components in the suspension balance model of Morris and Boulay (1999), the model predicts slight outward migration in steady torsional flow of a suspension with bulk particle volume fraction of 0.4 (Ramachandran and Leighton, 2008). Ramachandran (2007) also determined that suspension loading procedures in the parallel plate geometry can introduce significant concentration nonuniformities that may be the main driving force for migration in torsional flow. The recent studies are likely to be incorporated into a new prevailing view of suspension behavior.

There have also been interesting findings for steady torsional flows with non-Newtonian suspending fluids. Feng and Joseph (1996) found that for dilute concentrations of particles in viscoelastic fluids (aqueous solutions of polyethylene oxide) under steady shear in a rotating parallel plate geometry that chaining and outward migration takes place, except at low polymer concentration, where slow inward particle migration occurs for a single sphere. As in their study of suspensions with Newtonian suspending liquids in torsional flow, Kim *et al.* (2001) observed radially outward particle migration taking place for solids loading of $\phi_{bulk}=0.1$ to 0.3 in a highly elastic Boger fluid, where the particles form an annulus near the outer edge at steady state, but found no detectable migration in $\phi_{bulk}=0.5$ particle volume fraction suspension in the same geometry.

In addition to steady state suspension measurements, both shear reversal and oscillatory flow experiments have provided a wealth of data regarding particle microstructure in a suspension. Multiple experimental and simulation studies (Breedveld *et al.*, 2001, Butler *et al.*, 1999, Morris, 2001, Pine *et al.*, 2005) have found that after experiencing a strain of approximately 2 or 3 units, the suspension has formed the steady state microstructure with enhanced contact between particles along the compression direction. Based on the work of Gadala-Maria and Acrivos (1980), Kolli *et al.* (2002) and Narumi *et al.* (2002), the stress shows a net increase, after a brief initial decrease, during the transition from a uniform state to the steady state microstructure during shear reversal experiments. Narumi *et al.* (2005) also studied oscillatory flow of suspensions in the cone and plate geometry. They recorded a transient response followed by a purely viscous response during each oscillation. They accounted for this phenomenon by surmising that microstructural rearrangements of the particles accounted for the transient portion of the response.

According to the work of Heymann *et al.* (2002) in a cone and plate geometry, the oscillatory stress amplitudes examined here likely fall in the nonlinear transition region between Hookean behavior at small amplitude and a constant viscosity region at large amplitude. At the low end of the strain amplitude range, Breedveld *et al.* (2001) observed low viscosity values corresponding to a nearly isotropic microstructure in concentric cylinder Couette flow, accompanied by an abrupt viscosity increase to the steady shear viscosity value at higher strain amplitudes. They interpreted these rheology results to indicate that at small strain amplitudes, the particles are confined to a “cage” consisting of neighboring particles, but that the cage breaks open over a range of transition strain

amplitudes so that at large oscillatory strain amplitudes (> 2 units) the suspension exhibits the same viscosity value as in steady shear (Breedveld *et al.*, 2001). In a subsequent study, Pine *et al.* (2005) found a minimum strain amplitude value of approximately 0.8 units at $\phi_{bulk} = 0.4$ for irreversible particle interactions leading to nonzero particle diffusivity in concentric cylinder Couette flow (Pine *et al.*, 2005), thus supporting the argument of Breedveld *et al.* (2001).

Bricker and Butler (2006, 2007) extensively studied oscillatory flow of suspensions between rotating parallel plates as well as concentric cylinders. They showed experimentally and computationally that for oscillatory flow irreversible behavior dependent on the strain amplitude occurs, indicated by an increase or decrease of the apparent complex viscosity over time during oscillatory shear. Experimentally, Bricker and Butler (2006) varied the oscillatory strain amplitude and held the oscillation frequency constant at $f = 1.59 \text{ s}^{-1}$. They observed a distinct minimum value in the apparent complex viscosity at intermediate strain amplitudes, and attributed the phenomenon to microstructural rearrangement during evolution of the oscillatory flow. In a subsequent study involving Stokesian Dynamics simulations, Bricker and Butler (2007) elucidated the microstructures that form at small, intermediate, and large oscillatory strain amplitudes. In moderate amplitude flows, in the same range as the ones we studied here, they found that the particles formed independent layers parallel to the direction of the flow. In small amplitude flows, which are also incorporated into our studies, they found that particles develop a crystal-like solid state microstructure, with close-packed structures. At large strain amplitudes, the system exhibits the steady state suspension microstructure, with particles aligned in clusters along the compression direction of flow.

The experimental system of Bricker and Butler (2006, 2007) is most similar to our system of all the torsional flow suspension systems investigated to date, in terms of the particle properties, flow geometry and operating parameters selected.

Other previous studies have associated oscillatory flow and ordering of particles. For example, Gondret and Petit (1996) observed an ordered cubic particle structure to form in linear oscillatory flow of concentrated suspensions at $\phi_{bulk}=0.2$ and a strain amplitude of 0.1, along with a 25% decrease in the viscosity (Gondret and Petit, 1996). Gondret and Petit (1996) observed a viscosity decrease of comparable proportions for a bulk particle volume fraction of 0.4. In earlier work, Petit and Gondret (1995, 1992) proposed that the ordered structuring arises from stationary secondary flow due to oscillating boundary layers, and also developed scaling relationships for the rate of structure development. The ordering of particles under oscillatory shear is corroborated by other studies of particle jamming and release (Knipmeyer and Pine, 2003) where jamming was associated with a disordered microstructure and re-establishment of flow with an ordered microstructure. Calculations from a recent continuum model (Yapici et al., 2009) suggest that particle ordering occurs during small amplitude oscillatory channel flow because of an increase in the average particle separation distance to a value greater than that for randomly arranged particles.

A final effect that could occur in oscillatory torsional flow is “reverse” particle migration in the opposite direction to that observed for steady shear flow. Such a phenomenon has been observed in small amplitude, pressure-driven oscillatory flows, both in Stokesian Dynamics simulations (Morris, 2001) and continuum modeling (Yapici et al., 2009) in a planar channel and also nuclear magnetic resonance imaging (NMRI)

experimental measurements in a circular tube (Butler et al., 1999). In such systems, particles are observed to migrate laterally away from the channel or tube center and toward the wall, causing a high particle concentration band or ring to form near the wall at steady state. Since the “reverse” migration occurred along the velocity gradient direction for pressure driven flows, it is not known whether a similar effect is present along the neutral (radial) direction in torsional flow between rotating parallel plates.

1.2.2 Colloidal Science Theory in Heteroaggregation

The reversible and irreversible attraction between dissimilar types of particles is a topic of much scientific interest. This phenomenon is of interest in terms of suspension stability or even destabilizing of suspensions. The terms seen in the literature for particle mixtures aggregating together are heteroassociation, heteroflocculation, heterocoagulation, and heteroaggregation. Heteroassociation and heteroflocculation are interchangeable terms describing reversible or temporary particle aggregation. Heterocoagulation refers to irreversible aggregation. Heteroaggregation is the general term for particle aggregation that all of the previous terms can fit under although heterocoagulation is also sometimes used as general term (Islam et al., 1995).

Much of the early work conducted in heteroaggregation was based on the colloidal theory of Derjaguin, Landau, Verwey, and Overbeek (DLVO). DLVO at its simplest form calculates the interaction potential between particles by adding the interaction potential energy due to the electrostatic interactions and the interaction potential energy due to van der Waals forces (Derjaguin and Landau, 1941, Verwey and

Overbeek, 1948). DLVO sufficiently describes a process known as homoaggregation or aggregation between like particles but these equations, however, do not adequately describe particulate colloids. First, they do not take into account differences in particle properties (Bell and Peterson, 1972, Furusawa and Anzai, 1992, Sasaki et al., 1980, Stoll and Pefferkorn, 1993, Vincent et al., 1978).

Also, there is the possibility of solvent based forces which Hunter calls “solvent structural forces” (1987). The two types of solvent interactions are hydration forces and hydrodynamic interactions. Hydration forces are due to the water molecules forming hydrogen bonds with the ionic groups on the surface of a molecule (Gregory, 1988). When two such particles interact at distance of less than 10 nm and greater than 1 nm, a repulsive force arises equal to the amount of energy needed to remove the water molecule from the surface to the bulk. These usually produce minimal deviations in the colloidal interactions (Pashley and Israelachvili, 1984). Hydrodynamic interactions are repulsive forces that arise from slow drainage of fluid from in between two interacting particles. The size of the particles and the distance between them impacts how much hydrodynamic forces affect interaction potentials (Greene et al., 1994). Where shear flow is occurring in a mixture of dissimilar particles, the hydrodynamic repulsion is greater and also has an effect on particle collision rate (Valioulis and List, 1984, Wang, 1992).

Studies on mixed colloidal dispersions usually look at the kinetics of destabilization (Derjaguin, 1954, Hogg et al., 1966, Kihira et al., 1992). Coagulation rate can be described by the energy barrier that particles reach during collision (Wiese and Healy, 1970). Studies initially involved Brownian motion but most heteroaggregation systems usually involve some sort of agitation, flow, and/or sedimentation (Wang, 1992).

The simplest heterocoagulation equations are the Hogg-Healy-Fuerstenau (HHF) equations. They use the Derjaguin approximation which assumes lower surface potentials and an effective Debye length smaller than the particle size. These equations are valid for constant surface potentials (Islam et al., 1995). More complex equations have been developed that account for what are called attractive depletion forces (Vesaratchanon et al., 2007).

Finally, work that describes the structure of heteroaggregates that can form is done with numerical simulations that account for possible particle-particle interactions. There are two limiting regimes that are considered in simulations: diffusion limited cluster aggregation (DLCA) and reaction limited cluster aggregation (RLCA) (Lopez-Lopez et al., 2006). In DLCA every collision results in the formation of a bond and in RLCA a large number of collisions are needed in order to form a bond. RLCA is difficult to simulate due to the lack of agreement on a general kinetic theory (Islam et al., 1995). There were three interesting findings from DLCA simulations of oppositely charged particles of the same size. One finding was that charged clusters can aggregate with neutral clusters but as they aggregate with more neutral clusters they tend to vanish. Also, neutral clusters are formed only when two neutral or two oppositely charged clusters aggregate. Finally, two clusters of the same charge cannot aggregate (Puertas et al., 2002).

1.2.3 Experimental Studies in Heteroaggregation

Many early experimental studies looked to test different particulate materials and see how they compared to colloidal models. Cooper, et al. investigated the interactions of two graphitized carbon blacks: Graphon and Sterling MTG. They found that their experimental observations agreed with those predicted by the HHF theory (1973). This study did not explore varying surface potentials. Thus, more studies were done using mineral oxides since the surface potential can be varied by changing pH. Wiese and Healy completed a series of experiments using TiO_2 and Al_2O_3 . They studied stability and coagulation rates (Wiese and Healy, 1975). It was found though that mineral oxides were not suitable for study since they undergo chemical changes and thus researchers started studying latex particles (James et al., 1977). The complexity of the mineral oxides made it difficult to test the accuracy of known models. Using the combination of hematite and glass beads, Kihira, et al. were able to prove that HHF is actually valid up to 60 mV and not 25 mV as was initially thought. The only stipulation is that both types of particles cannot have a surface potential with a magnitude greater than 25 mV (1992).

Using prior heteroaggregation studies the first forays into creating stable multicomponent aggregates were made. Using the interaction of amphoteric latex particles and silica, Furusawa and Velez were able to investigate the effect of zeta potential, particle size ratio, and electrolyte concentration (Furusawa and Velez, 1999). They also used interaction curves to template so-called “superparticles” using the latex. They were able to control the size and composition.

Much recent work involves the coating of individual microparticles with nanoparticles. The term “nanoparticle halo” is used to describe these nanoparticles surrounding the microparticles. Much of the heteroaggregation work applies to

nanoparticle halos. Tohver, et al. did experiments mixing silica microspheres with hydrous zirconia nanoparticles. They found that using neutral charge silica they were able to tune the interaction with the zirconia based solely on the concentration (Tohver et al., 2001a, Tohver et al., 2001b). They were able to use the nanoparticle halos as a stabilization mechanism. Simulation work corroborated the fact that nanoparticles are useful as a stabilizer but only in certain regimes (Karanikas and Louis, 2004, Liu and Luijten, 2004).

The next system studied was composed of silica microspheres and polystyrene nanoparticles. This system also displayed stability through nanoparticle haloing. There were a couple of possible interaction regimes that were seen: bridging (aggregation) and haloing (full surface coating) (Chan and Lewis, 2005). Through further study of this system it was found that there is middle aggregation regime and above and below particles tend to be stable (Gilchrist et al., 2005). Further simulation work was able to demonstrate that nanoparticle haloing is not dependent on electrostatic interactions but can occur with van der Waals interactions (Barr and Luijten, 2006). Simulation work employing integral equation theory was also done that corroborates the three regimes that are possible with interacting microparticles and nanoparticles (Scheer and Schweizer, 2008).

1.2.4 Micro- and Nanoencapsulation Using Chitosan and Alginate

Encapsulation is the process of entrapping a compound by forming a particle or capsule around that compound. Micro- and nanoencapsulating particles have many

applications including but not limited to drug and flavor/fragrance delivery, use as tracers, waste and toxin removal, and the protection of active ingredients from the outside environment (Gibbs, 1999, Hester-Reilly and Shapley, 2007, Ravi Kumar, 2000, van Soest, 2007). Two commonly used ingredients in encapsulation technology are alginate and chitosan.

There are many known methods to produce chitosan capsules. Each have their advantages and disadvantages when it comes to size, release profiles, and stability. The known methods include emulsion cross-linking, emulsion-droplet coalescence, coacervation, spray drying, reverse micelles and ionotropic gelation (Agnihotri et al., 2004, Sinha et al., 2004).

Emulsion cross-linking and emulsion-droplet coalescence are similar chitosan capsule creation methods. Emulsion cross-linking is the method of creating a water-in-oil emulsion of a chitosan solution and then cross-linking the resulting chitosan droplets with a suitable agent like glutaraldehyde or formaldehyde (Berthold et al., 1996). This method produces large microparticles. Quicker release is dependent on lower cross-linking efficiency, larger particle size and larger payload loading (Thanoo et al., 1992). With emulsion droplet coalescence, a water-in-oil emulsion is again used but this time particles are precipitated out using NaOH (Tokumitsu et al., 1999). In this method particle size is solely dependent on the type of chitosan used. With a higher degree of deacetylation the particle size decreases. Coacervation is similarly performed to emulsion-droplet coalescence just without a pre-emulsion (Agnihotri et al., 2004).

Chitosan solutions, like many other liquid excipient solutions, can be spray dried to create particles. He, et al used spray drying to encapsulate cimetidine, famotidine and

nizatidine with chitosan (1999). Particles produced were in the 2-10 μm range and they had a quick release profile in their studies.

Reverse micellar method is similar to the emulsion cross-linking method in the small droplets of chitosan are cross-linked. In this case, chitosan solution is inside a reverse micelle and is then cross-linked. This produces very small chitosan particles on the order of 30-110 nm particles with low cross-linking or 500-600 nm with high cross-linking (Banerjee et al., 2002).

Finally, one of the more common methods for producing chitosan nanocapsules is with ionotropic gelation due to its simplicity and low toxicity (Agnihotri et al., 2004). Also, since these nanoparticles have pH tunable release (Harris et al., 2011) they are suitable for oral delivery which makes their use more widespread. The method of ionic gelation involves mixing chitosan solution with a counterion solution, such as sodium tripolyphosphate (TPP) that creates a reversible electrostatic link rather than a chemical link (Sinha et al., 2004). Other counterions such molybdate have also been used (Dambies et al., 2001).

Creation of alginate capsules does not have quite as many varying methods of preparations. All methods involve the use of a divalent ions to perform cross-linking (Tønnesen and Karlsen, 2002). Ca^{2+} , Ba^{2+} , and Sr^{2+} , were tried as the cross-linking divalent ions with Ca^{2+} providing the most stability to the alginate beads (Takka and Acartürk, 1999b). Alginate bead size can then be controlled by using different physical methods. Extrusion can be used to drip an alginate solution drop wise in a solution with Ca^{2+} ions (Takka and Acarturk, 1999a). Ca^{2+} ions can be slowly added to a water-in-oil emulsion with an alginate solution (Yu et al., 2013).

1.2.5 Background and Applications of Fluorescence Spectroscopy

Fluorescence is the short time scale emission of light from any substance during a return to ground state of an electron from an excited state. Fluorescence spectroscopy is the technique of capturing the signal intensity of that emitted light after excitation. Fluorescence spectroscopy is conducted by pulsing a sample with a certain wavelength of light and capturing the resulting spectrum over a range of wavelengths (Johnson, 2010). The resulting light signal is collected at a right angle from the light source in order to reduce the intensity of the emitted light captured by the detector so as to not confound the emission spectrum (Albani, 2008).

Spectra generated from fluorescence spectroscopy are highly dependent on the properties of the fluorescing molecule or fluorophore as it is known. Fluorophores come in two types: intrinsic and extrinsic (Lakowicz, 2007). Intrinsic fluorophores are already part of a larger molecule while extrinsic ones are added to larger molecules (Albani, 2008). Examples of intrinsic fluorophores include aromatic amino acids and enzyme cofactor like NADH (Lakowicz, 2007).

Extrinsic fluorophores are more widely used as many different applications of fluorescence do not employ molecules that are inherently fluorescent. Many have a group attached that allow them to form covalent or non-covalent bonds with their intended labeling targets (Lakowicz, 2007). Some examples of extrinsic fluorophores are naphthalene sulfonate and its derivatives, nucleic base binders such as ethidium bromide, and fluorescein and rhodamine derivatives (Albani, 2008, Lakowicz, 2007).

The most important things to keep in mind when choosing an extrinsic fluorophore are its behavior in the testing medium, its labeling efficiency, and its Stokes shift. Fluorescein isothiocyanate (FITC), a fluorescein derivative, can be used as an illustration for how all three of these properties affect the fluorophore's fluorescent output. Fluorescein for example is pH dependent (Figure 1.1).

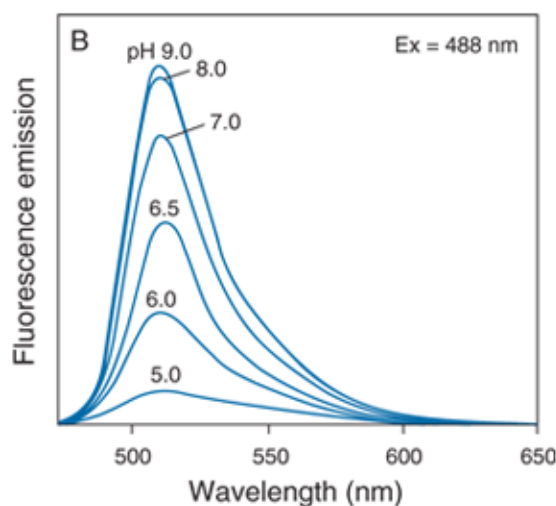


Figure 1.1. Illustration of pH dependence of FITC reproduced from Johnson (2010).

FITC has a good labeling efficiency which would normally indicate that fluorescent intensity is improved with higher labeling but that is not the case here and that is due to the Stokes shift. Stokes shift is the difference in peak wavelength of the excitation and emission (Johnson, 2010). Fluorescein has a small Stokes shift (Figure 1.2).

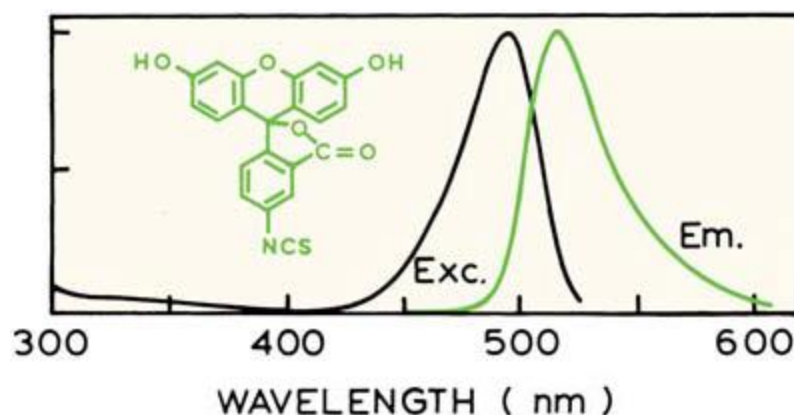


Figure 1.2. Stokes shift of FITC reproduced from Lakowicz (2007).

Small Stokes shifts lead to self-quenching (Lakowicz, 2007). This self-quenching is what makes higher labeling detrimental to the emission signal strength. Now if self-quenching is a property that is desired, FITC would be a molecule that can be used. For example, particles that are tagged with FITC may be naturally repellant but there may be something in the particles' environment that would cause them to come into closer contact with each other. This can be potentially represented with a lowered fluorescence peak due to the self-quenching in closer contact.

Knowing this background has allowed many different applications of fluorescence spectroscopy to be developed. There are many fields in which the technique is used, from food applications (Strasburg and Ludescher, 1995) to pharmaceutical applications (Moreira et al., 2004) among others. The most common use of fluorescence spectroscopy is in biological applications.

One early study involving fluorescence spectroscopy was studying the interaction of metal ions and DNA (Jennette et al., 1974). Some work was done on detecting tumor cells with fluorescent staining (Golden and West, 1974). Other work was done on particular uptake into cells (Lakowicz and Hylden, 1978). Cell uptake in particular has

been a very prominent application of fluorescence spectroscopy with attempts at targeted delivery. Anything from the cell uptake of modified gold nanoparticles (Rosi et al., 2006) to Gd (III) encapsulated chitosan nanoparticles (Nam et al., 2010) are studied using fluorescence spectroscopy. Since fluorescence spectroscopy already has applications with chitosan nanoparticles, it is only logical to apply it to studying particle interactions involving chitosan nanoparticles.

Chapter 2

Particle Migration in Oscillatory Torsional Flows of Concentrated Suspensions

2.1 Introduction

In this work, we have performed experiments involving noncolloidal suspensions of spheres undergoing moderate amplitude oscillatory shear. We address the question of whether shear-induced particle migration occurs in oscillatory torsional flows of varying strain amplitude and oscillation frequency. The major contribution of our study is the simultaneous measurement of the radial particle migration velocity in oscillatory flow and the oscillatory torque evolution. In the Experimental Methods section we discuss the materials, specific procedures and experimental parameters. We observed torque evolution and particle drift in the radial direction for each of these experiments. In the Results section we present the dependence of the data on oscillation frequency and strain amplitude. In the Discussion section we compare these results to those of steady torsional flow and also to calculations based on available continuum models. Finally, we relate our radial drift velocity and torque evolution observations to studies in the literature concerning microstructure formation and estimate the potential impact of secondary flows and viscoelastic effects on our results. In general, the observations of this study indicate interplay at moderate strain amplitudes between the shear-induced particle migration phenomena observed by Merhi *et al.* (2005) and Kim *et al.* (2008) in steady torsional flows and the microstructure formation effects observed by Bricker and Butler (2006, 2007) and Gondret and Petit (1996) in oscillatory torsional flows of suspensions.

2.2 Experimental Methods

2.2.1 Materials

The suspension contained 40% volume fraction of spherical, noncolloidal poly(methyl methacrylate) (PMMA) particles (39.75% normal, undyed particles and 0.25% dyed tracer particles) in a solution of ammonium thiocyanate (Sigma-Aldrich, ST. Louis, MO), glycerin (Pharmco-Aaper, Brookfield, CT), deionized water, and hydroxyethylcellulose (NatrosolTM 250 MR grade, molecular weight = 7.2×10^5 , Hercules Incorporated, Aqualon Division, Wilmington, DE). The dyed particles were treated with black RIT liquid fabric dye. Both the dyed tracer particles and normal, undyed particles were sieved so that their diameters fell between 106 and 125 μm (120-140 mesh). The suspending fluid consisted of 39 wt% ammonium thiocyanate salt, 36.5 wt% glycerin, 24.1325 wt% deionized water, and 0.3675 wt% hydroxyethylcellulose. This fluid provided the refractive index and density matching for the poly (methylmethacrylate) (PMMA) particles (Lucite International, Cordova, TN) with a density of 1.19 g/cm^3 . This solution, based on a recipe by Bailey and Yoda (2003), was used in place of the widely utilized zinc chloride, Triton X-100, and water solution (Krishnan et al., 1996) in order to minimize edge fracture instabilities. Such instabilities were observed during preliminary parallel plate flows of suspensions containing the zinc chloride suspending fluid. In the experiments presented here, edge fracture was averted through the use of the ammonium thiocyanate suspending fluid, with fairly low viscosity. The $\phi_{\text{bulk}} = 0.4$ particle volume fraction suspension studied here was slightly shear thinning, with an average steady shear viscosity of $1.34 \pm 0.42 \text{ Pa s}$ over the experimental shear rate range of $0.1\text{-}10 \text{ s}^{-1}$. All experiments were performed at 25°C .

2.2.2 Experimental Apparatus and Procedure

Figure 2.1 illustrates the experimental set up. A TA Instruments AR 2000 rheometer (TA Instruments, New Castle, DE) creates an oscillatory, torsional shear flow between parallel plates. The upper plate, attached to the rotating shaft, is a transparent, acrylic (PMMA) plate with 60 mm diameter. The lower plate, of larger diameter, is an extra PMMA plate attached to the underlying Peltier plate, so that the suspension is bounded by the same material above and below. A PixeLink A64 camera (PixeLink, Ottawa, Canada) at 3x zoom was used to obtain images. Since a direct line of sight from above was not possible, the camera was pointed horizontally at a mirror which reflected the flow occurring between the transparent PMMA plates. The side of the mirror was positioned parallel to the tangent of the upper plate edge and the camera was aligned horizontally so that the image axes corresponded to the tangential and radial directions of the flow. Also, the mirror was angled so that it reflected images from approximately 7.0 ± 1.4 mm from the outer edge of the plate, where the image field of view was 3.6 mm x 2.9 mm. An opaque white plastic background was placed underneath the lower PMMA plate in order to provide contrast for the black tracer particles. The lower PMMA plate and the background sheet had a combined thickness of 3.9 mm. A fiber-optic light source pointed directly at the flow provided sufficient lighting for imaging. The camera was able to detect the motion of tracer particles in approximately the first 1-3 particle layers nearest to the upper plate.

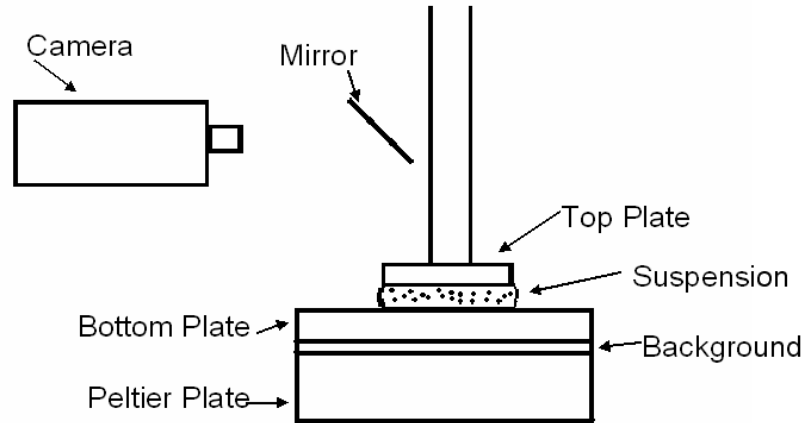


Figure 2.1. Schematic view of the oscillating parallel plate experimental setup.

The suspension was loaded on to the lower PMMA plate and the upper plate was lowered gradually in successive steps of 100 μm in order to fill the gap. We aimed to minimize the amount of suspension scraped off the outer edge, and estimate a typical excess layer at only 1-2 mm thick in the radial direction. The induction length required for meniscus formation is estimated by Ramachandran and Leighton (2007) as $L_I = k(\phi_{bulk}) (H/2)^3/a^2$, where H is the gap width, a is the particle radius, and $k(\phi_{bulk}) = 0.06$ for a suspension with $\phi_{bulk} = 0.4$. The resulting induction length has a value of 2.2 mm for the experimental system, which is larger than the typical displacement length. Another metric developed by Ramachandran (2007) specifically for the loading of circular parallel plates under

squeeze flow is $\chi = \frac{12\pi^3}{7} \frac{a^2 \hat{D} R^7}{V_0^3} \left[1 - \left(\frac{R_0}{R} \right)^7 \right]$ (p.185, Eq. 5.14), where R_0 and R

are the initial and final radii of the loaded suspension, V_0 is the initial volume, and $\hat{D} = 0.954$ is the dimensionless shear-induced diffusivity along the velocity gradient direction.

For our system, χ ranges from 0.035 (1 mm displaced) to 0.064 (2 mm displaced). These

values are a factor of 3-5 lower than $\chi_m \sim 0.175$, which indicates packed meniscus formation. Therefore, the gently loaded suspension did not travel far enough during squeeze flow for a packed meniscus to form at the outer edge of the plate and to be subsequently removed. However, some enhancement of the concentration near the edge of the plate may have occurred. Accordingly, the material remaining near the outer edge of the plates was likely of the bulk concentration or greater, and hence did not provide a driving force for radially outward particle migration.

The rheometer was operated in controlled strain mode. The control program for each experiment set the oscillatory strain amplitude and the oscillation frequency. The rheometer imposed a flow at the specified strain and frequency for the entire duration of the experiment, and the oscillatory torque was measured over time. Each run completed 4800 oscillations and the gap width (H) was maintained at a constant 1000 μm . The selected values of the oscillation frequency and oscillatory strain amplitude used in the experiments are listed in Table 2.1. For each experiment, the oscillatory torque was measured over time while the drift velocities of tracer particles were monitored with the camera.

Strain amplitude %	Frequency f (s^{-1})				
	0.1	0.25	0.333	0.5	1
0.1			x		
0.2			x		
0.415	x	x	x	x	x
0.8			x		x
1.6			x		x

Table 2.1. Parameters for oscillatory flow experiments.

The oscillation strain amplitudes were selected in order to cover the regime of moderate oscillatory shear. Moderate amplitudes are larger than the small amplitude range ($\gamma_0=A/H \leq 0.1$), where linear rheological properties are observed through small perturbations to the static microstructure, but smaller than the range of amplitudes where the steady shear microstructure is observed ($\gamma_0=A/H \geq 2$) (Breedveld et al., 2001, Bricker and Butler, 2006, 2007, Narumi et al., 2002). Among the experiments, the amplitude of the shear rate ranged from 0.1 to 10 s⁻¹. Flow Reynolds numbers in the experiments, based on the maximum tangential velocity of oscillation, the plate gap width, and the average steady shear suspension viscosity, ranged from 6×10^{-5} to 3×10^{-3} , thus indicating that inertial effects are minuscule in the system. In addition, the Womersley number or dimensionless oscillation frequency, normalized by the rate of momentum transfer across the gap width, had small values of 0.079 or less, typical of a quasi-steady flow (Dinnar, 1981). All but the two lowest oscillation frequency experiments achieved a total accumulated strain of 7500 or greater, so that a comparison with the oscillatory flow experiments of Bricker and Butler is possible, and the increasing or decreasing trend of the oscillatory torque is clearly established (Bricker and Butler, 2006). Although the final steady state was beyond the duration of our experiments, we were able to obtain slowly varying, “post-start-up” values of key quantities.

2.2.3 Fluid Rheology

Figure 2.2 presents the rheological properties of the suspending fluid, in steady shear (a) and small amplitude oscillatory shear (b). The rheological measurements were obtained by using the same AR 2000 rheometer with the actual acrylic 60 mm diameter top plate fixture used in the oscillatory flow experiments, but without the additional PMMA bottom plate and background utilized in the oscillatory flow experiments. The hydroxyethylcellulose (HEC) polymer present in the suspending fluid increased the viscosity but also caused mild non-Newtonian effects. The two plots in Figure 2.2 show that, over the experimental shear rate range of $0.1\text{-}10\text{ s}^{-1}$, the suspending fluid is only slightly shear thinning, with a nearly constant viscosity of $0.20 \pm 0.02\text{ Pa s}$, and only weakly viscoelastic, with viscous dominated rheological behavior, since the loss modulus significantly exceeds the elastic modulus. The slightly viscoelastic suspending fluid has a characteristic time scale of 0.018 s estimated from a Carreau-Yasuda model fit to the steady shear rheology data (Ponche and Dupuis, 2005). In Figure 2.2b), the overlapping forward (low to high frequency) and reverse measurements show the reproducibility of the data. In Figure 2.2a), the steady shear viscosity of the $\phi_{bulk}=0.4$ particle volume fraction suspension is also shown. The suspension is more viscous than the suspending fluid by approximately a factor of 6.6, falling between the Krieger (1972) and Zarraga (2000) relative viscosity correlations.

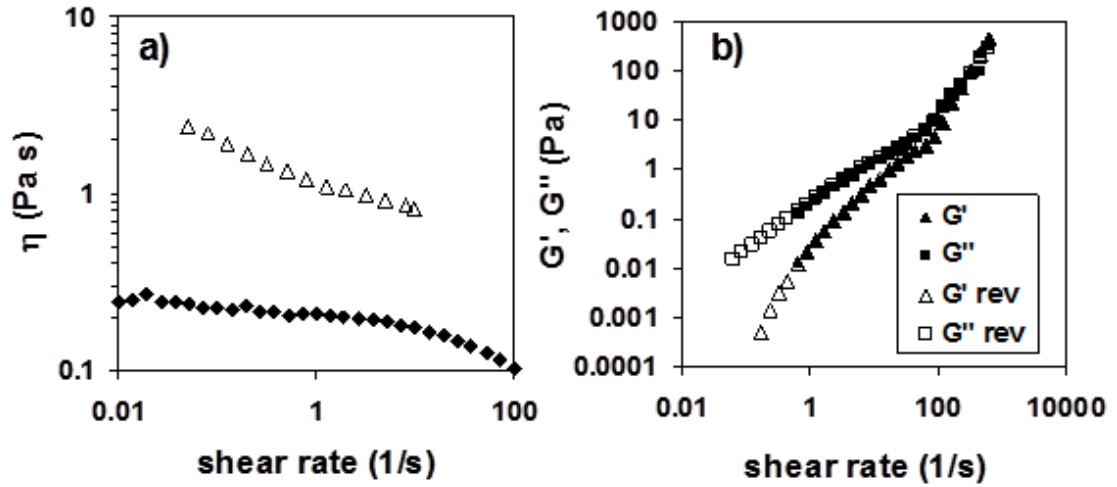


Figure 2.2 (a) Steady shear rheology of the suspending fluid (solid diamonds) and $\phi_{bulk}=0.4$ particle volume fraction suspension (hollow triangles); (b) Elastic and loss moduli of the suspending fluid at 5% strain amplitude.

The steady shear values for both the suspension and the suspending fluid were obtained during short duration measurements (maximum of 1 minute for each applied shear rate), without additional pre-shearing. The working definition of “steady state” employed by the rheometer entailed less than 5% variation in the torque during each data acquisition interval. The short duration of the rheological measurements minimized the impact of slowly developing nonuniformities in the particle concentration distribution due to particle migration.

2.2.4 Image Analysis

The program StreamPix was set up to capture images every 2 oscillations since the acquisition of live, real-time images was not possible due to RAM constraints of the computer used. The insufficient RAM caused a lag in capturing the real time images

which was eliminated with the time lapse. Since the image capture was synchronized with the oscillatory flow, only net drift motion of the particles was expected to be observed during flow. Even though the acquisitions were sometimes slightly off cycle, the error cancelled out over the course of the 2400 images. Figure 2.3 consists of three images demonstrating net radial particle drift during oscillatory flow with oscillatory strain amplitude of 0.2 and oscillation frequency of 0.333 s^{-1} . Particles used for the drift velocity calculation are marked A, B and C, and are shown at three time intervals during flow: 1500, 6000, and 12,000 seconds after flow began. The field of view of each image is $3.6 \text{ mm} \times 2.9 \text{ mm}$, and the radial position of the center of the image is approximately $r = 23.0 \pm 1.4 \text{ mm}$. The images capture tracer particles in approximately the first 1-3 particle layers adjacent to the upper plate ($z = 0.17 \text{ mm} \pm 0.17 \text{ mm}$ from the upper plate).

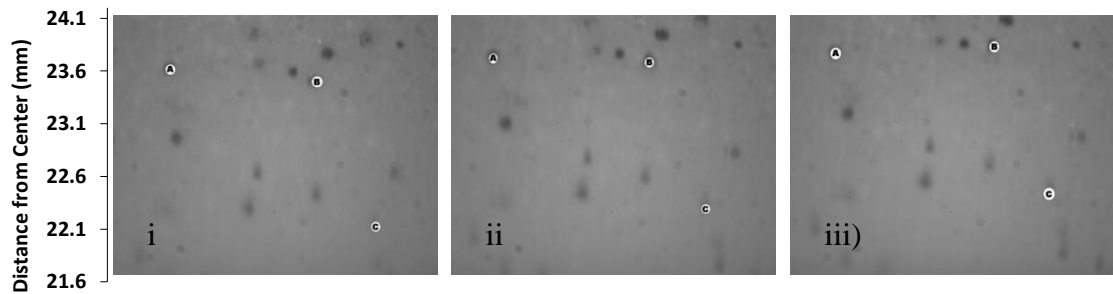


Figure 2.3. Three images demonstrating radial particle drift during oscillatory flow with strain amplitude = 0.2 and frequency = 0.333 s^{-1} . Particles used for drift velocity calculation are marked A, B, C. The images were acquired (i) 1500 sec; (ii) 6000 sec; (iii) 12,000 sec after the start of oscillatory flow. The radial direction is vertically upward in the images.

Particle velocities were determined by image analysis using ImageJ 1.36 software. Three individual particles were chosen in each experiment and particle positions were tracked every 50 images (every 100 oscillations). For example, Figure 2.4 presents the

trajectories in the radial direction of particles A, B, and C from Figure 2.3. Then, average radial and tangential velocities for each particle were determined using the calibrated size of $2.81\ \mu\text{m} \times 2.81\ \mu\text{m}$ for each pixel in the picture frame (the size of each frame was $3.6\ \text{mm} \times 2.9\ \text{mm}$) and the time at which each frame was acquired. Multiple averaging steps were used to reduce the error associated with tracking individual particles. Each velocity component of a tracer particle was averaged separately over time, and the radial velocity component was of particular interest. The average radial drift velocity values presented here were calculated from particle trajectories after the particle radial drift velocity reached a slowly varying value. For many of the experiments, the first five points (500 oscillations) in the particle trajectory were neglected, owing to the rapid flow evolution occurring during that period. Such a procedure was applied to the trajectories shown in Figure 2.4, where the slope of each particle trajectory clearly reaches a slowly varying value after an initial period of rapid variation. Then, the average radial velocity values of three tracer particles were averaged, and the mean value was identified as the radial particle drift velocity after the “start-up” of the flow.

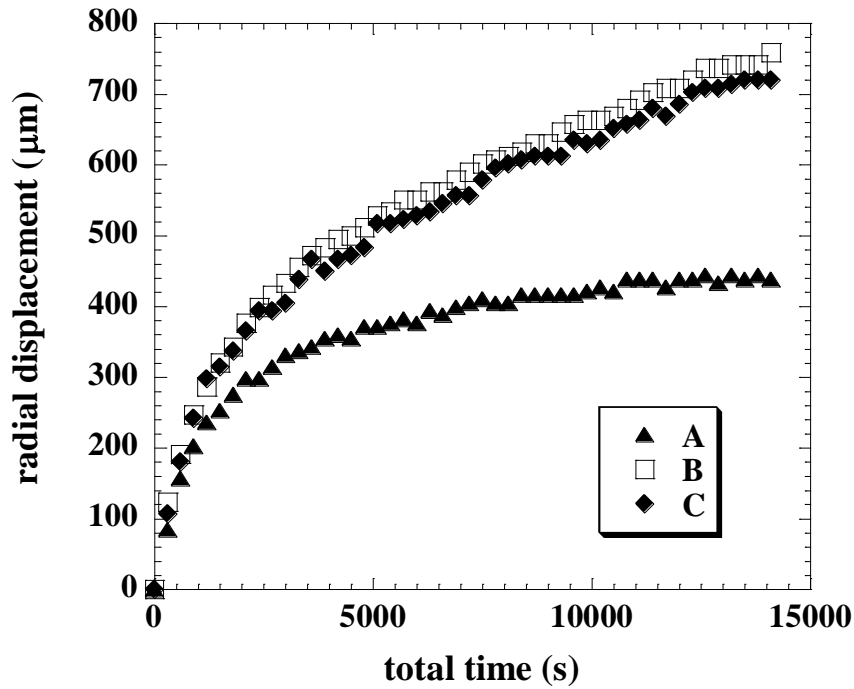


Figure 2.4. Evolution of radial trajectories of the three particles shown in Figure 2.3 at each time after the start of oscillatory flow. The time axis has the same meaning as in Figure 2.3 above, without any shifting of the origin.

The average uncertainty in the radial drift velocity measurements was estimated at approximately $\pm 10\%$. The uncertainty was determined from the differences between the drift velocity averaged over three tracer particles and that averaged over eight tracer particles in several representative experiments. It can be assumed that the velocities averaged over a greater number of particles will be more accurate, but that $\pm 10\%$ uncertainty reasonably captures the difference between three-particle and many-particle averages. A major source of variation in average velocities from particle to particle is the range of axial positions of tracer particles (approximately 1-3 particle diameters from the upper plate) captured in the same image. Since the region in focus includes particles immediately adjacent to the upper plate, and the average velocities of wall particles may

be noticeably lower than in the bulk due to wall effects, the variation shown in Figures 2.3 and 2.4 is not surprising. Most of the tracer particles in Figures 2.3 and 2.4 (including particles B and C) move with the same radial drift velocity, except for particle A, which moves more slowly than the others. Aside from the influence of wall effects, the average radial drift velocity is not expected to vary significantly along the axial direction, since the shear rate at every time is constant in that direction for a low Reynolds number and high aspect ratio flow. Axial displacement of tracer particles was not observed during the start-up of the flow, but only large displacements into or out of the imaging region could be detected.

2.3 Results

2.3.1 Radial Drift Velocity

For all of the cases studied here, the average drift velocity of the tracer particles was directed radially outward (i.e. positive values). The magnitude of the observed radial drift velocity was a function of the oscillatory strain amplitude and the frequency of oscillation. The dependence of the average radial drift velocity on the oscillatory strain amplitude and oscillation frequency is shown in Figures 2.5 and 2.6.

The average radial drift velocity of the tracer particles was measured as a function of oscillatory strain amplitude γ_0 , for oscillation frequencies of 0.333 s^{-1} and 1 s^{-1} . The results are shown in Figure 2.5a. For both oscillation frequencies, it is clear that the average radial drift velocity increases approximately linearly with the oscillatory strain amplitude. The average radial displacement per cycle is presented in Figure 2.5b, and

also generally increases linearly with the oscillatory strain amplitude. If the observed particle motion arose purely from a shear-induced migration process, the curves for the two frequencies would superimpose. Since that is not the case, some frequency dependence in the system is evident, hence suggesting the presence of a competing effect. Separate linear curve fits for the two frequencies 0.333 s^{-1} and 1 s^{-1} in Figure 2.5b result in $\delta_{r,drift} \sim 0.273 \gamma_0 \text{ (}\mu\text{m/cycle)}$ and $0.068 \gamma_0 \text{ (}\mu\text{m/cycle)}$, respectively.

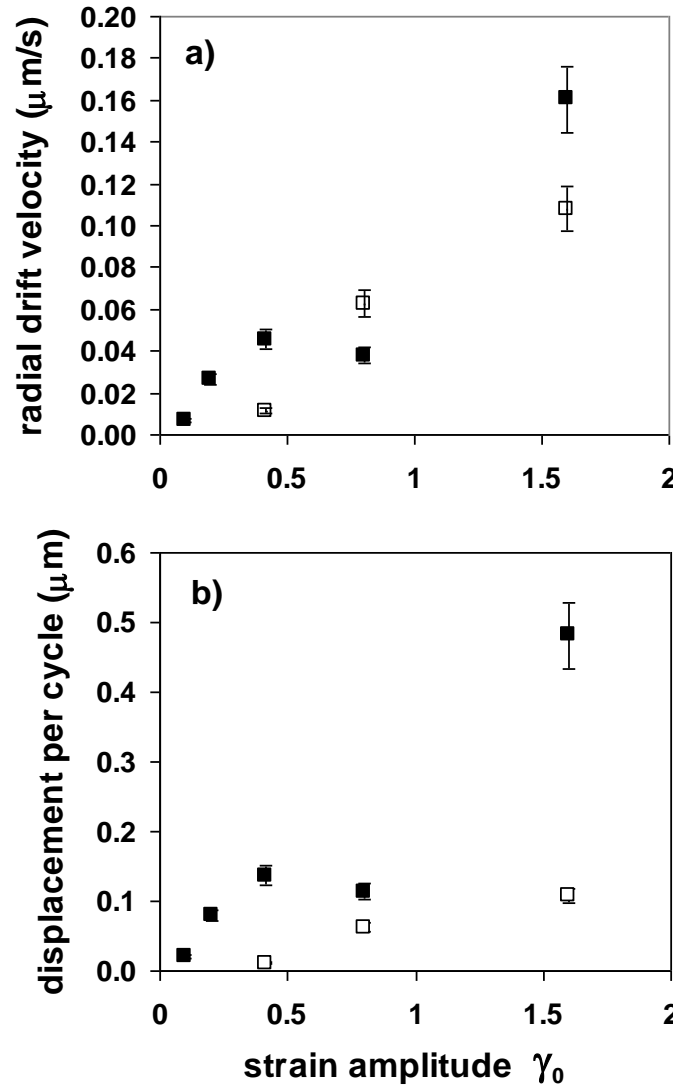


Figure 2.5. Radial drift velocity (a) and radial displacement per cycle (b) as a function of strain amplitude γ_0 , for oscillation frequencies of 0.333 s^{-1} (solid squares) and 1 s^{-1} (hollow squares).

It is reasonable that the drift velocity and displacement per cycle increase linearly with the strain amplitude. The strain amplitude determines the approximate number of interparticle collisions per half cycle, which is estimated as the collision rate multiplied by the half period, or $2\phi_{bulk}\gamma_0$ (where $\phi_{bulk}=0.4$). Therefore, we would estimate between 0.08 and 1.28 interparticle collisions per half cycle over the range of strain amplitudes examined. Since only on the order of one or fewer collisions are expected per half cycle, the flow can be considered to lie in the high “shear-induced Peclet number” regime, where convection by the mean flow is fast compared to shear-induced diffusion (Ramachandran and Leighton, 2008). The studies of Narumi *et al.* (2005) and Bricker and Butler (2006) concluded that the strain amplitude is the main parameter governing the oscillatory rheology of suspensions. One other noticeable feature of the curve in Figure 2.5 for an oscillation frequency of 0.333 s^{-1} is the local decrease in the average radial drift velocity and displacement per cycle at a strain of 0.8. The local decrease in drift velocity and displacement parallels a local decrease in torque ratio discussed below.

The average radial drift velocity was also measured as a function of oscillation frequency, for a fixed strain amplitude value of 0.415, as displayed in Figure 2.6. Figure 2.6a indicates that the average radial drift velocity is a nonmonotonic function of the oscillation frequency, with a maximum value of $0.045\text{ }\mu\text{m/s}$ at frequencies in the range of $0.25 - 0.333\text{ s}^{-1}$, and a baseline value at other frequencies of approximately $0.012\text{ }\mu\text{m/s}$. A plot of the corresponding radial displacement per cycle in Figure 2.6b indicates that the displacement generally follows an inverse square relationship with the oscillation frequency (solid line represents $0.011 / f^2$) except at very low frequency, where the

nonmonotonic behavior of the displacement is captured by the difference between an inverse square and inverse quartic function (dashed line represents $0.013 / f^2 - 0.0001222 / f^4$).

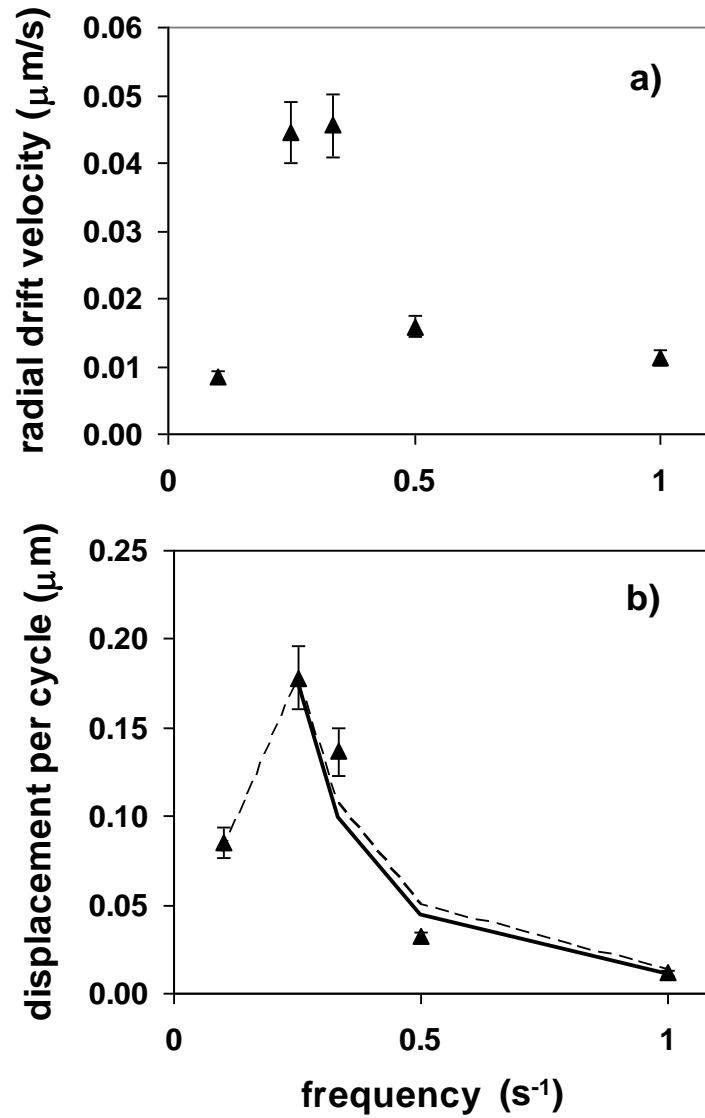


Figure 2.6. Radial drift velocity (a) and radial displacement per cycle (b) as a function of oscillation frequency, strain amplitude $\gamma_0 = 0.415$. In (b), the solid line represents the function $(0.011 / f^2)$ and the dashed line represents the function $(0.013 / f^2 - 0.0001222 / f^4)$.

The inverse square dependence of the displacement on frequency is reminiscent of the time scale of particle microstructure formation derived by Petit and Gondret (1992), which has an inverse square dependence on the shear rate: $\tau_s = \nu / [(\gamma_0 H)^2 (2\pi f)^2]$. In our data acquired at fixed strain amplitude, the radial displacement per cycle is proportional to Petit and Gondret's time scale of structure formation, where at high frequencies the structure forms rapidly and the corresponding displacement per cycle is very small. The data suggest that the formation of ordered cubic structures such as those observed by Petit and Gondret (1996, 1992) reduces the driving force for shear-induced migration, perhaps by eliminating the likelihood of collisions between particles at different heights in the z direction. However, we did not observe the inverse square dependence on the strain amplitude that Petit and Gondret proposed, since the displacement per cycle linearly increased with the strain amplitude at fixed frequency (see Figure 2.5). Therefore, in our system, it appears that the oscillation frequency rather than the shear rate provides the time scale of particle ordering interactions.

2.3.2 Torque Evolution

Simultaneous rheological measurements and particle tracking provided complementary information about suspension behavior in each experiment. Figure 2.7 shows the evolution of the oscillatory torque in a single experiment with an oscillatory strain amplitude value of 1.6 and an oscillation frequency of 0.333 s^{-1} . The torque measured at each time point is normalized by the minimum torque value obtained during the experiment. A sharp decrease in the first 265 s (89 oscillations, or a total strain value of

142) is followed by a gradual increase occurring over a period of 4800 oscillations, or 5×10^5 in total strain. Since each sample was loaded without preshearing, the initial torque decrease is attributed to the relaxation along the axial direction of structure formed during sample loading and particle protrusion through the fluid-air interface as flow commences (Chow (Chow et al., 1994, Ramachandran, 2007, Singh et al., 2006). The initial decrease in the torque occurs on a different time scale from that of the formation of ordered structure as derived by Petit and Gondret (1992). Petit and Gondret's (1992) structure time scale estimate overpredicts the time of rapid torque decrease at low strain amplitude ($\gamma_0 \sim 0.1, 0.2$) and underpredicts the time of rapid torque decrease at high strain amplitude ($\gamma_0 \sim 1.6$).

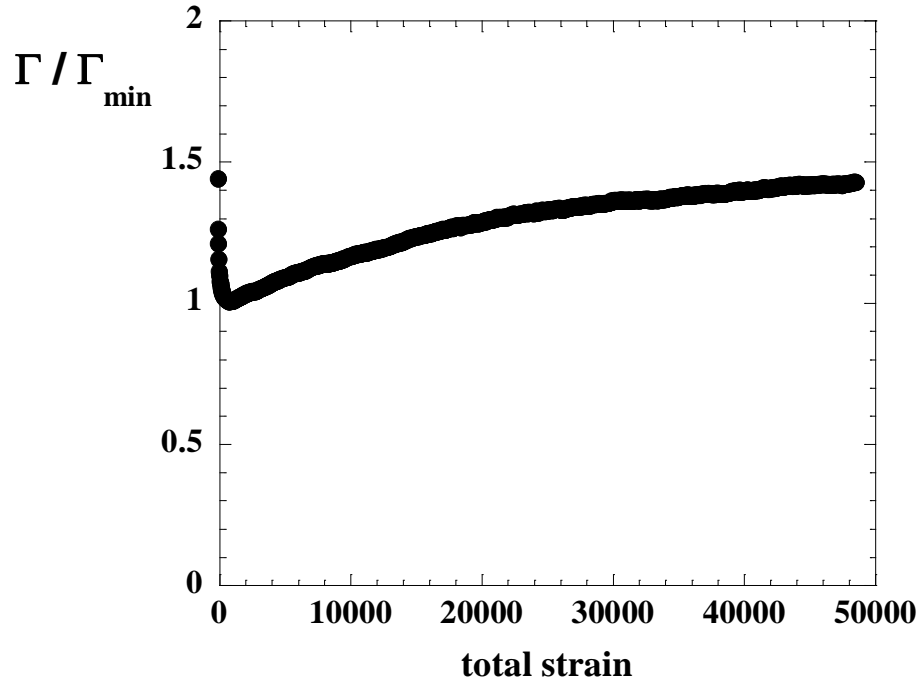
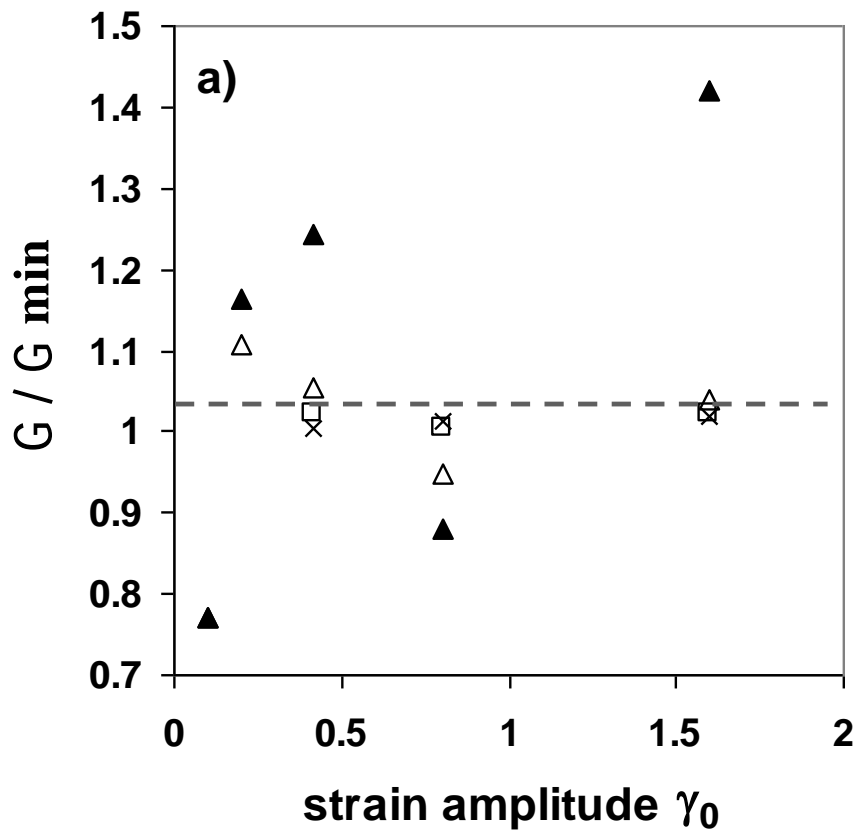


Figure 2.7. Normalized torque evolution curve, strain amplitude $\gamma_0 = 1.6$ and frequency = 0.333 s^{-1} .

The subsequent gradual change in torque is more significant and the mechanism which causes it has been recently debated in the literature. Evaporation of the aqueous suspending fluid was examined as the cause of the torque increase or decrease. Bricker and Butler particularly highlighted the importance of avoiding suspending fluid evaporation effects and specifically designed their experiments with non-aqueous based fluids in order to preclude evaporation (Bricker and Butler, 2006). Small torque increases were observed during torque evolution measurements of the pure suspending fluid, corresponding to slight stiffening of the fluid-air interface over a period of four hours. The fluid evaporation produced a baseline level of torque increase, where the net torque increases or decreases in the suspension exceeded such levels. By the naked eye there was no discernible change in concentration or crust formation near the plate edge during suspension experiments to indicate that evaporation was taking place. The length of time of the experiments was far shorter than those reported by Bricker and Butler (2006), so that the effect of evaporation on the results was less of a concern in this study. Only the longest duration experiment ($\gamma_0=0.415$, $f=0.1 \text{ s}^{-1}$), running for over 13 hours, showed possible signs of fluid evaporation causing stiffening of the air-fluid interface.

For each experiment, the ratio of the final torque value to the local minimum torque value after the initial rapid decrease appears in Figure 2.8. The final torque value was obtained after 4800 oscillations. The normalized final torque value is presented as a function of the oscillatory strain amplitude in Figure 2.8a), for experiments with oscillation frequencies of 0.333 s^{-1} and 1 s^{-1} . A clear local minimum in the final torque ratio with strain amplitude is apparent for a strain amplitude of 0.8, compared to the adjacent data points at strain values of 0.415 and 1.6. The minimum is quite sharp at an oscillation frequency

of 0.333 s^{-1} but slight for a frequency of 1 s^{-1} . Values of the torque ratio smaller than unity correspond to cases where the torque continued to decrease after the initial rapid decrease, so that the final torque was less than the initial minimum torque. Figure 2.8a) also shows the ratio of the torque at a total accumulated strain of 1930 to the initial local minimum torque, for the same frequencies. These torque ratios compare all of the experiments at the same accumulated strain of 1930, in order to compensate for the greater extent of development of the high shear experiments at a fixed number of oscillations. Again, the dip at a strain amplitude of 0.8 is clearly visible for an oscillation frequency of 0.333 s^{-1} but at a frequency of 1 s^{-1} , there is no local minimum. In summary, the trends in the torque ratios with strain are much more apparent at the lower frequency.



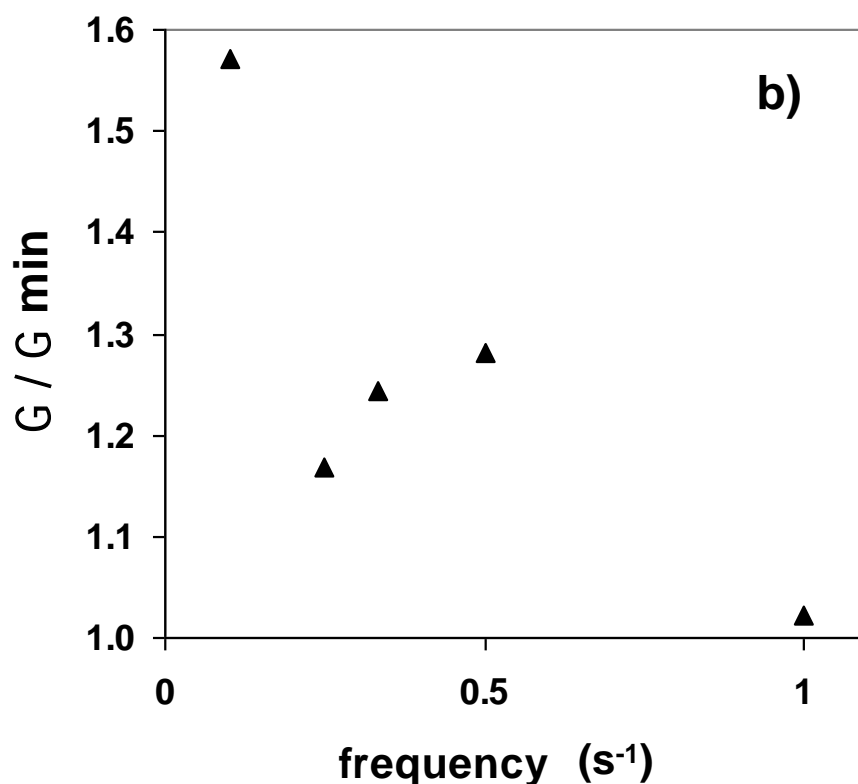


Figure 2.8. Normalized torque value (a) as a function of strain amplitude, the ratio of final torque to initial minimum torque for frequency = 0.333 s^{-1} (solid triangles) and 1 s^{-1} (hollow squares), and the ratio of torque at a total strain of 1930 and initial minimum torque for 0.333 s^{-1} (hollow triangles) and 1 s^{-1} (X). The dashed line represents the calculated final torque ratio based on the fully developed concentration profile predicted by the suspension balance model. (b) Final / minimum torque ratio as a function of oscillation frequency, strain amplitude = 0.415.

We found qualitatively similar behavior to the torque evolution ratio in the final viscosity ratio. The final suspension complex viscosity after 4800 oscillations was compared to the average steady shear viscosity. The viscosity ratios for strains of 0.415 and 0.8 are the minimum viscosity ratios for an oscillation frequency of 0.333 s^{-1} and show a significant drop (at least by a factor of two) from the surrounding values at strains of 0.2 and 1.6. At a frequency of 1 s^{-1} , the viscosity ratios at strain values of 0.415 and 0.8 had similar low values. The local minimum at intermediate strain values in the torque evolution ratio and

the final viscosity ratio agrees with the results of Bricker and Butler (2006), where a strong minimum was observed in the viscosity ratio at strains close to unity and attributed to ordering of the suspension through the formation of independent particle layers, where particles move within planes without collisions with particles in neighboring planes (Bricker and Butler, 2007). Petit and Gondret (1995, 1992) suggested a mechanism of layer formation, which is the local stationary secondary flow caused by oscillating boundary layers, even when inertial effects are very small. The local secondary flow leads to attraction of neighboring particles along the axis of shear rotation (radial direction) and repulsion of adjacent particles along the directions normal to the axis (tangential and axial directions) (Gondret and Petit, 1995, Petit and Gondret, 1992). Repulsion of particles along the axial direction is an important driving force for formation of the independent layers, where particles are slightly more separated along the z direction than in other microstructures.

In Figure 2.8b), the normalized final torque value is plotted against the oscillation frequency, for experiments with an oscillatory strain amplitude of 0.415. Here, the torque ratio is on balance observed to decrease with oscillation frequency. Due to possible suspending fluid evaporation affecting the longest duration experiment ($\gamma_0=0.415, f=0.1 \text{ s}^{-1}$), the torque ratio for the lowest oscillation frequency may be significantly overestimated. The data suggest that the normalized final torque value may follow qualitatively similar behavior to the drift velocity with oscillation frequency, where there is a maximum at moderate frequencies.

2.4 Discussion

2.4.1 Comparison of Oscillatory and Steady Torsional Flows

Over the oscillatory flow conditions examined here, the main observation was that the radially outward drift of tracer particles generally was accompanied by a gradual increase in oscillatory torque. Both outward drift and simultaneously increasing torque are consistent with a concentration (and therefore viscosity) increase near the outer edge of the rotating plate. The observed behavior is quite similar to the experimental results reported by Merhi *et al.* (2005) and Kim *et al.* (2008) for a steady, torsional suspension flow between rotating parallel plates, although the experiments reported here were performed at lower shear rates ($0.1\text{-}10\text{ s}^{-1}$ vs. $25\text{-}55\text{ s}^{-1}$). Hence, only particle migration in the same direction as that observed in steady flow was detected here.

The variation in the oscillatory torque observed here occupied a wider range than in the results reported by Merhi *et al.* (2005) for steady, torsional flow. Merhi *et al.* typically observed a 15-20% increase in the torque from the minimum to the final value, over a similar time period ($\sim 10^5\text{ s}$) but over a total accumulated strain of one to two orders of magnitude greater than the extent we examined. We observed some torque increases in the same range, but also obtained greater increases (42%) for oscillatory flow under the largest strain amplitude and moderate frequency conditions (see Figures 2.7, 2.8). Merhi *et al.* measured a maximum torque increase of 40% in one experiment (40 s^{-1}), but the increase occurred over 100 times the strain that we used. Over a comparable accumulated strain, Merhi *et al.* (2005) only observed a 15-20% torque increase for that run.

Therefore, in the limit of large strain amplitude ($\gamma_0=1.6$), the torque increase observed here is comparable or greater than that for steady flow.

A remaining open question is the differences in experimental results obtained by Merhi *et al.* (2005) and Kim *et al.* (2008) compared to Bricker and Butler (2006) for steady shear flow, since the experiments were performed at the same bulk particle volume fraction of 0.4 and in very similar flow geometries. The main parameter distinguishing the studies was a/H , the particle to gap size ratio. We suspect that the contrasting observations can be attributed to varying values of the particle to gap size ratio, which is known to have a very strong influence on suspension loading conditions, migration rates and final concentration profiles in narrow geometries (Ingber *et al.*, 2009, Ramachandran, 2007, Stickel *et al.*, 2007).

2.4.2 Comparison with Model Calculations

We also made two calculations to compare the oscillatory flow data to published steady flow results. First, we compared the observed torque increase to the increase expected in a steady flow as it evolves from the initial uniform state to the final steady state concentration distribution. The calculation of the final torque utilized the steady state concentration profile predicted by the suspension balance model (Morris and Boulay, 1999) and evaluated by Ramachandran and Leighton (2008) for rotating parallel plates using the shear stress components measured by Zarraga *et al.* (2000), where

$$\phi(r) = \frac{c \phi_m r^{-(1+b+2d)/3(1+d)}}{\phi_m + c r^{-(1+b+2d)/3(1+d)}} \quad (2.1)$$

The constant c is set by the bulk suspension concentration, where we find $c=0.79$ for $\phi_0=0.4$, and the expression $-(1+b+2d)/3(1+d)$ has a value of 0.17 from the parameters of Zarraga *et al.* (2005), where $b= -0.15$ and $d=-0.54$, in addition to $\phi_m=0.62$.

The expression utilized here for $\phi(r)$ is very similar to the measured profile of Merhi *et al.* (2005) and the calculations of Merhi *et al.* (2005) and Kim *et al.* (2008) using modified diffusive flux models, where the steady state particle volume fraction increases slightly with radial position. The dashed line in Figure 2.8a) represents the calculated final torque ratio of 1.034 for steady flow, where the final torque calculated from the steady state expression above is divided by the torque resulting from a uniform suspension with $\phi_0=0.4$, following the same procedure as Merhi *et al.* The observed torque ratios for a frequency of 0.333 s^{-1} are generally larger than the estimated steady flow torque ratio, except where the observed ratios go through a minimum at a strain amplitude of 0.8 and at a very low strain amplitude of 0.1. All observed torque ratios for a frequency of 1 s^{-1} are less than the estimated steady value.

In addition, we used the suspension balance model (Miller and Morris, 2006, Morris and Boulay, 1999) to estimate the initial radial migration velocity of particles in steady torsional flow for a suspension with the properties of the experimental system and moving at the same average velocity as the oscillatory flow. The particle drift velocity, defined as the difference between the average particle velocity and the average suspension velocity, $(\mathbf{u}_p - \mathbf{u})$, is directly related to the concentration and flow fields through the lateral flux of particles \mathbf{j}_\perp (Miller and Morris, 2006),

$$\phi (\mathbf{u}_p - \mathbf{u}) \equiv \mathbf{j}_\perp = \frac{2 a^2}{9 \eta_0} f(\phi) [\nabla \cdot \Sigma_p] \quad (2.2)$$

where a is the particle radius, η_0 is the suspending fluid viscosity, $f(\phi)$ is the hindered settling function, and Σ_p is the particle contribution to the stress tensor. Ramachandran and Leighton (2008) find the radial component for parallel plate flow (Eq. 2.23 in their work)

$$j_r = \frac{2a^2}{9\eta_0} f(\phi) \left[\frac{1}{r} \frac{\partial}{\partial r} (r \Sigma_{prr}) - \frac{\Sigma_{p\theta\theta}}{r} \right] = \frac{2a^2}{9\eta_0} f(\phi) \left[\frac{\partial \Sigma_{prr}}{\partial r} + \frac{\Sigma_{prr} - \Sigma_{p\theta\theta}}{r} \right] \quad (2.3)$$

Assuming initially uniform concentration $\phi = \phi_0 = 0.4$, and following the discussion of Ramachandran and Leighton (2008) using the functions found by Zarraga *et al.* (2000) for the stress tensor components, the equation becomes

$$j_r = \frac{2}{9} a^2 [-(1+b+2d)] f(\phi_0) \alpha(\phi_0) \mu_r(\phi_0) \frac{\omega}{H} \quad (2.4)$$

where $[-(1+b+2d)] = 0.23$, $f(\phi) = (1-\phi)^5$, $\alpha(\phi) \mu_r(\phi) = 2.17 \frac{\phi^3}{\left(1 - \frac{\phi}{\phi_m}\right)^3}$, and

$\phi_m = 0.62$.

Then, because concentration variations are slight, we can approximate the radial drift velocity as

$$v_{r,drift} \cong \frac{j_r}{\phi_0} \cong \frac{2}{9} a^2 (0.23) \frac{f(\phi_0) \alpha(\phi_0) \mu_r(\phi_0)}{\phi_0} \frac{\omega}{H} \quad (2.5)$$

where for an oscillatory flow, the average angular frequency of rotation is given by the angular distance traveled per cycle, $\omega = 4 \theta_0 f = 4 \frac{\gamma_0 H}{R} f$. The edge shear rate is given by $\dot{\gamma} = 4 \gamma_0 f$. After substitution of the functions, we find

$$v_{r,drift} \cong \frac{j_r}{\phi_0} \cong 0.11 \frac{a^2}{R} (1-\phi_0)^5 \frac{\phi_0^2}{\left(1-\frac{\phi_0}{\phi_m}\right)^3} 4 \gamma_0 f \quad (2.6)$$

For the experimental parameters of $\phi_0=0.4$, $a=58 \mu\text{m}$, $H=1 \text{ mm}$, and $R=30 \text{ mm}$, the expression becomes $v_{r,drift} \cong 0.0133 \gamma_0 f (\mu\text{m/s})$.

Figure 2.9 shows the comparison of the measured radial drift velocity for oscillation frequencies of 0.333 s^{-1} and 1 s^{-1} and for fixed strain amplitude of 0.415, and the estimated initial migration velocities in steady flow, as a function of shear rate. For each frequency, the measured velocity is clearly larger than the estimated steady migration velocity. The slope for oscillatory flow is greater by a factor of 21 for $f=0.333 \text{ s}^{-1}$ and a factor of 5 for $f=1 \text{ s}^{-1}$ compared to the steady flow estimates. Taken together, the results for the radial migration velocity and the oscillatory torque suggest that the rate and extent of migration in oscillatory flow are greater than that predicted by continuum models for a corresponding steady flow. It seems that the enhanced radial migration velocity in oscillatory flow can be attributed to the looser particle microstructure that forms under oscillatory shear compared to steady shear, with greater average spacing between particles and therefore increased particle mobility (Narumi et al., 2005, Yapici et al., 2009).

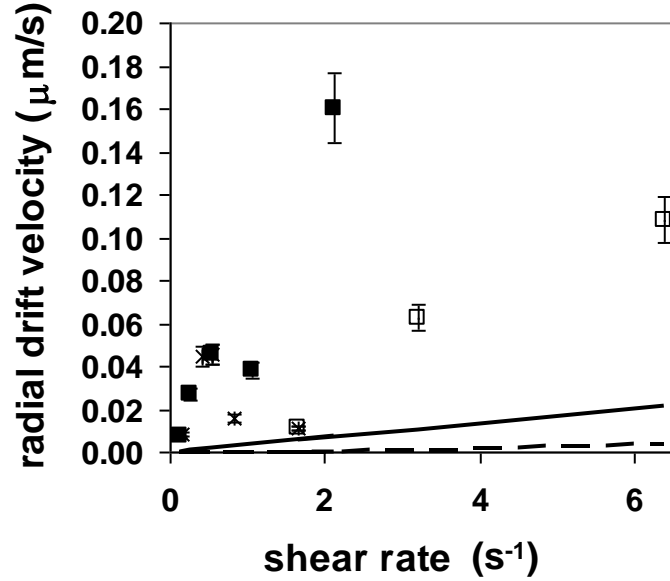


Figure 2.9. Measured radial drift velocity for oscillation frequencies of $0.333 s^{-1}$ (solid squares) and $1 s^{-1}$ (hollow squares), and strain amplitude of 0.415 (stars), compared with the estimated initial migration velocity in steady flow, based on the suspension balance model, at the same average velocities corresponding to the oscillatory flows (solid line). The estimated secondary flow velocity for a Newtonian fluid at low Reynolds number in the infinite plate limit (McCoy and Denn, 1971) is also shown (dashed line).

Global secondary flow is an unrelated effect which has the potential to obscure the measurement of the radial migration velocity in the parallel plate geometry. During steady shear of a Newtonian fluid between rotating parallel plates, large-scale secondary flow due to inertia appears as a toroidal motion with outflow near the moving plate and inflow near the stationary plate. For a viscoelastic fluid, normal stresses promote secondary motion in the opposite direction (Hill, 1972), and the two effects may cancel out in viscoelastic liquids with large normal stress differences (Feng and Joseph, 1996). Based on the work of McCoy and Denn (1971), we estimated the radial velocity due to macroscopic secondary flow in a Newtonian fluid under steady shear at the conditions of our experiments. We used Eq. [18] of McCoy and Denn, for the “infinite disk” solution

$(R/H \rightarrow \infty)$ at low Reynolds number, where the radial velocity due to secondary flow is given by (to second order in pseudo-Reynolds number N_{Re}):

$$u = -(r/R) N_{Re} / 60 [4 (1 - z/H) - 9 (1 - z/H)^2 + 5 (1 - z/H)^4] R \omega \quad (2.7)$$

where $N_{Re} = \rho H^2 \omega / \eta$, and we evaluate the solution at the experimental location $r/R=0.767$ and $z/H=0.174$, which corresponds to an axial distance of 1.5 particle diameters from the rotating plate, and $R\omega = 4 \gamma_0 H f$ is the average rotation velocity during each half cycle. The estimated secondary flow radial velocity was negligible for all of the flows examined here, where it ranged from 0.02% - 4% of the measured radial drift velocity. The dashed curve in Figure 9 shows the magnitude of the estimated secondary flow velocity compared to the measured radial drift velocity values. Since the oscillatory flows occurred at very low Reynolds numbers, the impact of large-scale secondary flow was minimal.

2.4.3 Viscoelastic Effects

Viscoelastic effects did not have a noticeable impact on the results of this study. Although with a dilute concentration of tracer particles we were not able to observe it, we did not expect to see any appreciable extent of particle chaining along the flow direction. Chaining is frequently observed for particles suspended in viscoelastic liquids. Recent studies show that strong shear thinning is a key property of the fluid that promotes chaining (Won and Kim, 2004). Since the suspending fluid used in this study was only

weakly shear thinning, we do not believe the non-Newtonian chaining effect is significant in our system.

In experiments tracking single spherical particles suspended in viscoelastic liquids during steady torsional flow, Feng and Joseph observed outward migration of particles for concentrated solutions of polyethylene oxide (1% and 2%), and very slow inward migration for more dilute solutions (0.5%) (Feng and Joseph, 1996). The suspending fluid used in this study had rheological properties most similar to the dilute 0.5% suspending fluid of Feng and Joseph. Therefore, the presence of a non-Newtonian suspending liquid was expected to produce at most slight migration in the opposite direction to that observed in our experiments.

2.4.4 Oscillation Amplitude Effects on Microstructure

All the values of the oscillatory strain amplitude tested here (0.1 – 1.6 strain units) are below the typical limit for full development of the steady state particle orientation arrangement of about 2-3 strain units, as shown in the work of Breedveld *et al.* (2001) and Narumi *et al.* (2002, 2005). Since the oscillation strain amplitudes span the regime of moderate oscillatory shear ($0.1 \leq \gamma_0 = A/H < 2$), a particle microstructure distinct from both the uniform and the steady shear cases is expected. Breedveld *et al.* and Narumi *et al.* find that particle “cages” are disrupted by strain amplitude ~ 1 (Breedveld *et al.*, 2001, Narumi *et al.*, 2002, Narumi *et al.*, 2005).

In the results presented here, we observe two interesting effects which offer hints about the suspension microstructure under oscillatory torsional flow. First, the marked frequency dependence of the radial drift velocity and final torque ratio has not been prominently featured in previous work. In general, other experimental studies have focused on a higher frequency range, such as 1.59 s^{-1} (Bricker and Butler, 2006) or 200 s^{-1} (Gondret and Petit, 1996, Petit and Gondret, 1992), where the trend of our data indicates that the radial drift velocity and torque variation would be negligible. Indeed, in another set of low frequency experiments, Narumi *et al.* (2005) observed frequency dependence in their study of large amplitude oscillatory shear flows in the cone and plate rheometer of mono-, bi-, and polydisperse suspensions with a bulk particle volume fraction of 0.5. For the monodisperse suspensions in particular, the apparent viscosity at a shear rate of 1 s^{-1} decreased with frequency, where there was a 25% drop in viscosity between frequency 0.333 and 1 s^{-1} in their Figure 7, and no further frequency dependence above a frequency of 1.5 s^{-1} (Narumi et al., 2005).

The significant decrease in both the radial displacement per cycle and the final torque ratio with oscillation frequency that we obtained suggest that another competing process hinders shear-induced particle migration preferentially at high frequency. The formation of ordered cubic structures such as those observed by Petit and Gondret (1996, 1992) is a possible explanation of the results, where cubic packing yields independent particle layers which can slide past each other and experience relatively few collisions with particles at other axial positions. Since shear-induced particle migration arises from stress gradients communicated through collisions between particles in neighboring shear layers, the formation of noninteracting layers would be expected to reduce such interactions and

hence slow down the rate of particle migration. Petit and Gondret (1992) also characterize the ordered microstructure formation as a local inertial effect, where the steady streaming velocity arising from the secondary flow around each rotating particle is proportional to the Reynolds number. Therefore, the attraction of particles along the axis of shear rotation and repulsion in the normal directions will increase with oscillation frequency and lead to a greater rate and extent of ordering at high frequency, and consequently a decrease in the rate of particle migration. Furthermore, the nearly inverse square dependence of the radial displacement per cycle on the oscillation frequency (Figure 6b) resembles Petit and Gondret's (1992) scaling estimate of the time scale of ordered structure formation. Based on the arguments discussed above, it seems reasonable that ordered cubic structure formation hinders shear-induced particle migration as the oscillation frequency increases.

The second distinct effect we observed is the local minima in the radial displacement per cycle and in the torque ratio at intermediate strain amplitude values ($\gamma_0=0.8$). The local minima at intermediate strain values are consistent with the rheology results of Bricker and Butler (2006). The simulations of Bricker and Butler, which support their rheology data, suggest that at intermediate strain amplitudes, particles form horizontal layers, where the particles are free to move in the plane without collisions with particles in adjacent layers (Bricker and Butler, 2007). Therefore, the radial direction offers relatively low resistance when particle layers form, corresponding to the observed decrease in torque as the flow evolves as well as the low relative viscosity values compared with steady flow for such intermediate amplitude cases ($\gamma_0=0.8$).

We speculate that the dominant ordered microstructure occurring in our system is the configuration identified by Gondret and Petit (1995). Based on viscosity data, they find that the ordered cubic arrangements of particles consist of staggered square arrays and staggered triangular arrays coexisting within the particle layers. The staggered layers can glide over each other, but some interaction between particles in neighboring layers is still likely, thus allowing the collisions that cause shear-induced particle migration. At an intermediate strain amplitude of 0.8, the rheology data and planar simulations of Bricker and Butler (2006, 2007) suggest that an even lower viscosity configuration develops, similar to a non-staggered cubic array of particles. In a non-staggered array, the particle layers have a greater axial separation distance (Gondret and Petit, 1995) and are therefore even less likely to interact. A resulting decrease in the radial displacement per cycle and torque ratio would then be expected, matching our observations. However, the mechanism of microstructure evolution in torsional flow is not yet well understood and is a likely topic of further study.

2.5 Summary

Overall, the observations of this study appear to be a superposition of the results of Bricker and Butler (2006, 2007) and Gondret and Petit (1996) for oscillatory flows of suspensions. The unique contribution of our study is the measurement of radial particle migration velocities, which were compared with model predictions for steady torsional flow, and generally were found to exceed estimated values based on the normal stress balance model. Also, our characterization of the strong frequency dependence of the

radial migration velocity and torque evolution provided further insight into microstructure development during oscillatory flow. Since there has been recent interest in transient flows and the evolution of particle distributions, these measurements fill important gaps in our knowledge of suspension behavior. For all of the cases studied here, the average drift velocity of the tracer particles post “start-up” was directed radially outward and was approximately a linear function of the oscillatory strain amplitude while also depending on the frequency of oscillation in a nearly inverse square relationship. We attribute the enhanced migration in oscillatory flow compared to steady flow to the looser microstructure formed during oscillatory flow, where the average particle separation distance is larger and particles are not as tightly packed in clusters along the compression direction of flow. We also obtained complementary torque evolution measurements. In most cases, the torque increased as the flow evolved, as was previously observed in steady flow, and a local minimum in the torque ratio was detected at intermediate strain values, as was observed in other studies of oscillatory flow. Together, these results suggest the competition between radial shear-induced particle migration driven by the overall particle stress balance and microstructural ordering driven by local inertial effects gathering the particles into layers. Further studies quantifying the particle microstructure evolution will lead to improved insights into torsional flows of concentrated suspensions.

Chapter 3

Applying Fluorescence Spectroscopy to Distinguish Between Particle Interaction Regime Transitions

3.1 Introduction

When oppositely charged microparticles and nanoparticles are mixed together, aggregation tends to occur. The specific type of interaction and resulting aggregate morphology that occurs is dependent on particle concentration (Tohver et al., 2001a, Tohver et al., 2001b). The various types of particle interactions can be distinguished at boundaries according to concentration ratios. Unfortunately, particle interaction regime boundaries can only be determined visually by using microscopy or by using not typically available techniques such as ultra-small-angle X-ray scattering (Gilchrist et al., 2005, Zhang et al., 2008). Accordingly, this study aimed to create a new easy-to-use analytical method to quantify the interaction regime boundaries by using fluorescence spectroscopy. It was hypothesized that fluorescence spectroscopy would provide the ability to distinguish the interaction regime boundaries by using a fluorophore that would have a different intensity output in each of the interaction regimes.

The system used to test this analytical method was a mixture of alginate microspheres and fluorescently tagged chitosan nanoparticles. Although previous studies have examined interaction regimes in mixtures of microparticles and nanoparticles (Gilchrist et al., 2005, Zhang et al., 2008), this study involves distinctive materials which are highly hydrophilic and oppositely charged hydrogels. Optical microscope images were used to determine interaction regime boundaries. Independent spectroscopic results were then compared to the known interaction regime boundaries. In addition, the location of the interaction regime boundaries provided insight into the interplay of colloidal particle interactions in the system.

3.2 Experimental Methods

3.2.1 Materials

Chitosan was tagged with fluorescein isothiocyanate (FITC) according to the procedure outlined in Huang et al. (2004). The chitosan used for tagging was the low molecular weight type purchased from Sigma Aldrich. The chitosan had a deacetylation fraction of 90.85% and molecular weight range of 50 to 190 kDa. More specifically, the acquired batch had a viscosity of 185 cP (for a concentration of 1 w/w in 1 w/w acetic acid solution) (all data provided by supplier). The FITC was also from Sigma Aldrich and was under the title Fluorescein 5(6)-isothiocyanate BioReagent, suitable for fluorescence, mixture of 2 components. The solution of chitosan that was dissolved in water and acetic acid was mixed with a solution of FITC dissolved in methanol for 3 hours to complete tagging. Chitosan was then precipitated out of solution by NaOH and centrifuged and washed several times. The tagged chitosan was then polymerized with sodium tripolyphosphate (TPP) using the ionic gelation method outlined in Yu et al. (2013). The TPP was purchased from Sigma Aldrich and was the technical grade, 85%. The solutions of chitosan and TPP were at a concentration of 2 mg/mL. The chitosan solution also had 3.5 mg/mL of acetic acid in addition to the deionized water. 0.7 mL of TPP solution was added to 5 mL of the chitosan solution. The particles created with this procedure had an average diameter of 250 nm with a zeta potential of approximately 40 mV. The zeta potential value contrasts with that of a previous study, where Gilchrist et

al. used polystyrene nanoparticles with a zeta potential of 95 mV (2005). These chitosan particles were suspended in water at a concentration of 37.5 mg/mL. They have a density of approximately 1g/mL. Water used for all experiments was acquired from a Milli-Q water system.

In order to form the alginate microparticles, a sodium alginate and sucrose solution was emulsified in 1,6-dibromohexane and iso-octane with span-80 as the surfactant. The sodium alginate was purchased from Acros Organics under the name alginic acid, sodium salt. It had a molecular weight range of 450 to 550 kDa and a viscosity of 485 cP (for a 1% w/w solution) (data provided by supplier). Furthermore, the sodium alginate contained 65-75% guluronic acid (G) subunits and 25-35% mannuronic acid (M) subunits. The dibromohexane was obtained from Sigma Aldrich and is the one at 96% purity. Iso-octane was HPLC grade and purchased from Fisher Scientific. Span-80 was purchased from Sigma Aldrich. The emulsified alginate was crosslinked with calcium chloride purchased from Fisher Scientific using the outlined method in Yu et al. (2013) to create calcium alginate beads. The resulting beads were wet sieved down to below 38 μm diameter and then after that were filtered using vacuum filtration with a 25 μm pore size filter paper to be above 25 μm diameter with an average diameter of 34 μm (measured with Beckman Coulter LS 13 320). The alginate microparticles have a zeta potential of ~ -46 mV (Mladenovska et al., 2007). The value is similar to that found in a previous study, where Gilchrist et al. used silica microparticles with a zeta potential of -52 mV (2005). The alginate microparticles are stored in water. They have an approximate density of 1.05 g/mL. The alginate microparticles are approximately 136 times larger in diameter compared to the chitosan

nanoparticles. This particle size ratio is larger than the ratio that Gilchrist et al. used, which was 59 (2005).

3.2.2 Instrumentation

The two instruments we used to measure fluorescent intensity were an Ocean Optics USB4000FL Fluorescence Spectrometer and a Horiba Jobin Yvon FluoroMax-3 TCSPC Spectrofluorometer. The Ocean Optics spectrometer is a modular instrument while the Horiba Jobin Yvon one is a “black box” instrument.

For the Ocean Optics instrument we used the PX-2 pulsed xenon light source with a right angle cuvette holder. Fiber optic cables connected the cuvette holder to the light source to the cuvette holder and the spectrometer. A monochromator (filter) is placed in between light source and the sample to control the excitation wavelength that is passed into the sample. This is self-calibrated prior to collection of each spectrum. SpectraSuite software controls the pulsing of the light and the integration time needed to generate a full range spectrum. They have a measured value of the signal-to noise-ratio of 300:1. As a result there is a lot of variability in the spectrum at each pulse of light.

The Horiba Jobin Yvon spectrometer also uses a xenon lamp. There are two monochromators used. One sits in between the light and the sample and the other in between the sample and the detector. The monochromators are already precalibrated and thus the sample is pulsed at the inputted wavelength (excitation) and then the intensity is detected at a range of separately inputted wavelengths (emission). The spectrum

generated is only for the emission range specified. The whole process is automated by the FluoroEssence software.

3.2.3 Experimental Procedure

Each measured sample contained distinct levels of chitosan and alginate particles mixed into deionized water. Total sample volume was kept constant at 8 mL each. To prepare each sample, water volume was first measured out. The amount of water in each sample was varied according to how much of the chitosan suspension was added. Then the proper amount of alginate microparticles (by weight) was added into the measured water volume. In order to obtain the alginate beads from their storage suspensions, they were centrifuged at 6000 RPM in a Beckman centrifuge with the rotor (approximately $5500 \times g$) for 5 minutes. After adding the alginate to the water the sample was sonicated for a minute at low power to ensure resuspension of the beads. After that, the chitosan suspension was measured out by volume and added to the sample. The sample was again sonicated for another minute at the same power. Then, the sample was left to stir on a stir plate using microstirbars for an hour to allow it to cool before testing. The alginate levels used were 0.05 g, 0.1 g, and 0.2 g (approximately 2.31×10^6 particles, 4.63×10^6 particles, and 9.26×10^6 particles, respectively). The approximate volume fractions of alginate particles in each sample are 0.006, 0.012, and 0.024 indicating that all the suspensions are dilute. The levels of chitosan (in suspension volumes and approximate particle number) and the corresponding water volumes used for each sample are shown in Table 3.1.

Sample	Chitosan Volume	Number of Chitosan Particles	Chitosan Volume Fraction	Water Volume
1	6.25 μL	3.06×10^{10}	3.13×10^{-5}	7.99375 mL
2	12.5 μL	6.11×10^{10}	6.25×10^{-5}	7.9875 mL
3	25 μL	1.22×10^{11}	1.25×10^{-4}	7.975 mL
4	50 μL	2.44×10^{11}	2.50×10^{-4}	7.95 mL
5	100 μL	4.89×10^{11}	5.00×10^{-4}	7.9 mL
6	200 μL	9.78×10^{11}	1.00×10^{-3}	7.8 mL
7	400 μL	1.96×10^{12}	2.00×10^{-3}	7.6 mL
8	800 μL	3.91×10^{12}	4.00×10^{-3}	7.2 mL
9	1600 μL	7.82×10^{12}	8.00×10^{-3}	6.4 mL
10	3200 μL	1.56×10^{13}	1.60×10^{-2}	4.8 mL

Table 3.1. Levels of chitosan for each sample and corresponding water volumes

The amount of chitosan is doubled in each successive sample. Three trials were performed for each chitosan and alginate level.

Each prepared sample was tested in the Ocean Optics and Horiba Jobin Yvon fluorescence spectrometers. 3 mL were added to a 4 sided clear plastic cuvette along with a microstirbar. The samples were stirred while a spectrum was taken to prevent any settling. In both spectrometers the wavelength of light used to pulse the sample was 490 nm. This was approximate for the Ocean Optics spectrometer while the Horiba Jobin Yvon was centered at 490 with a 5 nm slit. Both spectra were taken with a 100 millisecond integration time. The Ocean Optics results were an average of 10 scans with the 100 millisecond integration.

Another set of experiments were performed keeping chitosan constant and varying the alginate. The chitosan levels tested were 25 μL , 35 μL , and 200 μL (approximately 1.23×10^{11} particles, 1.71×10^{11} particles, and 9.78×10^{11} particles, respectively). The approximate volume fractions are 1.25×10^{-4} , 1.75×10^{-4} , and 1×10^{-3} .

This time, the ratio of alginate to chitosan was kept constant between the chitosan levels.

The levels tested are shown in Table 3.2.

Sample	Chitosan Suspension Volume	Water	Alginate (g)	Number of Alginate Particles	Alginate Volume Fraction
1	25 μ L	7.975 mL	0	0	0
2			0.000875	3.70×10^4	9.52×10^{-5}
3			0.001563	7.40×10^4	1.90×10^{-4}
4			0.0125	6.02×10^5	1.55×10^{-3}
5			0.05	2.31×10^6	5.95×10^{-3}
6			0.15	6.94×10^6	1.79×10^{-2}
7			0.2	9.26×10^6	2.38×10^{-2}
8	35 μ L	7.965 mL	0	0	0
9			0.001225	5.67×10^4	1.46×10^{-4}
10			0.002188	1.01×10^5	2.60×10^{-4}
11			0.0175	8.10×10^5	2.08×10^{-3}
12			0.07	3.24×10^6	8.33×10^{-3}
13			0.21	9.72×10^6	2.50×10^{-2}
14			0.28	1.30×10^7	3.33×10^{-2}
15	200 μ L	7.8 mL	0	0	0
16			0.007	3.24×10^5	8.33×10^{-4}
17			0.0125	6.02×10^5	1.55×10^{-3}
18			0.2	4.63×10^6	1.19×10^{-2}
19			0.4	1.85×10^7	4.76×10^{-2}
20			1.2	5.55×10^7	1.43×10^{-1}
21			1.6	7.40×10^7	1.90×10^{-1}

Table 3.2. Levels of alginate and water for each corresponding level of chitosan

Each sample for this set of experiments was tested only in the Horiba Jobin Yvon fluorescence spectrometer.

Each sample for both sets was also photographed under an optical microscope using the Zeiss Axio Lab.A1. Approximately 50 μ L of sample was spread out in the

depression on a concavity slide. Each image was taken with AxioVision software under 50x magnification.

3.3 Results

3.3.1 Interaction Regime Boundaries

There are three distinct interaction regimes present in the interaction profile of the alginate and chitosan particles. The first is a “dispersed, uncoated” regime where discrete alginate microparticles are partly coated by chitosan nanoparticles. There is too low a ratio of chitosan to alginate for the alginate particles to be loosely bonded together by networks of chitosan particles. The second regime is an “agglomerated” regime where there is an intermediate ratio of chitosan to alginate particles. In this regime, multiple alginate microparticles are connected into large clusters by many chitosan nanoparticles. Finally, there is a “dispersed, coated” regime, where there is sufficient chitosan on the surface of the alginate particles to start pushing them apart into a discrete particle suspension once again. Evidence from optical microscopy is used to show where the chitosan level boundaries are for each level of alginate.

The first alginate level tested was 2.31×10^6 (0.05g) alginate particles. As seen in Figure 3.1, at a level of 3.06×10^{10} (6.25 μ L) chitosan particles, alginate particles are clearly dispersed and since the chitosan level is too low for any aggregates to form it is in the dispersed, uncoated regime.



Figure 3.1. Microscope image of a sample mixture of 2.31×10^6 (0.05 g) alginate particles and 3.06×10^{10} (6.25 μL) chitosan particles. The sample is in the dispersed, uncoated regime

At a chitosan level of 6.11×10^{10} (12.5 μL) particles, we see the first sign of borderline agglomeration. At 1.22×10^{11} (25 μL) chitosan particles, we see definitive agglomeration. This is where the interaction regime boundary between dispersed, uncoated and agglomerated is located for 2.31×10^6 (0.05 g) alginate particles (Figure 3.2).

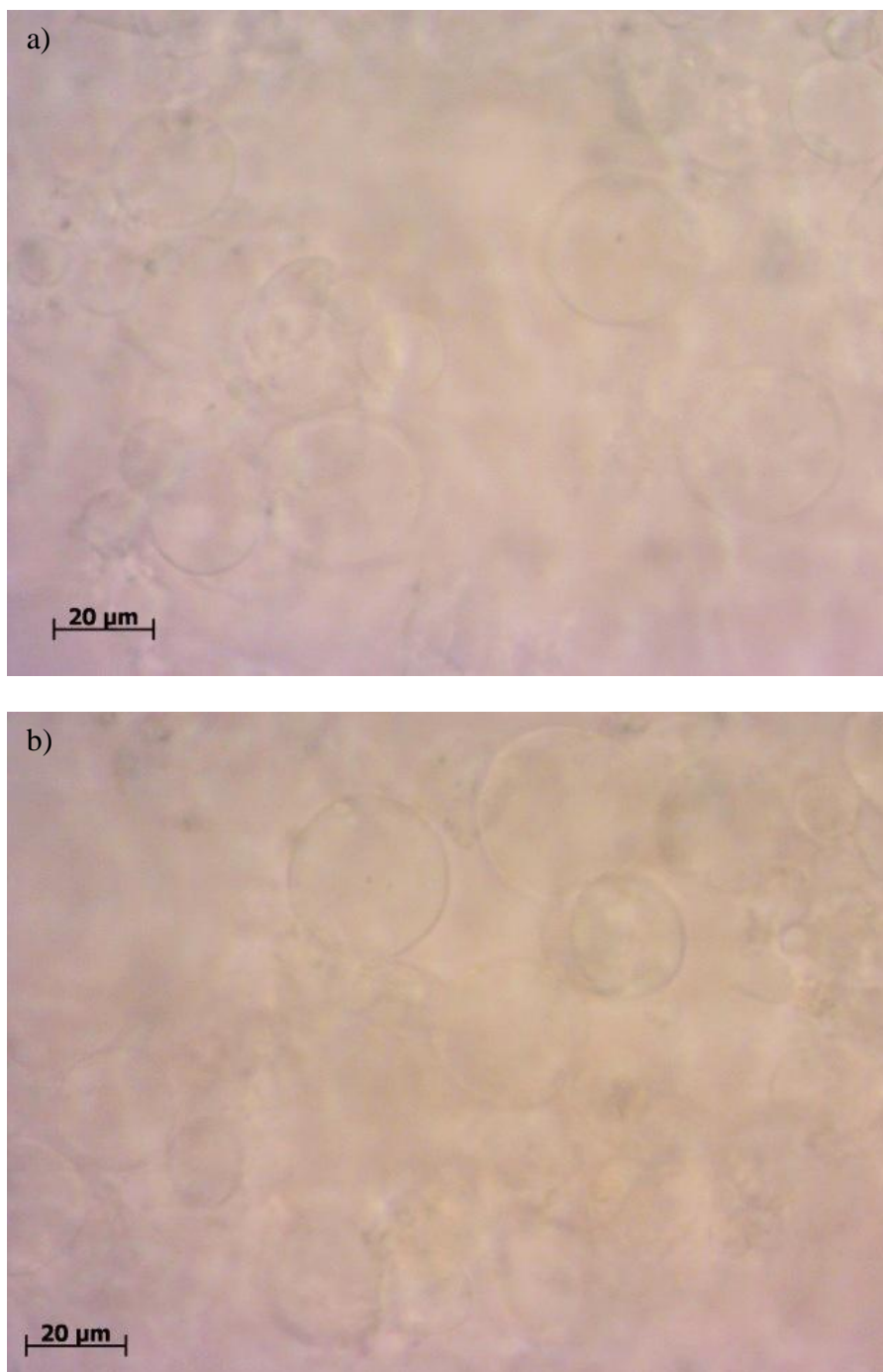
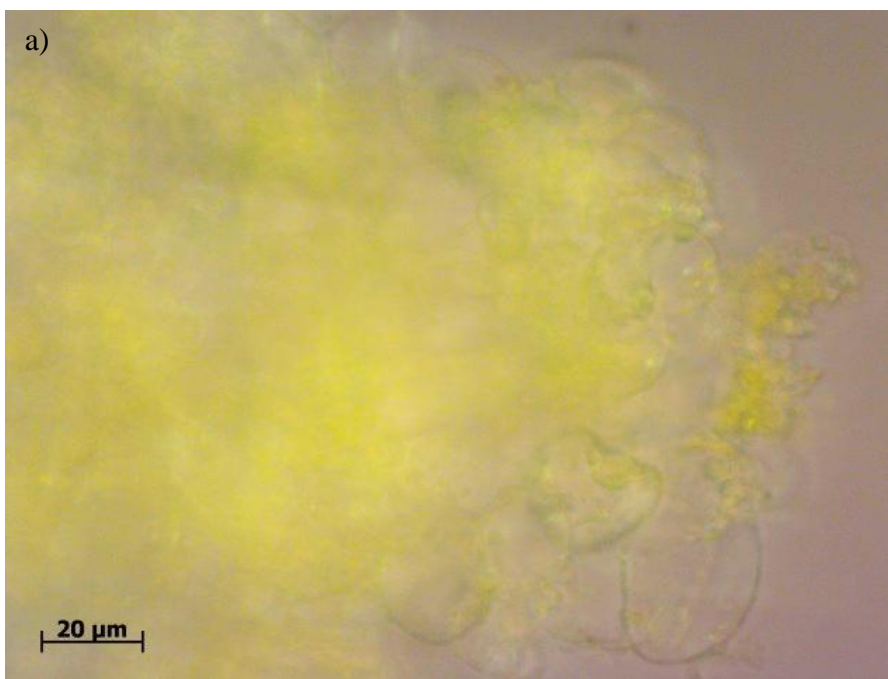


Figure 3.2. Microscope images of sample mixtures of (a) 2.31×10^6 (0.05 g) alginate particles and 6.11×10^{10} (12.5 μL) chitosan particles and (b) 2.31×10^6 0.05 μL alginate particles and 1.22×10^{11} (25 μL) chitosan particles. This is the dispersed, uncoated/agglomerated regime boundary.

The agglomerated regime continues through the level of 9.78×10^{11} (200 μL) chitosan particles. The picture shows a greenish yellow tint to the agglomerate which is a sign of fluorescing molecules. At 1.96×10^{12} (400 μL) chitosan particles we see that the alginate particles are starting to disperse again. The picture has particles with a darker yellow tint indicating a quenching of fluorescence occurring. The darker yellow color is the natural color of the tagged chitosan when it is not fluorescing. These two levels mark the interaction regime boundary between agglomerated and coated dispersed (Figure 3.3).



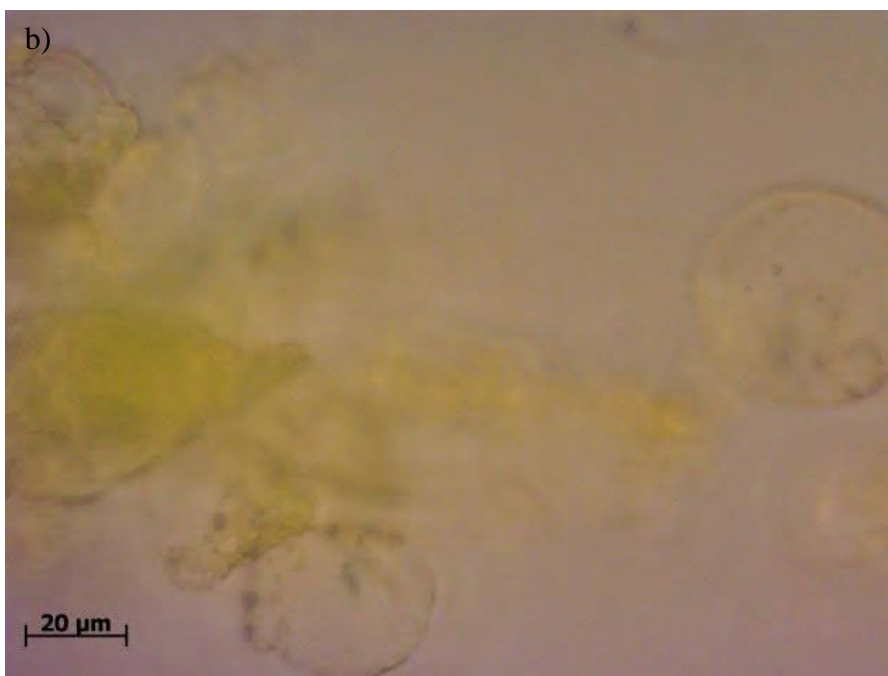


Figure 3.3. Microscope images of sample mixtures of (a) 2.31×10^6 (0.05 g) alginate particles and 9.78×10^{11} (200 μL) chitosan particles and (b) 2.31×10^6 (0.05 g) alginate particles and 1.96×10^{11} (400 μL) chitosan particles. This is the agglomerated/dispersed, coated interaction regime boundary.

The samples with chitosan particle levels of 3.91×10^{12} (800 μL) or higher are very clearly dispersed. They also have particles with a yellowish orange tint to them which again indicates that a significant fraction of the particles are not fluorescing (Figure 3.4).

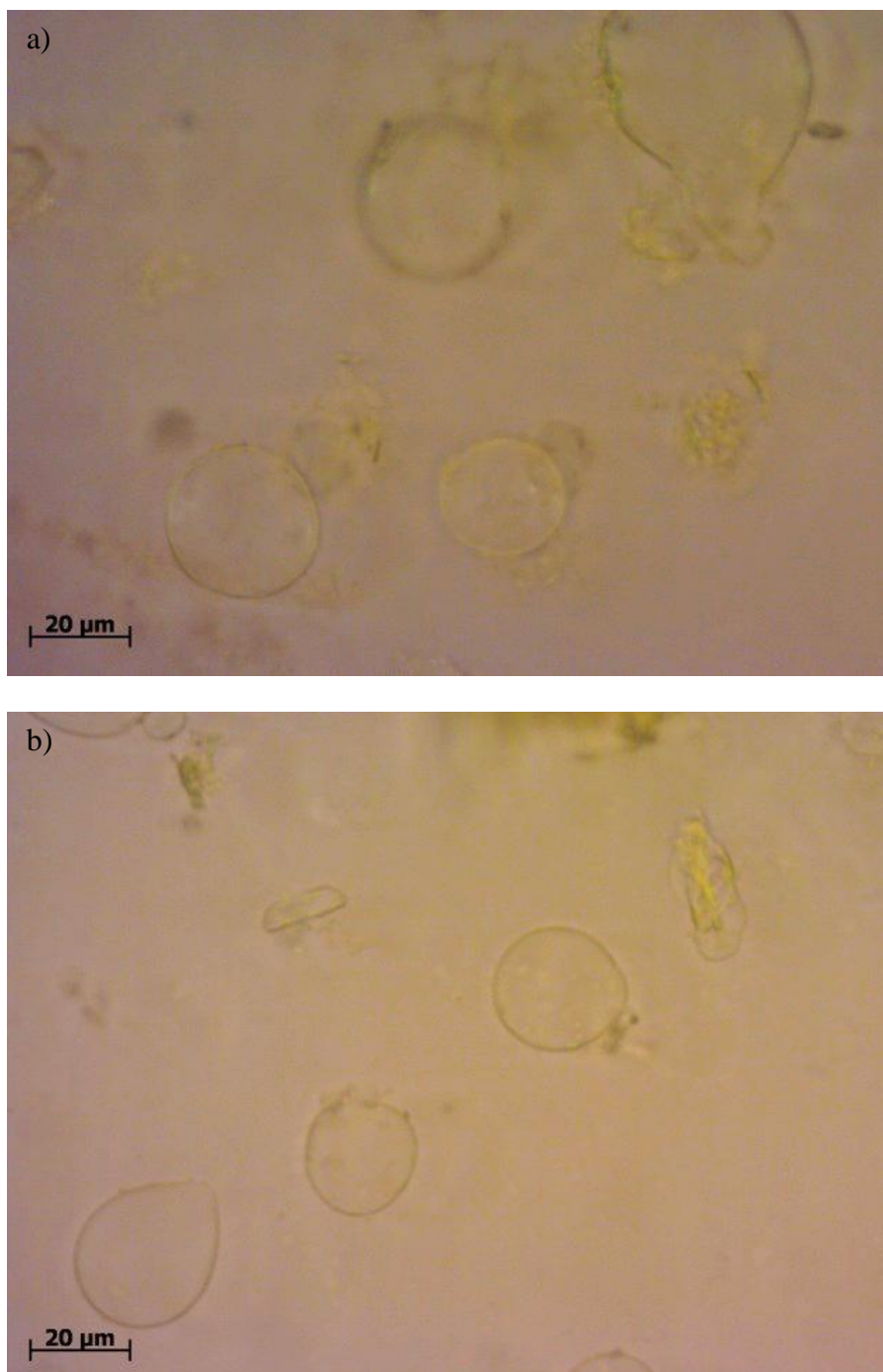
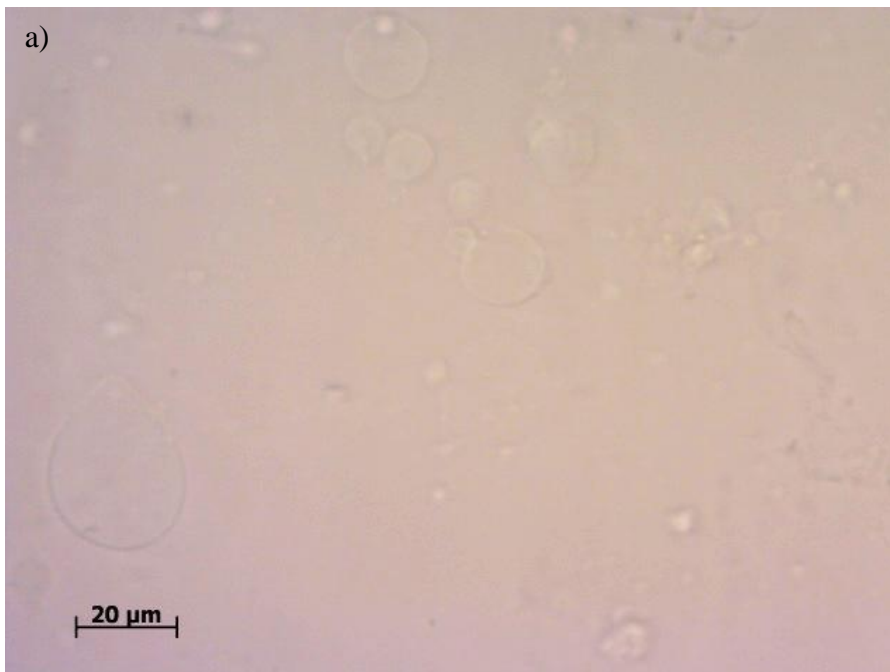


Figure 3.4. Microscope images of samples mixtures of (a) 2.31×10^6 (0.05 g) alginate particles and 3.91×10^{12} (800 μL) chitosan particles and (b) 2.31×10^6 (0.05 g) alginate particles and 7.82×10^{12} (1600 μL). The samples are in the dispersed, coated interaction regime.

The next alginate level tested was 4.63×10^6 (0.1 g) particles. As shown in Figure 3.5, there was a very distinct dispersed, uncoated/agglomerated interaction regime boundary between the chitosan levels of 1.22×10^{11} (25 μL) and 2.44×10^{11} (50 μL) particles.



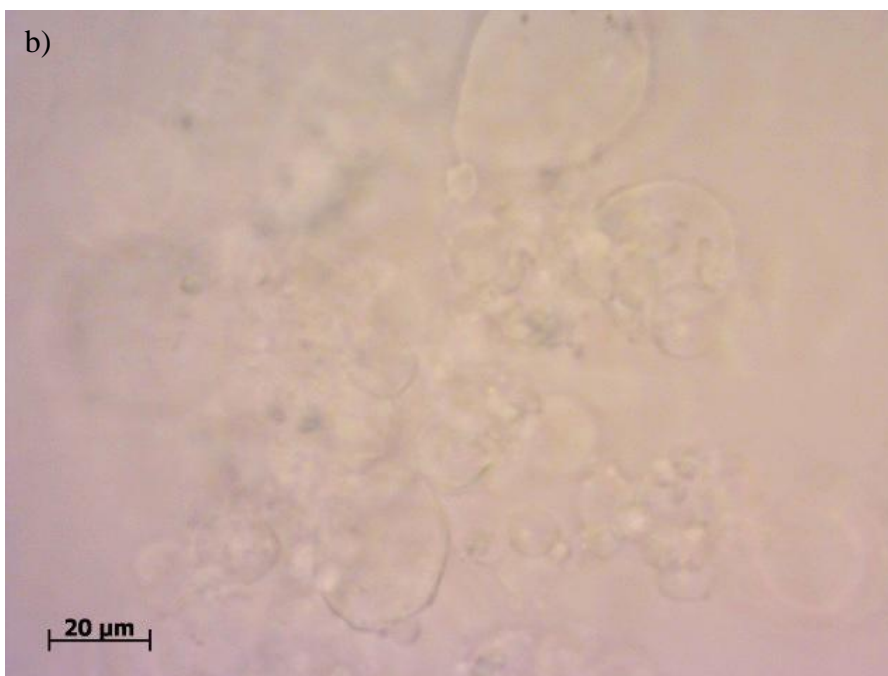


Figure 3.5. Microscope images of sample mixtures of (a) 4.63×10^6 (0.1 g) alginate particles and 1.22×10^{11} (25 μL) chitosan particles and (b) 4.63×10^6 (0.1 g) alginate particles and 2.44×10^{11} (50 μL) chitosan particles. This is the dispersed, uncoated/agglomerated interaction regime boundary.

The agglomerated interaction regime continues through the chitosan level of 1.96×10^{12} (400 μL) particles and switches to the dispersed, coated regime at 3.91×10^{12} (800 μL) particles (Figure 3.6). The 1.96×10^{12} (400 μL) particles level has a brighter yellow tint visually showing fluorescence and the 3.91×10^{12} (800 μL) particles level has a yellow-orange tint marking the beginning of fluorescence quenching.

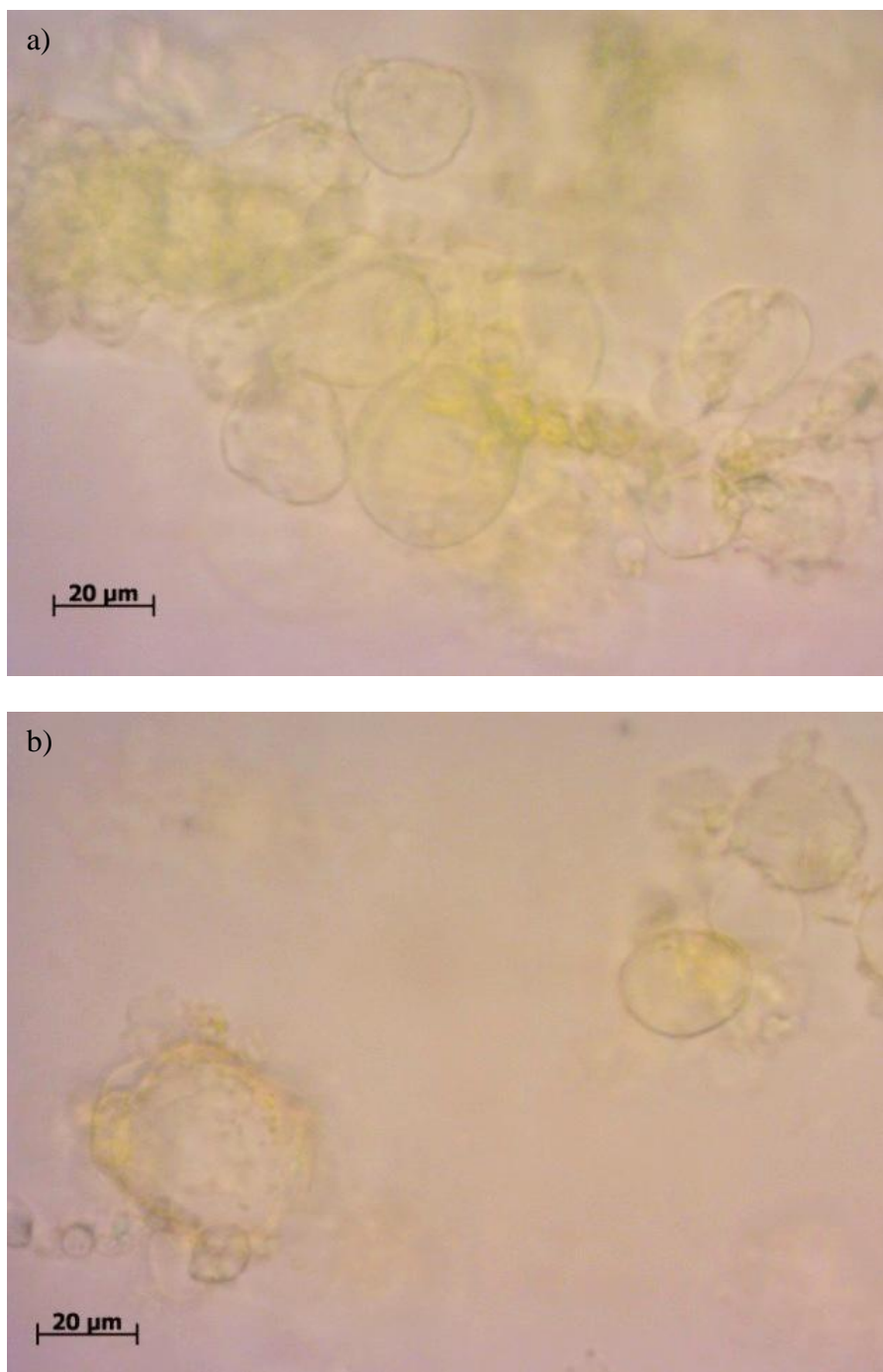


Figure 3.6. Microscope images of sample mixtures of (a) 4.63×10^6 (0.1 g) alginate particles and 1.96×10^{12} (400 μL) chitosan particles and (b) 4.63×10^6 (0.1 g) alginate particles and 3.91×10^{12} (800 μL) chitosan particles. This is the dispersed agglomerated/dispersed, coated interaction regime boundary.

The final alginate level tested was 9.26×10^6 (0.2 g) particles. As shown in Figure 3.7, the samples stay in the dispersed, uncoated regime through the chitosan level of 1.22×10^{11} (25 μL).

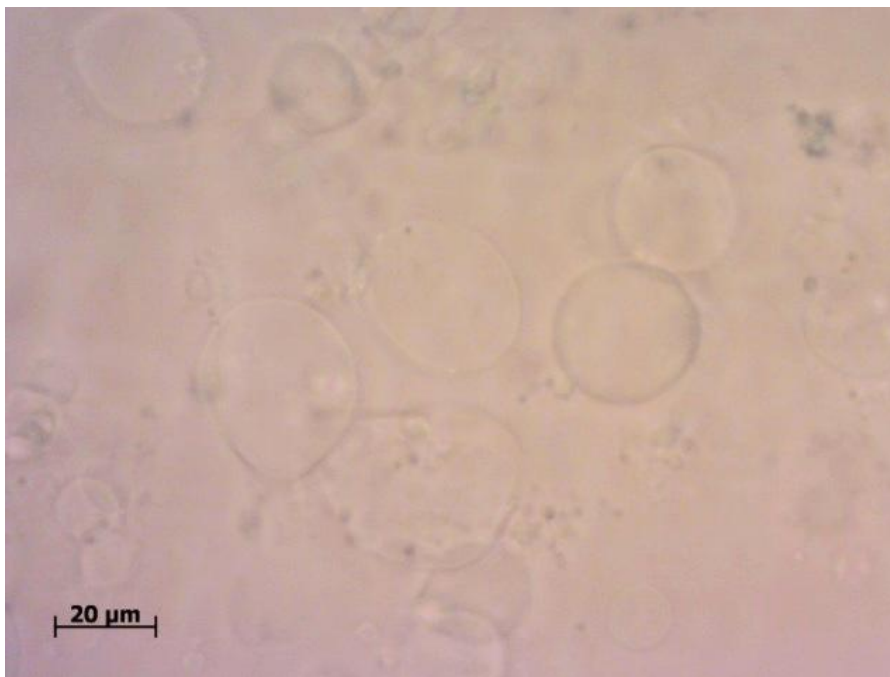


Figure 3.7 Microscope image of a sample mixture of 9.26×10^6 (0.2 g) alginate particles and 1.22×10^{11} (25 μL) chitosan particles. The sample is in the dispersed, uncoated interaction regime.

At 2.44×10^{11} (50 μL) chitosan particles, the particles start showing signs of agglomeration but it isn't until the chitosan level hits 4.89×10^{11} (100 μL) particles that they are clearly agglomerated. This is the approximate boundary between the dispersed, uncoated regime and the agglomerated regime (Figure 3.8).

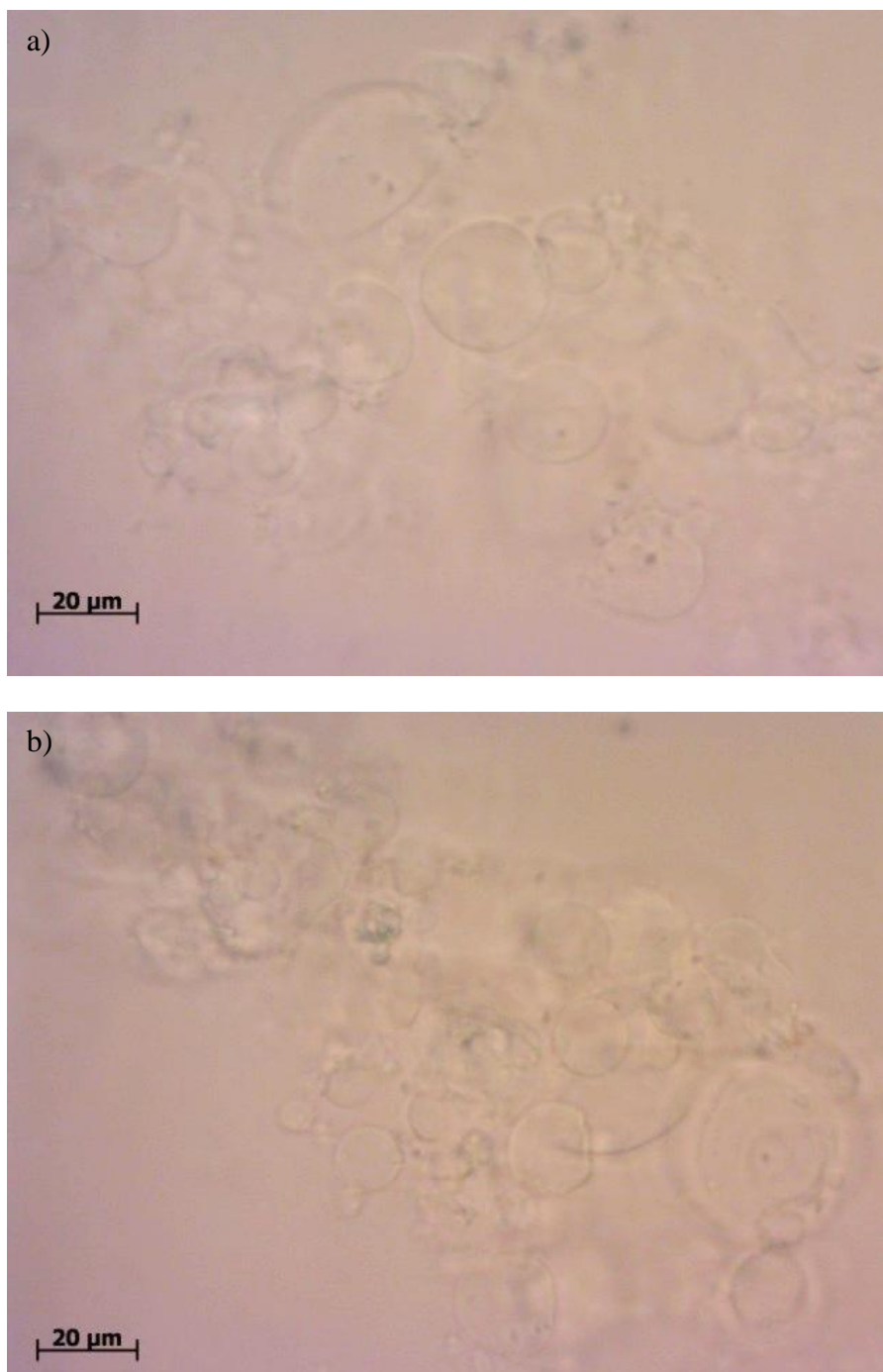
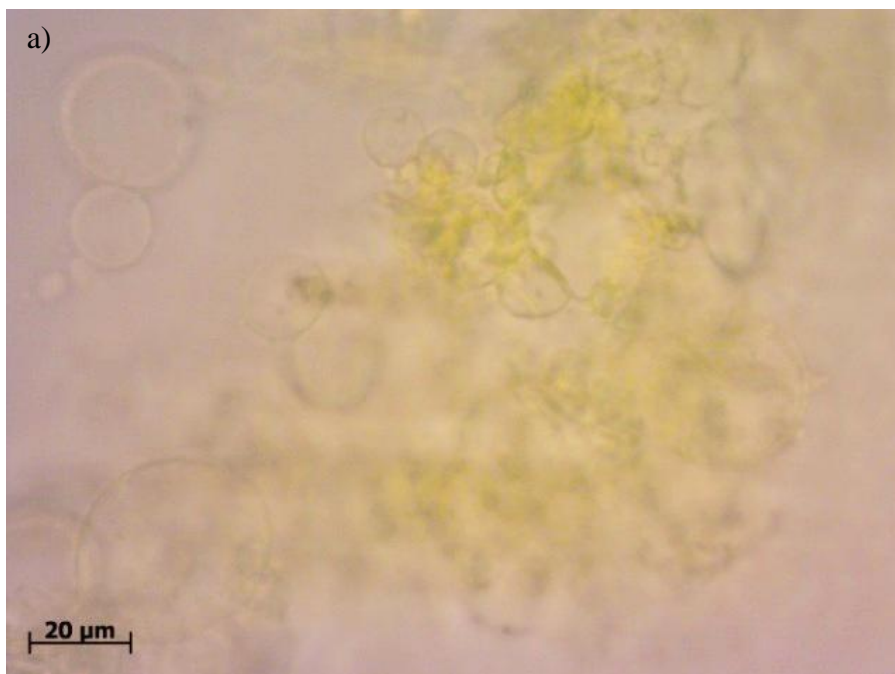


Figure 3.8. Microscope images of sample mixtures of (a) 9.26×10^6 (0.2 g) alginate particles and 2.44×10^{11} (50 μL) chitosan particles and (b) 9.26×10^6 (0.2 g) alginate particles and 4.89×10^{11} (100 μL) chitosan particles. This is the dispersed, uncoated/agglomerated interaction regime boundary.

The agglomerated regime continues until the level of 3.91×10^{12} (800 μL) chitosan particles. There is a bright yellow tint for this sample. The 7.82×10^{12} (1600 μL) chitosan particles sample is dispersed. There is more subdued yellow tint for this sample indicating more quenching (Figure 3.9).



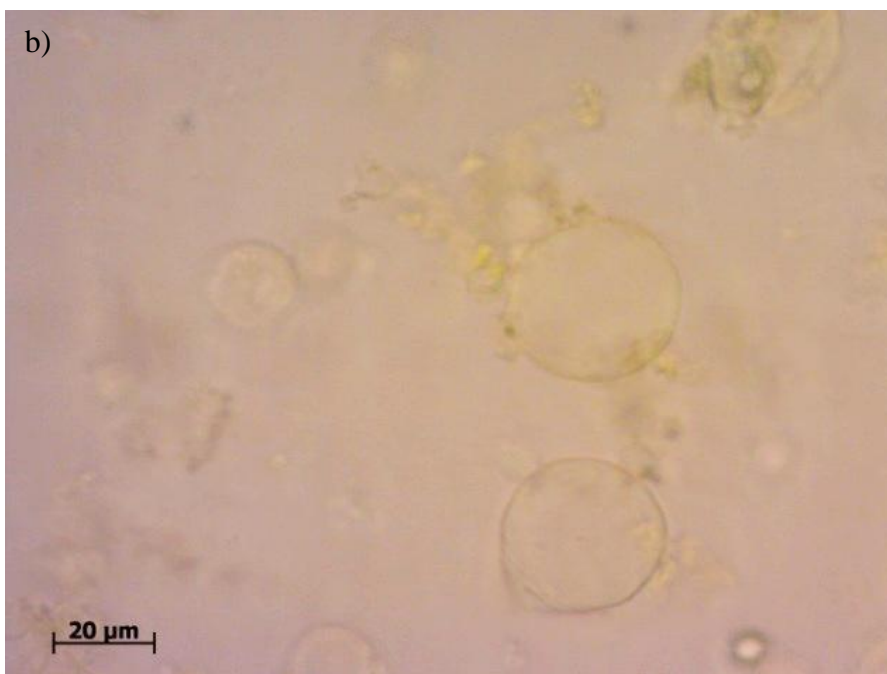


Figure 3.9. Microscope images of sample mixtures of (a) 9.26×10^6 (0.2 g) alginate particles and 3.91×10^{12} (800 μL) chitosan particles and (b) 9.26×10^6 (0.2 g) alginate particles and 7.82×10^{12} (1600 μL) chitosan particles. This is the agglomerated/dispersed, coated interaction regime boundary.

Figure 3.10 shows the resulting interaction regime diagram from all these results.

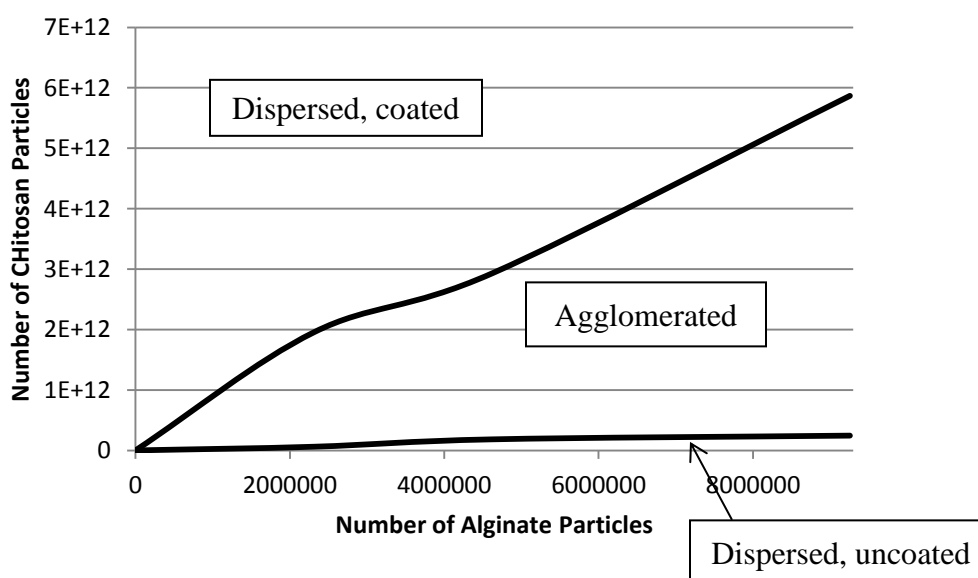


Figure 3.10. Resulting interaction regime diagram from experiments.

In comparison with the study of Gilchrist et al., the determined interaction boundaries in terms of the ratios of the number of nanoparticles to the number of microparticles are much larger than the ratios determined by Gilchrist et al. (2005). The observed difference arises because the other investigators had a much larger difference in zeta potential between their particles (-52mV and 95 mV vs. our 40 mV and -46 mV) and also a much smaller particle diameter ratio (59 for their work vs. 136 for this study).

3.3.2 Fluorescence Spectroscopy Results

Samples were first tested in the Ocean Optics fluorescence spectrometer. The samples' spectrum baseline kept increasing as samples were taken. In order to re-zero the data an average was taken of approximately where the baseline is at a zero value and that was subtracted from the measured intensity values. Intensity is the measure of emitted light collected by the detector. Intensity is a very instrument dependent value as each spectrometer uses different numbers for the same level of emitted light. An example of an early raw spectrum generated by the instrument with the baseline re-zeroed is seen in Figure 3.11a. There is also a graph of a zoomed in region from wavelength of 500 nm to 650 nm in Figure 3.11b.

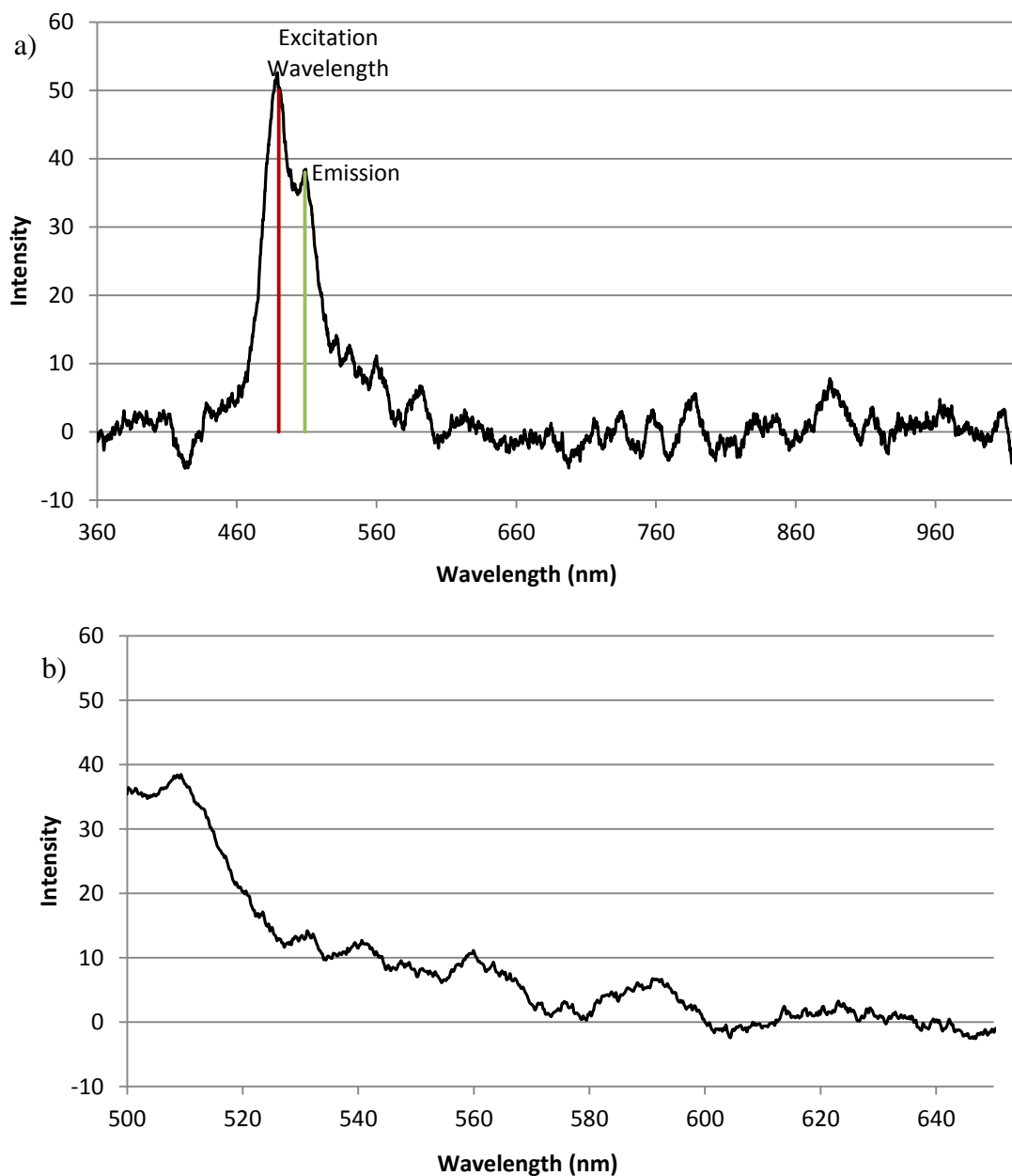


Figure 3.11. (a) Initial re-zeroed raw spectrum data for sample 4.36×10^6 (0.1 g) alginate particles and 1.96×10^{12} (400 μ L) chitosan particles. (b) The zoomed in region from 500-650 nm.

The data was fairly noisy but in initial tests there was a clear fluorescent signal. This proved not to be the case when a different batch of FITC was used in the tagging

procedure. There is no distinguishable emission peak distinct from the excitation peak (Figure 3.12).

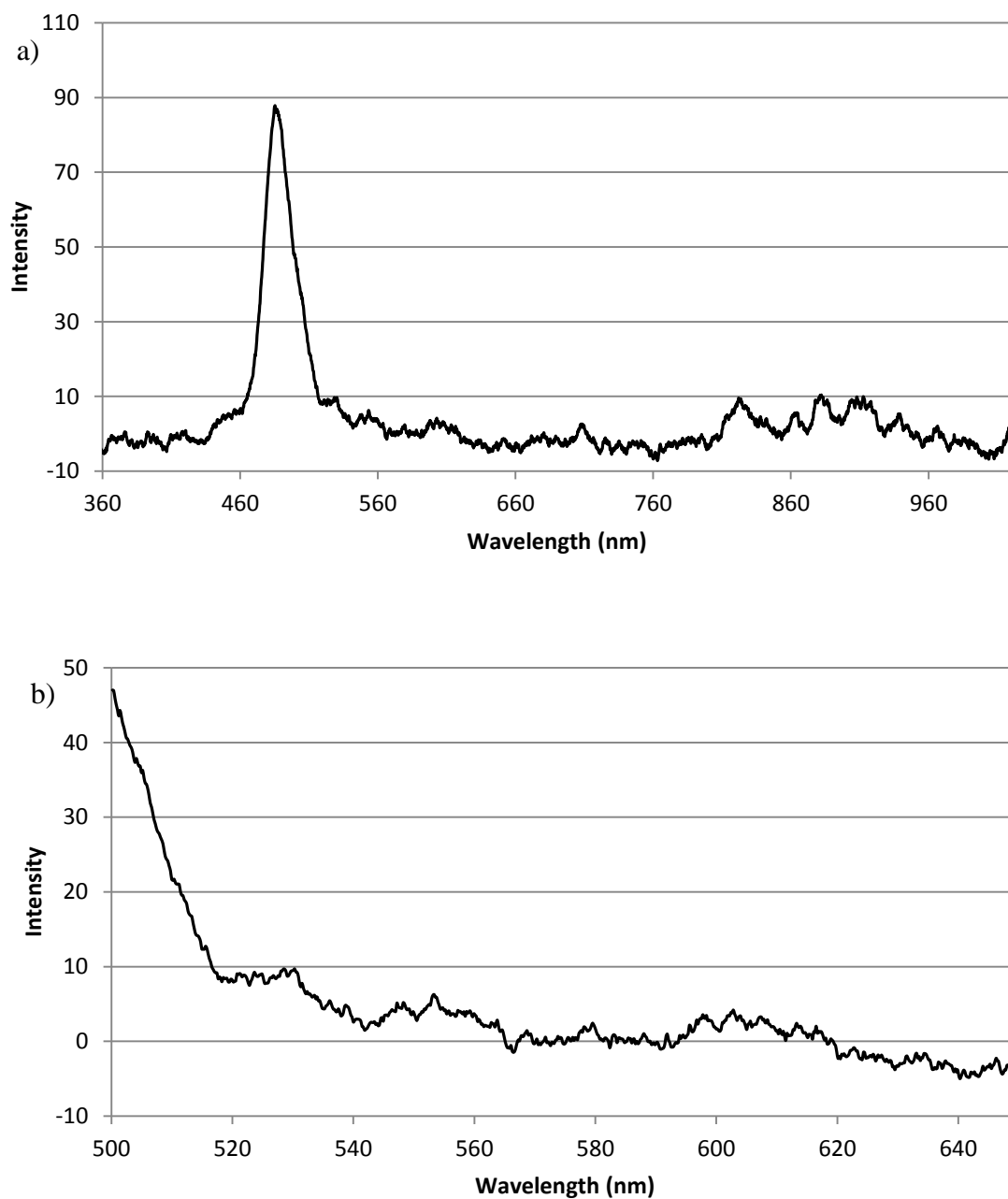


Figure 3.12. Re-zeroed raw spectrum data for new batch of FITC tagged chitosan particles at a level of 4.36×10^6 (0.1 g) alginate particles and a level of (a) 1.96×10^{12} (400 μ L) chitosan particles. (b) The zoomed in region from 500-650 nm.

The reason for this signal detection issue is two-fold. First, the new batch of FITC was not as efficient as tagging the chitosan as the first batch. Second, as there are fewer tagged chitosan particles there are far more that are reflective. That is the reason for the larger excitation peak. The larger excitation peak indicates higher scattering and prevents the fluorescent peak from being visible.

In order to deal with these issues, samples were then tested in the Horiba Jobin Yvon fluorescence spectrometer. The idea was to take advantage of the outgoing monochromator to filter out scattered light from the excitation wavelength and to have a more sensitive instrument with a better signal to noise ratio to see the fluorescence peak better. An example of a raw spectrum from the Horiba Jobin Yvon fluorescence spectrometer is shown in Figure 3.13.

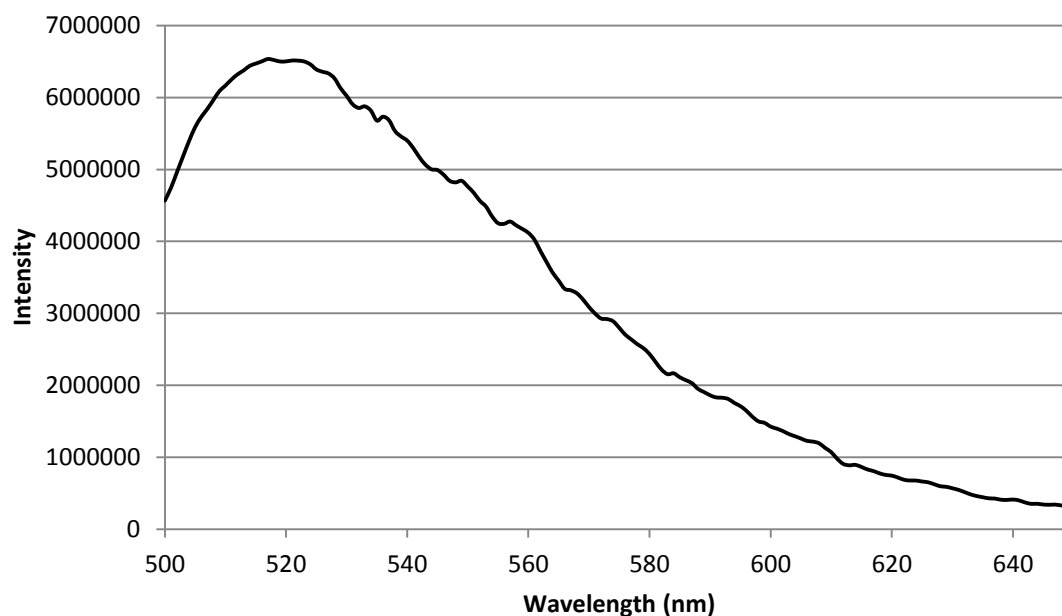


Figure 3.13. Raw spectrum data for sample 4.36×10^6 (0.1 g) alginate particles and 1.96×10^{12} (400 μ L) chitosan particles.

The peak is much more clearly defined compared to the peaks in the previous Ocean Optics spectrometer measurements. The Horiba data is very reproducible due to the smaller amount of noise. These spectra were generated for every tested sample.

For each spectrum, the area under the curve from the maximum value to the half maximum value was calculated using the trapezoidal rule. These integrated intensities were averaged over 3 trials for each level of chitosan and alginate. The results for the constant alginate and varying chitosan are seen in Figure 3.14.

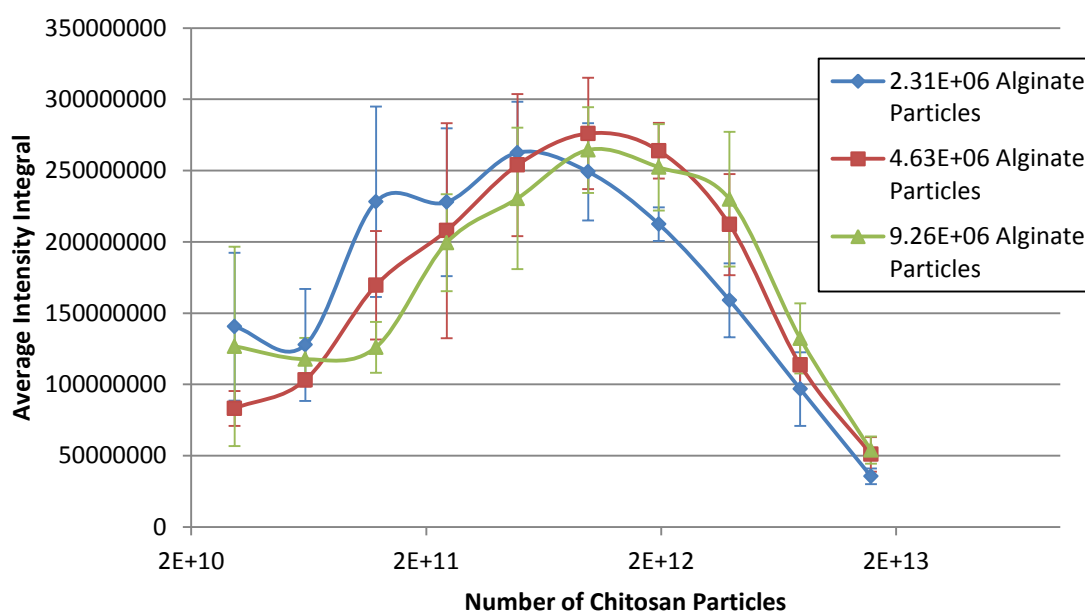


Figure 3.14. The average intensity integral from the maximum intensity to the half maximum intensity for each constant alginate level plotted against the number chitosan particles.

The interaction regime transition from dispersed, uncoated to agglomerated, at relatively low numbers of chitosan particles, is not very clear from the plot. There are too many

shoulders in the intensity curve for it to be clear which one indicates a transition. Meanwhile, the transition from agglomerated to dispersed, coated seems to be indicated by the first large drop in signal intensity at relatively high numbers of chitosan particles. The signal continues to drop with increasing amount of fluorescent chitosan for all of the alginate levels, suggesting that the inner filter effect is occurring, where fluorescent molecules close to the cuvette surface absorb most of the excitation light preventing those in the center of the cuvette (and providing the larger signal reaching the detector) from being excited and emitting a signal (Lakowicz, 2007). It is not fully clear from this data set whether the first large drop in signal intensity is due to the transition or simply a residual inner filter effect.

In order to further understand the cause of the intensity drop, the average maximum to half maximum intensity integral was plotted against the ratio of the number of alginate particles to chitosan particles (Figure 3.15).

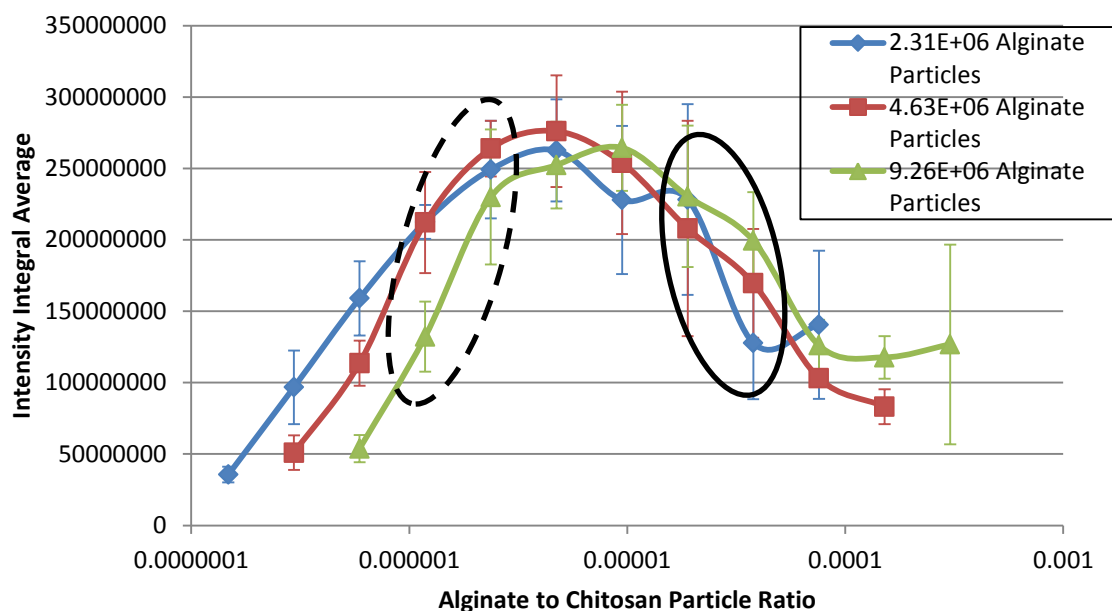


Figure 3.15. Average maximum to half maximum intensity integral plotted against the ratio of alginate to chitosan particles for constant alginate levels with the points for the interaction regime transitions from dispersed, coated to agglomerated (dashed) and agglomerated to dispersed, uncoated (solid) circled.

Here again, the dispersed, uncoated and agglomerated transition is not well indicated due to the large error in the results. The dispersed, coated and agglomerated transition is again indicated by a large drop but the intensity value drop of the 9.26×10^6 alginate particles level (0.2 g) at the transition is significantly larger magnitude than the drop of 2.31×10^6 (0.05 g) and 4.63×10^6 (0.1 g). This difference indicates that the inner filter effect is playing a significant role in the signal decrease, at least for the 9.26×10^6 particle level. As the decrease in signal is the largest for the most concentrated system, it is likely that fluorescent chitosan particles at a much higher number in the system absorb much more of the emitted light as compared to the two lower alginate values at the same ratio.

In order to further understand the mechanism for the observed trends in fluorescence intensity, fluorescence spectra were taken of samples with constant amounts

of chitosan and varying amounts of alginate. Spectra were taken from two alginate levels within each interaction regime as well as from the zero alginate point (used as a control). The number ratio of alginate to chitosan particles was the parameter varied for each chitosan level. The area under the curve from maximum to half maximum intensity of each spectrum averaged over three trials was plotted against the ratio of the number of alginate to chitosan particles (Figure 3.16).

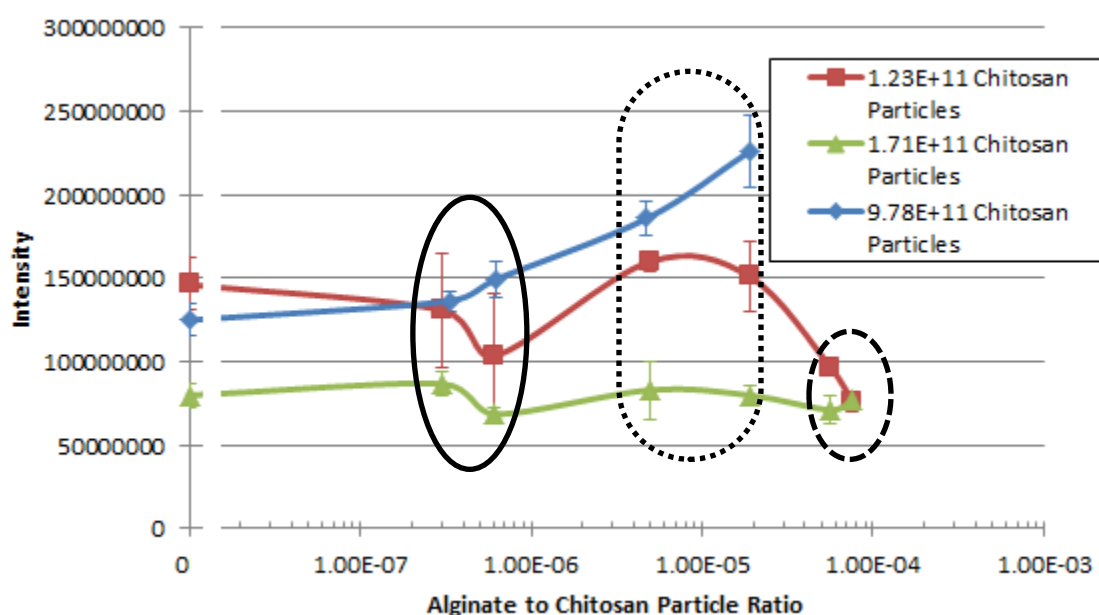


Figure 3.16. Average maximum to half maximum intensity integral plotted against the ratio of alginate to chitosan particles for constant chitosan levels. The dispersed, coated regime (—), the agglomerated regime (...), and the dispersed, uncoated regime (---) are circled.

The intensity values of the alginate in the dispersed, coated regime are lower than the control value in the 1.23×10^{11} chitosan particles (25 μL) and the 1.71×10^{11} chitosan particles (35 μL) as the system approaches the boundary of the agglomerated regime. In the limit that the ratio approaches zero in the dispersed, coated regime (i.e. minuscule

concentration of alginate), the intensity value is at that of the control. For the agglomerated regime at the two lower chitosan levels, the intensity values are approximately at the level of the control. The pattern of the intensity values of the two lower levels diverge in the dispersed, uncoated regime. For 1.23×10^{11} chitosan particles (25 μL), the more alginate there is, the lower the signal. That is only true for the 9.71×10^6 alginate particles (0.21 g) at the 1.71×10^{11} chitosan particles (35 μL) level which is an alginate to chitosan particle ratio of 5.68×10^{-5} . For the 1.30×10^7 (0.28 g and a particle ratio of 7.57×10^{-5}) alginate particle level the intensity rises again. This observed difference is due to a lower initial (zero alginate) signal from the (35 μL) level chitosan particles which allowed scattering from the alginate particles to affect the results. The preparation method of the chitosan particles induces a general variability in signal intensity due to varying tagging efficiency. Each batch of fluorescently tagged chitosan can yield a different signal intensity. For this reason, the raw signal intensity of 1.71×10^{11} chitosan particles (35 μL) with zero alginate is significantly lower than that of 1.23×10^{11} chitosan particles (25 μL), since the chitosan particles were synthesized from different tagged chitosan batches. The 9.78×10^{11} chitosan particles (200 μL) level has the same initial (zero alginate) signal as that of the 1.23×10^{11} chitosan particles level, but since the chitosan particles were produced from the same tagged chitosan batch this is probably due to the inner filter effect as otherwise the signal should be approximately 8 times higher for the 9.78×10^{11} particle level. For the 9.78×10^{11} chitosan particles (200 μL) the signal simply rises with alginate to chitosan ratio, due to the excess scattering caused by the alginate in the system. A distinct fluorescence signal cannot be discerned from the data for the dispersed, coated and agglomerated regimes. The dispersed,

uncoated data did not provide any noticeable fluorescence peak and accordingly were not shown in the plot.

In conjunction with the microscope images, these results suggest that as chitosan particles adsorb on to the surface of the alginate particles, the fluorescence intensity is significantly quenched. The quenching is particularly severe in the dispersed, uncoated regime, where virtually all of the chitosan particles are adsorbed on to the alginate particles. In the agglomerated regime there is a significant amount of unadsorbed chitosan found in large clusters, leading to intensity values that match the control. When the agglomerates transition to the dispersed, coated particles, most of the chitosan is bound to the surface of the alginate particles. However, as the alginate to chitosan particle ratio decreases, there is more unbound chitosan in free suspension surrounding the coated alginate particles and the intensity values start to approach the control values again. The effect of quenching is clearer when the intensity values are normalized to the control (Figure 3.17).

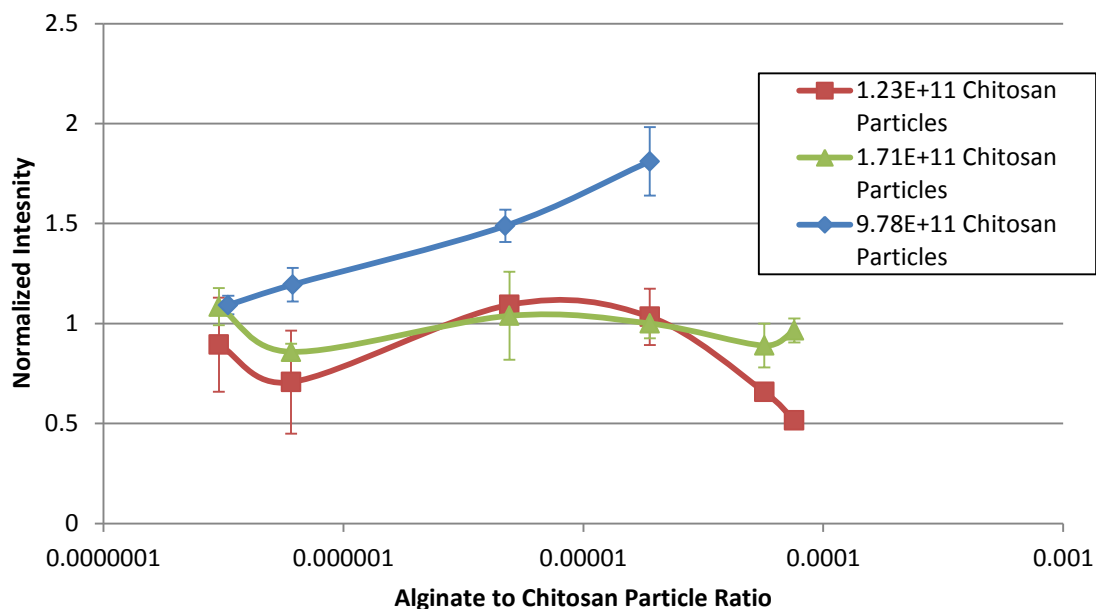


Figure 3.17. Average maximum to half maximum intensity integral normalized to zero alginate value plotted against the ratio of alginate to chitosan particles for constant chitosan levels

The two lower chitosan curves follow the same pattern until scattering from alginate particles mixes with the fluorescent signal for the latter points of 1.71×10^{11} chitosan particles (35 μL). It is also clearer that scattering overwhelms the signal for 9.78×10^{11} chitosan particles (200 μL). These results prove that as long as scattering is low and the fluorescence signal is not severely attenuated by the inner filter effect, fluorescence spectroscopy is capable of distinguishing among all of the major interaction regimes. Thus, varying chitosan concentration data can be used to determine threshold values for the change in interaction regime from agglomerated to dispersed, coated.

The varying chitosan data have an issue that as fluorescent intensity is variable for each purchased batch of FITC due to differences in tagging efficiency, there needs to be a method to allow all plots to be compared regardless of peak fluorescence. We therefore normalized each intensity integral (maximum to half maximum integral) to the maximum

value of the set of calculated values over each experimental run – a run being 1 trial of a single alginate level at all 10 chitosan levels. These normalized points were averaged over 3 trials and then plotted to the logarithm of the chitosan levels (Figure 3.18).

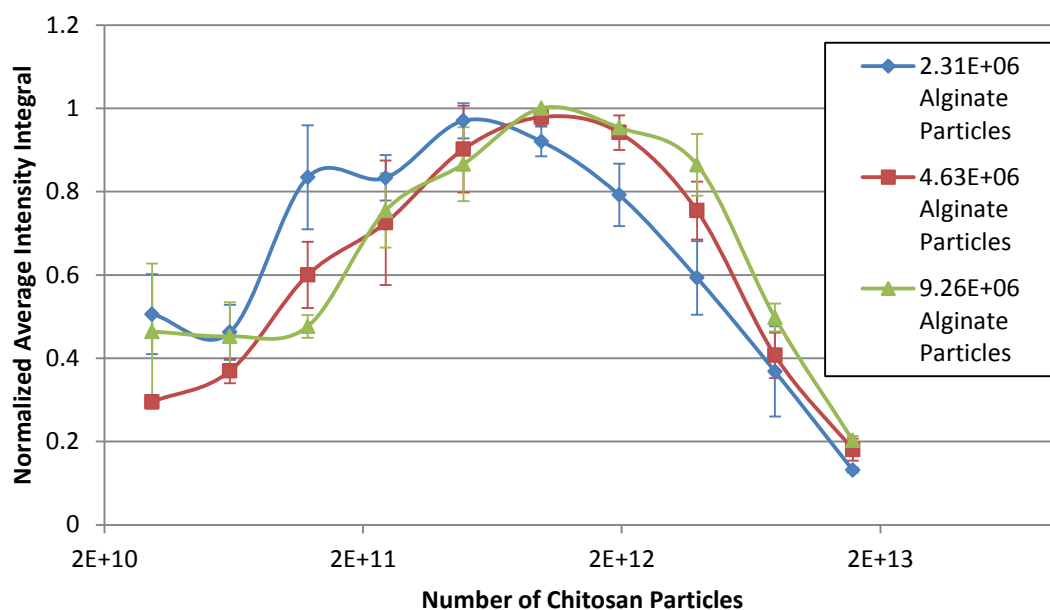


Figure 3.18. Normalized maximum to half maximum intensity integral plot

The normalized plots follow a similar pattern to the previous plots with the difference being that the 9.26×10^6 regime boundary is better illustrated even though there is an issue with the inner filter effect for the drop in intensity.

To quantify the interaction regime boundary the slope of the normalized average integral of the maximum to half maximum intensity was calculated. The change in the normalized average intensity was divided by the change in the natural logarithm of the

number of chitosan particles. A plot of these values was created to determine the slope where the interaction regime boundary is indicated (Figure 3.19).

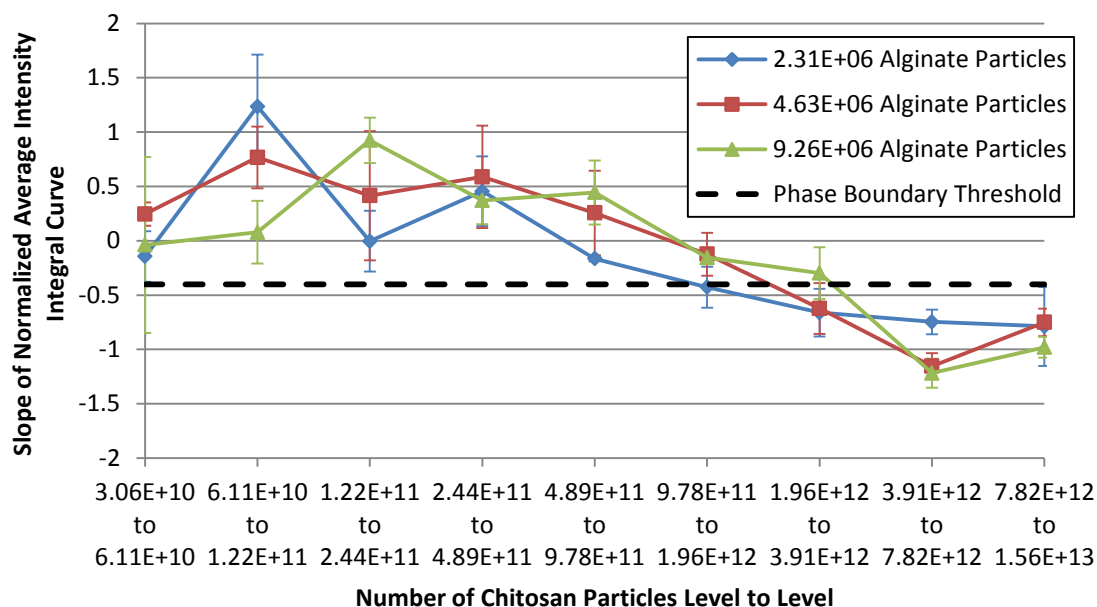


Figure 3.19. Plot of the slope of the maximum intensity to half maximum intensity integral curve from chitosan level to chitosan level.

From this plot, it is evident that the interaction regime boundary threshold for the switch from the agglomerated regime to the dispersed, coated regime is marked by a slope value of -0.4 for the change of the normalized average maximum to half maximum integral. The meaning of this value is that significant self-quenching is evident in the changing intensity values. The fluorescent chitosan particles have come into close contact as the transition to the dispersed, coated regime occurs.

3.4 Discussion

Once fluorescence spectroscopy was proven to distinguish the particle interaction regime boundaries, we aimed to gain understanding of why the regime boundaries were located at the designated particle ratios. Accordingly, we made several calculations using established particle interaction theory in its simplest forms. The first calculation was made in order to determine the number of chitosan particles required to adsorb on to the surface of an alginate particle to reach zero net surface charge. The equation for the surface charge density of a spherical particle is

$$q_s = \varepsilon_3 \varepsilon_0 \zeta \left(\frac{1}{a} + \kappa \right) \quad (3.1)$$

where ε_3 is the dielectric constant of the medium, ε_0 is the vacuum permittivity, $8.85 \times 10^{-12} \text{ Fm}^{-1}$, ζ is the zeta potential, a is the radius of the particle, and κ is the inverse Debye length (Hunter and White, 1987). At room temperature $\kappa = \sqrt{I}/0.304$ in nm^{-1} where I is the ionic strength of the solution (Hunter and White, 1987). The ionic strength of the solution was approximated as 10^{-5} M , which refers to the pH value of 5 of the chitosan suspensions. The expression for κ yields a Debye length of 96 nm. For the alginate calculations, the dielectric constant ε_3 is 80.1 for water, the zeta potential is -46 mV (Mladenovska et al., 2007), and the average particle radius is 17 μm . For the chitosan calculations, the medium is again water, so the same inverse Debye length and dielectric constant are used. The zeta potential for chitosan is 40 mV and the average particle radius is 125 nm. The total charge of an alginate particle is the surface area of a sphere multiplied by the surface charge density. The alginate particle is assumed to only interact with half of the surface charge of a chitosan particle since only one side of the chitosan adsorbs onto the alginate surface, and the other side is neutralized by the solution

counterions. Therefore, the half total the surface charge of a chitosan particle is divided by the total charge of an alginate particle. This quotient yields an alginate to chitosan particle ratio of 2.35×10^{-5} . This surface charge neutralization ratio lies directly in between the experimentally determined particle ratios of 1.89×10^{-5} and 3.79×10^{-5} that bookend the transition from the dispersed, uncoated regime to the agglomerated regime. The particle ratio resulting from this calculation suggests that that charge neutralization is the mechanism for the transition from the dispersed, uncoated regime to the agglomerated regime. If the electrostatic interactions between particles are eliminated by surface charge neutralization, only attractive van der Waals forces remain, driving the particles together toward aggregation.

A DLVO calculation was also developed in order to approximate the total interaction potential energy. The van der Waals attractive interaction energy was subtracted from the electrostatic repulsion energy. The electrostatic energy was calculated by the equation outlined in Furusawa (1999)

$$V_e = \frac{8R^2T^2\gamma^2\epsilon_3a}{Z^2F^2} \exp(-2\kappa x) \quad (3.2)$$

where $\gamma = \tanh\left(\frac{e\psi}{4kT}\right)$

Zeta potential (ζ) is used in place of surface potential (ψ) for simplicity since surface potential cannot be measured directly and cannot be accurately calculated. R is the ideal gas constant, T is temperature, ϵ_3 is the dielectric constant of water, Z is the ionic valency (-1 in this case), F is the Faraday constant, and x is the distance between particles. For alginate, the zeta potential is recalculated using equation 1 to be 57 mV. Alginate was treated as a large chitosan particle with full surface coverage. This assumes that when

covered, the alginate particle only shows the surface charge per unit area of the chitosan particles adsorbed to the surface. The total charge of the chitosan particles needed for full surface coverage is added to the total charge of one alginate particle and that number is divided by half the surface area of the chitosan particles adsorbed on the surface to get the surface charge density. Half the surface area is used since it is assumed that only half is exposed to the solution. This surface charge density value is used to back out the zeta potential that is used in the DLVO calculations for two interacting covered alginate particles. The measured value of 40 mV is used for the interaction between two chitosan particles.

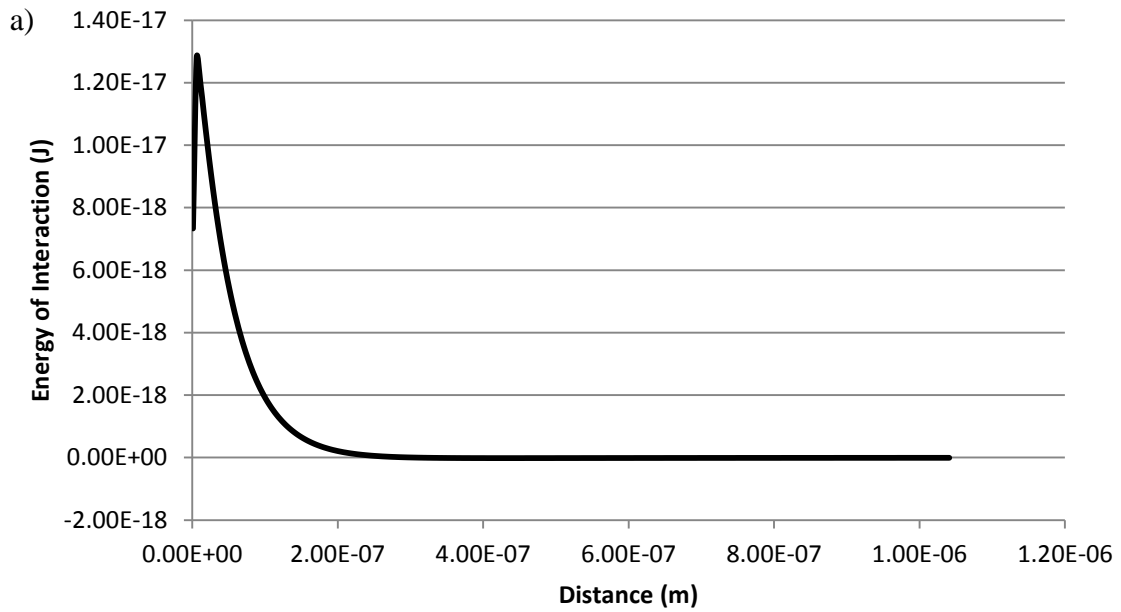
The van der Waals energy was calculated with a simple attraction of two spheres model using the Derjaguin approximation (Hunter and White, 1987)

$$V_a = \frac{Aa}{12x} \quad (3.3)$$

where
$$A = \frac{3}{4} kT \left(\frac{\varepsilon_1 - \varepsilon_3}{\varepsilon_1 + \varepsilon_3} \right)^2 + \frac{3h\nu_e}{16\sqrt{2}} \frac{(n_1^2 - n_3^2)^2}{(n_1^2 + n_3^2)^{3/2}} \quad \text{from Lifshitz theory}$$

(Israelachvili, 2010). The Derjaguin approximation is valid when two interacting spheres are large enough that they see each other as two flat plates at a small separation distance. This approximation is valid for interacting alginate microparticles but is less accurate for chitosan nanoparticles interacting with each other. ε_1 is the dielectric constant of the particle, h is the Planck constant, ν_e is the characteristic frequency of the medium (water), n_1 is the refractive index of the particle, n_3 is the refractive index of the medium. The dielectric constant of chitosan is the same as water since it is a hydrogel. The refractive index of chitosan is 1.47.

Now we aim to determine the maximum number of particles that can fit into a control volume while still experiencing attractive interactions. In order to calculate the minimum stable separation distance between two particles, first, curves are generated by subtracting the attractive van der Waals energy from the electrostatic repulsion energy which is calculated as a function of distance (Figure 3.20).



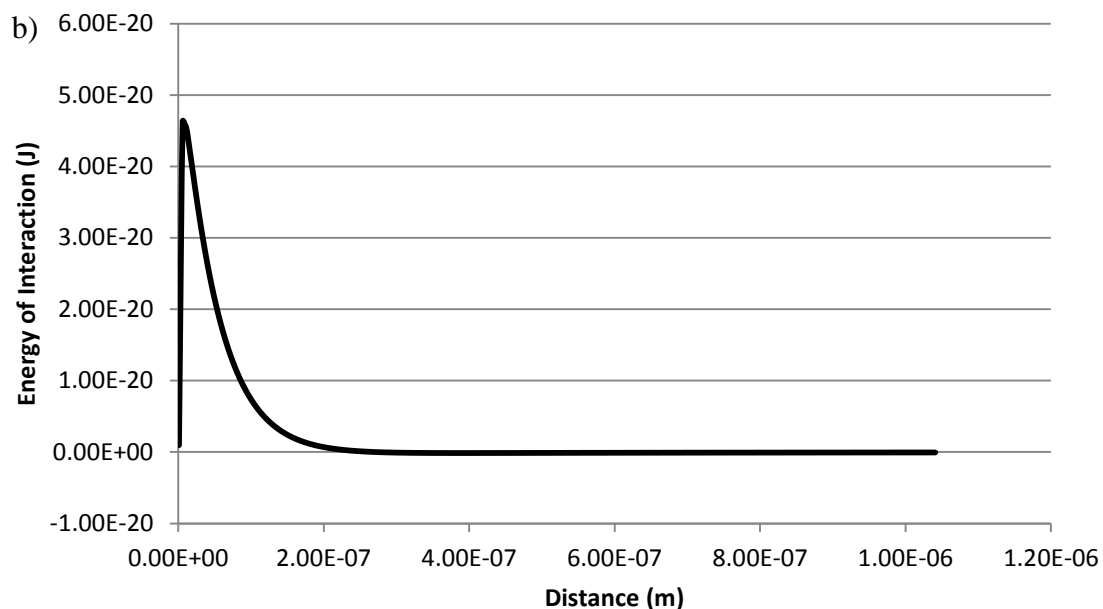


Figure 3.20. DLVO curves for (a) two interacting covered alginate particles and (b) two interacting chitosan particles.

The minimum stable separation distance is determined by the distance where the interaction energy changes from causing repulsion (positive values) to causing attraction (negative values). That distance represents the minimum distance of attraction, while particles repel if they are placed in closer proximity. For two fully coated alginate particles, the minimum stable separation distance is 311 nm. For two chitosan particles, the minimum stable separation distance is 271 nm.

In order to calculate the ratio of alginate to chitosan particles in an agglomerate, the maximum number of particles that can fit in a control volume of a 1 mm by 1 mm box is determined. First, a cubic lattice arrangement of particles is assumed. Then, using the alginate separation distance, the maximum number of alginate particles that can fit in the control volume is calculated based on a cubic lattice. Then the number of chitosan particles that can adsorb onto the surface of an alginate particle is determined by

assuming that each chitosan particle takes up an area of πr^2 of the alginate surface area, where r is the radius of the chitosan particle. This number is multiplied by the total number of alginate particles in the control volume. Afterward, the empty space in the control volume is calculated. Finally, it is assumed that chitosan fills the empty space in a cubic lattice and the number of free chitosan particles is calculated from the chitosan separation distance. The ratio of alginate particles to chitosan particles in the control volume is number of alginate particles divided by the free plus adsorbed chitosan particles. This ratio of alginate particles to chitosan particles was 2.78×10^{-6} , which is close to an experimentally determined regime transition boundary. The ratios of 1.18×10^{-6} and 2.37×10^{-6} mark the transition from the agglomerated to dispersed, coated regime in the experiments.

Regime Transition	Experimental	Calculated
Dispersed, uncoated to agglomerated	In between 1.89×10^{-5} and 3.79×10^{-5}	2.35×10^{-5}
Agglomerated to dispersed, coated	In between 1.18×10^{-6} and 2.37×10^{-6}	2.78×10^{-6}

Table 3.3. Comparison of experimental and calculated interaction regime transition boundaries shown as ratio of alginate particles to chitosan particles.

A comparison of the two ratios we estimated as the boundaries of the agglomerated regime indicates that a large amount of unadsorbed chitosan accumulates inside the agglomerates. The significant presence of unadsorbed chitosan is also indicated by the microscope pictures, where large yellow clusters or clouds are visible surrounding the alginate particles. The calculated ratio of unadsorbed to adsorbed chitosan particles at minimum stable separation distances in the control volume is 3.87 to 1. The

preponderance of unadsorbed chitosan in the agglomerates can explain the fluorescence results, as the signal is lower for the regimes where there is strong adsorption to the alginate particle surface, while it jumps up back to approximately the control value for the agglomerates, where a significant fraction of the chitosan is unadsorbed.

As a side note, a very simplistic assumption of a monolayer of adsorbed chitosan particles was used which could explain why the calculated alginate to chitosan ratio is slightly higher than in experimental values. The alginate and chitosan particles are not hard spheres but very porous hydrogels. The exposed alginate surface area could be larger and lead to a higher calculated zeta potential which would then increase the minimum distance of separation. A greater alginate separation distance would yield fewer alginate particles in the control volume which would lead to a lower, more accurate ratio, on the order of the experimental results.

These approximate calculations provide an explanation for the mechanisms leading to the different interaction regimes. For the dispersed, uncoated regime, the electrostatic repulsion among the alginate particles is still higher than van der Waals attraction, even with adsorption of chitosan on the alginate surface. Thus, the alginate particles stay dispersed. In the agglomerated regime, the electrostatic repulsion of the alginate particles is overcome when the surface charge of the alginate is neutralized. To get to the dispersed, coated regime, the chitosan particles must be unable to pack into an agglomerate as they cannot get closer to alginate or chitosan particles than the minimum stable distance of separation. This packing constraint appears to be what breaks apart the agglomerates at high chitosan concentrations.

3.5 Summary

In this study, we were able to determine experimentally the interaction regime boundaries of chitosan nanoparticles and alginate microspheres during heteroaggregation by using optical microscopy. Also, fluorescence spectroscopy has proven to be a viable method for determining the particle interaction regime between alginate and tagged chitosan particles due to the quenching of the fluorescence signal when chitosan is adsorbed on to the surface of an alginate particle. In the dispersed, uncoated regime, there are not many free chitosan particles, which produces a lower observed fluorescence signal. In the agglomerated regime, the higher acquired fluorescence signal, the microscope images, and the comparison to DLVO calculations indicate that there are unadsorbed chitosan particles in each agglomerate. The unadsorbed chitosan leads to the higher observed fluorescence signal. In the dispersed, coated regime, the signal drops near the boundary to the agglomerated regime due to a decrease in the number of unbound chitosan particles. This signal drop on either side of the agglomerated regime is what can be used to determine the transition in regimes. The fluorescence detection method is limited by alginate particle scattering and also the inner filter effect if the concentration of fluorescent particles is too high. With this knowledge we were able to determine a threshold value for the interaction regime change from agglomerated to dispersed, coated. Finally, simple, approximate theoretical calculations elucidated possible mechanisms for the transitions between interaction regimes. One calculation suggested that the mechanism of agglomeration is simply charge neutralization. In addition, a DLVO calculation suggested that the mechanism of dispersion from

agglomeration is the lack of space to pack more unadsorbed chitosan particles into an agglomerate.

Chapter 4

Determining Particle Interaction Regime

Boundaries using Fluorescence

Spectroscopy at Varying pH

4.1 Introduction

Alginate and chitosan particles are used as delivery vehicles with pH tunable release. As pH is lowered they release their payloads (Agnihotri et al., 2004, Tønnesen and Karlsen, 2002). Therefore it is important to understand their interaction behavior as pH is lowered. Since the zeta potential shifts with pH, it is therefore expected that interaction boundaries should shift as well. Determining the interaction regime boundaries can establish requirements for the concentration ratio of chitosan to alginate in order to maintain particle stability as pH is lowered.

This study aims to test the interaction of chitosan and alginate as pH is lowered by both using a buffer and by simply adding acid. Alginate concentration is kept constant while chitosan concentration varies. The particle interaction is determined with both the fluorescence spectroscopy method developed in Chapter 3 and with an optical microscope. This study tests the viability of fluorescence spectroscopy in a different environment in addition to determining how the interaction regime boundaries shift with pH.

4.2 Experimental Methods

4.2.1 Materials

As in Chapter 3 low molecular weight chitosan (Sigma Aldrich) again was tagged with FITC (Sigma Aldrich) according to the procedure in Huang, et al (2004). The

chitosan was polymerized with TPP (Sigma Aldrich) using the ionic gelation method outlined in Yu, et al (2013). The difference in procedure occurred when a buffer was used to control pH in each sample. Instead of resuspending the resulting chitosan pellet in water, the pellet was resuspended in the buffer. The concentration of the chitosan was kept at 37.5 mg/mL of water but when the buffer was used the concentration was 37.5 mg/mL of buffer. A glycine/hydrochloric acid and acetic acid/sodium acetate buffer were used to control pH. Other buffers were tried but they seemed to react with the chitosan and alginate particles. Zeta potential at each pH was measured using a Malvern Zetasizer. The pH was changed by adding 0.2 M HCl to each batch of chitosan tested until the desired pH was reached. The buffers used are listed in Table 4.1.

pH	Chitosan Zeta Potential	0.2 M Glycine	0.2 M HCl	0.2 M Acetic Acid	0.2 Sodium Acetate
2.2	51.0 mV	50 mL	44 mL		
2.8	48.2 mV	50 mL	11.4 mL		
3.5	44.3 mV	50 mL	5 mL		
4.0	41.3 mV			41 mL	9 mL
4.8	39.3 mV			20 mL	30 mL
5.6	30.6 mV			4.8 mL	45.2 mL

Table 4.1. Buffers used to control pH.

Also as in Chapter 3, the alginate particles were also prepared in the same way as in Yu, et al (2013). A sodium alginate (Acros Organics) and sucrose solution was emulsified in 1,6-dibromohexane (Acros Organics) and iso-octane (Fisher Scientific) with span-80 (sigma Aldrich) as the surfactant. The emulsified alginate was crosslinked with calcium chloride purchased from Fisher Scientific to create calcium alginate beads.

The resulting beads were wet sieved down to below 38 μm and then filtered to be above 25 μm with an average size of 34 μm (measured with Beckman Coulter LS 13 320).

4.2.2 Experimental Procedure

When a buffer was not used, the pH of each sample was controlled by adding enough amounts of 0.2 M HCl to change the pH to the desired level while monitoring the pH with a pH meter. For each sample 3.2 mL of water was measured out first. Then, alginate was added and sonicated. Then, the relevant level of chitosan was added. After that, 0.2 M HCl was added to each sample until the desired pH was reached. For these samples the pH levels tested were 2.3, 3.6, and 4.8. Higher pH values were not tried because the chitosan particles react with sodium hydroxide and the pH of the samples in plain water was very variable in a range from 5-6.8. Deionized water was added to each sample until an 8 mL sample volume was reached. Due to the variable amount of HCl added this also varied from sample to sample and even trial to trial. The samples were then stirred with microstirbars for an hour before being tested in the Horiba Jobin Yvon fluorescence spectrometer. Each sample was pulsed with light at a wavelength of 490 nm and the emission data was collected as a spectrum from 500-650 nm. The samples were also photographed using the Zeiss Axio Lab.A.1 microscope at 50x magnification. Three trials were also conducted for each of these samples.

For the buffer controlled pH experiments, the buffer suspended chitosan and weighed out alginate particles were mixed into the buffer used for the experiment. These samples were prepared similarly to the pure water experiments. First, the buffer volume

was measured out, which varied according to how much chitosan was added. Then, 0.1 g (4.63×10^6 particles) of alginate was added to the buffer measured out. The approximated volume fraction of alginate in each sample is 0.012. The particles were weighed out using the centrifugation method to remove the particles from water storage. The sample with alginate was then sonicated as in the no buffer samples. Then the chitosan in buffer suspension was added at the proper level and then that was sonicated again. Samples were then left to stir with micro-stirbars for an hour to cool down. Then these samples were tested in the Horiba Jobin Yvon fluorescence spectrometer. The Ocean Optics fluorescence spectrometer was not used. The Zeiss Axio Lab.A.1 microscope at 50x magnification was used to photograph the samples. Three trials of each sample were tested. The chitosan was added according to the levels in Table 4.2.

Sample	Chitosan Buffer Suspension Volume	Number of Chitosan Particles	Chitosan Volume Fraction	Buffer Volume
1	6.25 μL	3.06×10^{10}	3.13×10^{-5}	7.99375 mL
2	12.5 μL	6.11×10^{10}	6.25×10^{-5}	7.9875 mL
3	25 μL	1.22×10^{11}	1.25×10^{-4}	7.975 mL
4	50 μL	2.44×10^{11}	2.50×10^{-4}	7.95 mL
5	100 μL	4.89×10^{11}	5.00×10^{-4}	7.9 mL
6	200 μL	9.78×10^{11}	1.00×10^{-3}	7.8 mL
7	400 μL	1.96×10^{12}	2.00×10^{-3}	7.6 mL
8	800 μL	3.91×10^{12}	4.00×10^{-3}	7.2 mL
9	1600 μL	7.82×10^{12}	8.00×10^{-3}	6.4 mL
10	3200 μL	1.56×10^{13}	1.60×10^{-2}	4.8 mL

Table 4.2. Levels of chitosan for each sample and corresponding buffer volumes

4.3 Results and Discussion

4.3.1 Fluorescence Spectroscopy Results without Buffers

For each spectrum generated for samples without a buffer, an integral from maximum intensity to half maximum intensity was taken using the trapezoidal rule (Figure 4.1).

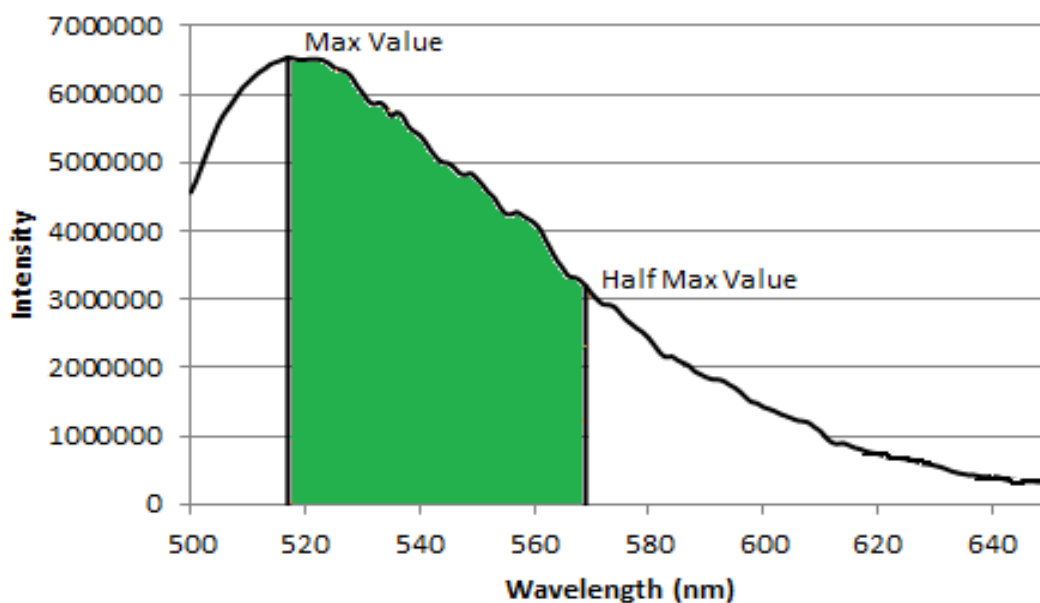


Figure 4.1. Illustration of the integral from the maximum intensity to the half maximum intensity.

These numbers were averaged over three trials for each pH and chitosan level. Then these values were plotted against the number of chitosan particles (Figure 4.2a) and were also normalized over the maximum value at each pH of the range of the chitosan particle levels (Figure 4.2b).

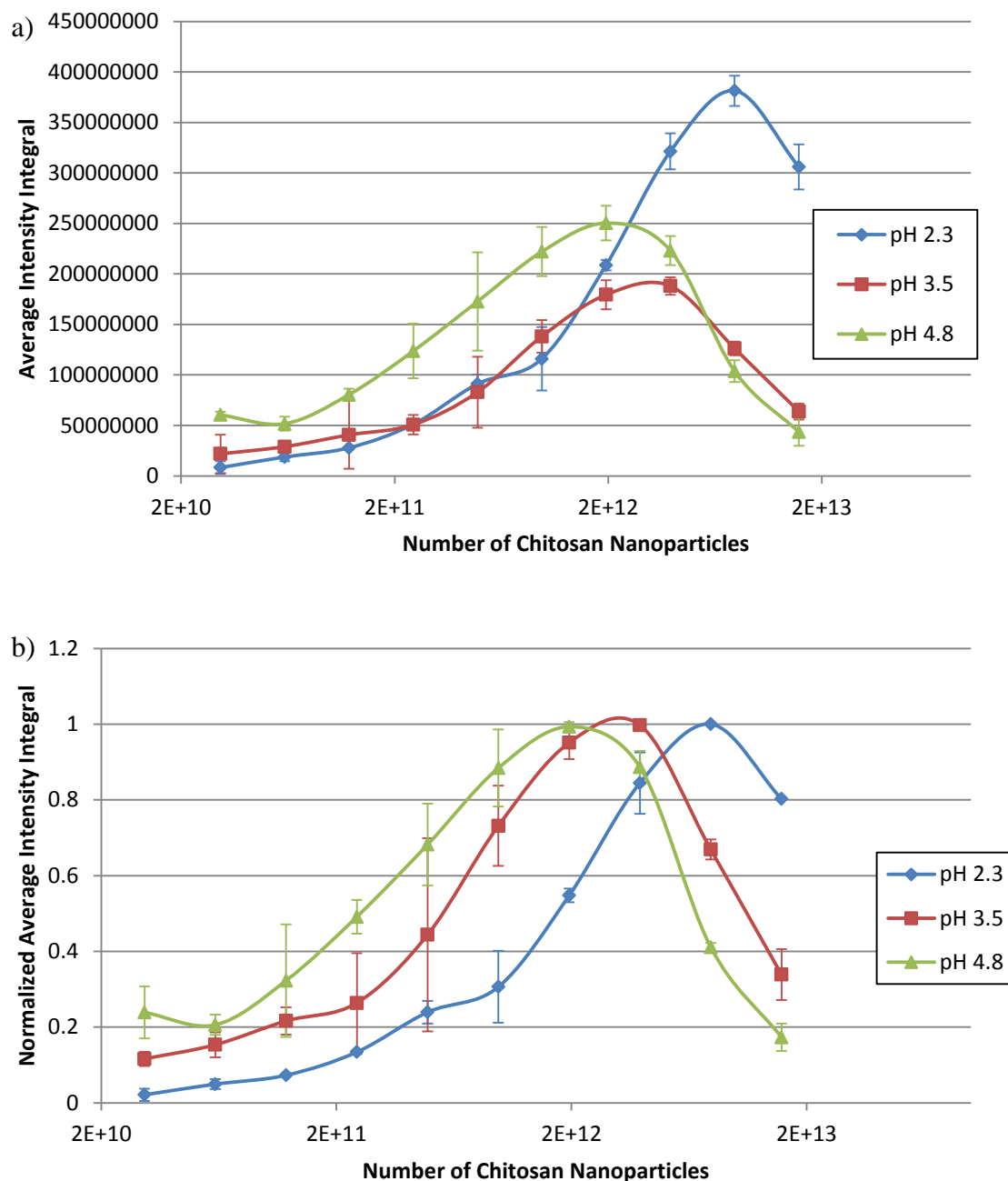


Figure 4.2. (a) Average intensity integral from maximum intensity to half maximum intensity for each pH plotted against number of chitosan particles at an alginate level of 4.63×10^6 (0.1 g) particles. (b) Normalized average intensity integral from maximum intensity to half maximum intensity for each pH plotted against number of chitosan particles at an alginate level of 4.63×10^6 (0.1 g) particles.

Then, as with the buffer experiments, the slope of the normalized average intensity integral versus the number of chitosan particles was calculated and then plotted to see where the -0.4 slope boundary was crossed to mark where the interaction regime transition from agglomerated to dispersed, coated occurred according to the fluorescence spectroscopy results (Figure 4.3).

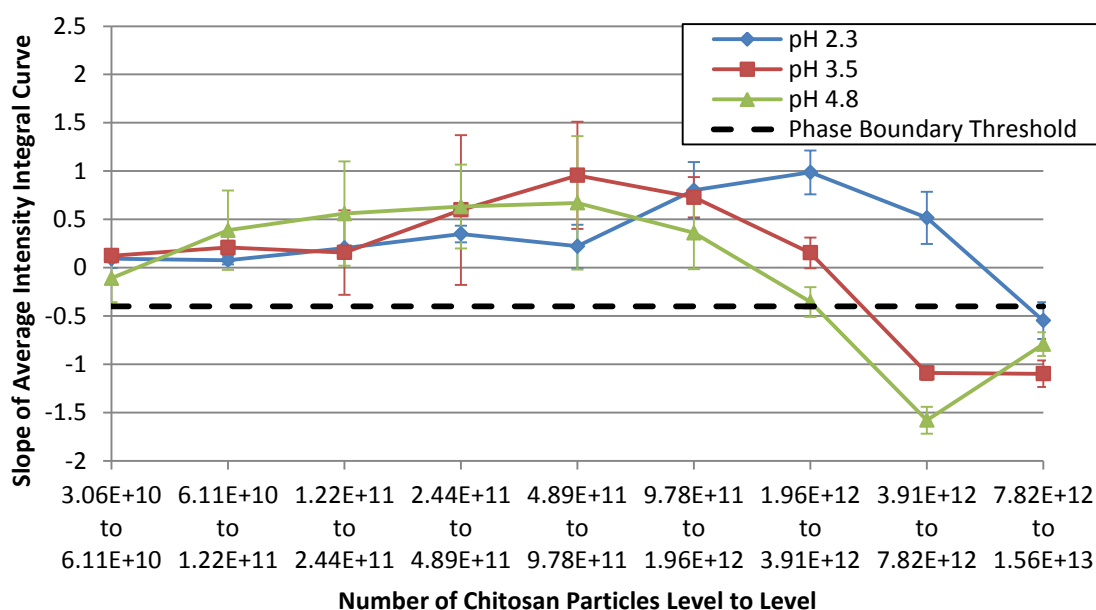


Figure 4.3. Slope of the normalized average intensity integral from maximum intensity to half maximum intensity curve from each chitosan level to level for each pH without a buffer.

These results indicated that there is interaction regime transition at the pH of 2.3 from 7.82×10^{12} ($1600 \mu\text{L}$) to 1.56×10^{13} ($3200 \mu\text{L}$) chitosan particles but there an error high enough where that may not be an interaction regime transition. At the pH of 3.5 and 4.8 there is an interaction regime transition from 3.91×10^{12} ($800 \mu\text{L}$) to 7.82×10^{12} ($1600 \mu\text{L}$) chitosan particles. At the pH of 4.8 there may be a regime transition from 1.96×10^{12}

(400 μL) to 3.91×10^{12} (800 μL) chitosan particles instead but because of experimental uncertainty, that is not perfectly clear.

We again wanted to compare these results to microscope results. For pH 2.3, large agglomerates are seen in the 9.78×10^{11} (200 μL) chitosan particles microscope picture (Figure 4.4).

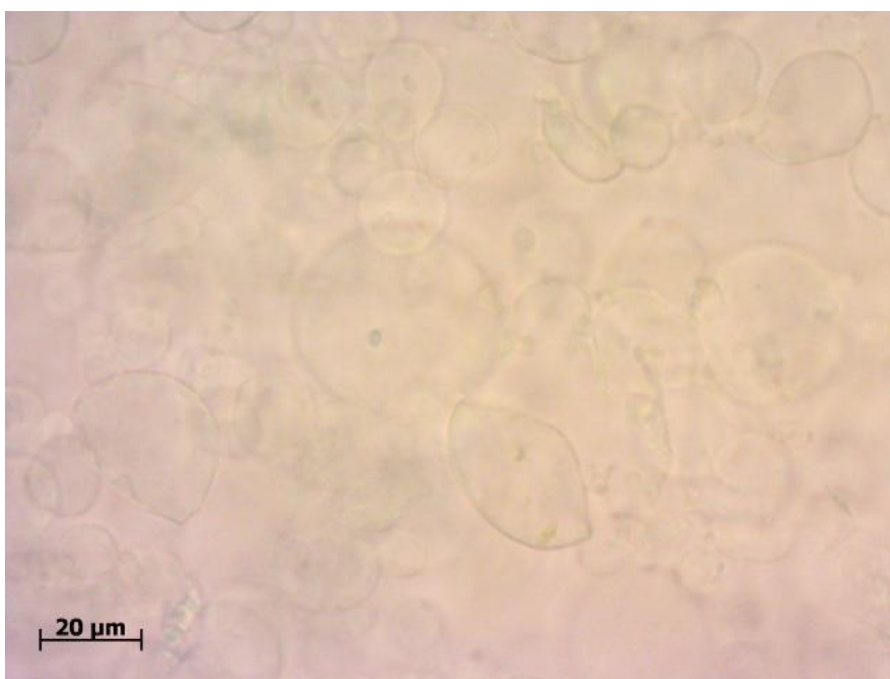


Figure 4.4. Microscope image of 4.63×10^6 (0.1 g) alginate particles and 9.78×10^{11} (200 μL) chitosan particles at pH 2.3

Interestingly, small agglomerates continue on through 1.56×10^{13} (3200 μL) chitosan particles (Figure 4.5).

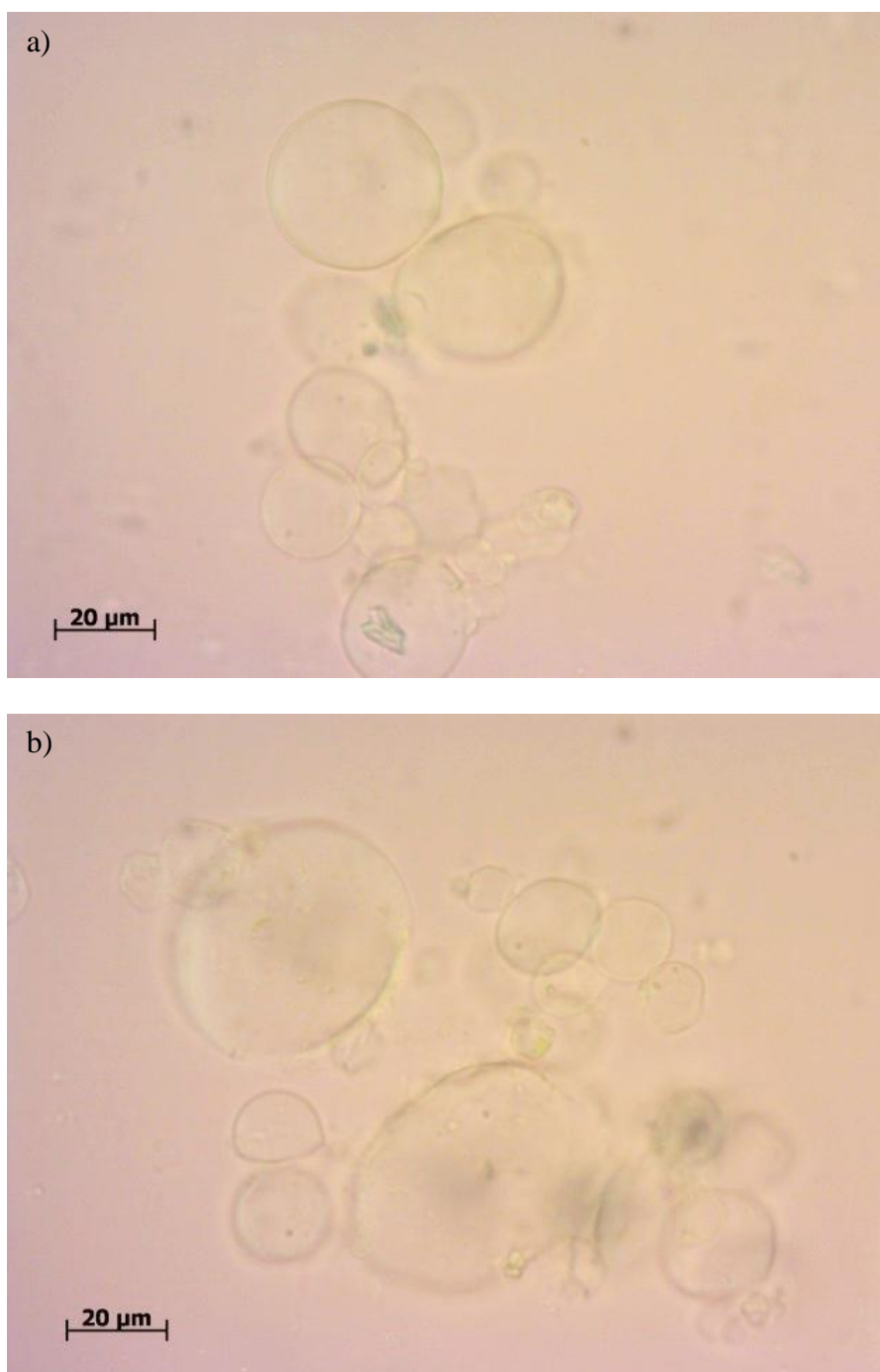
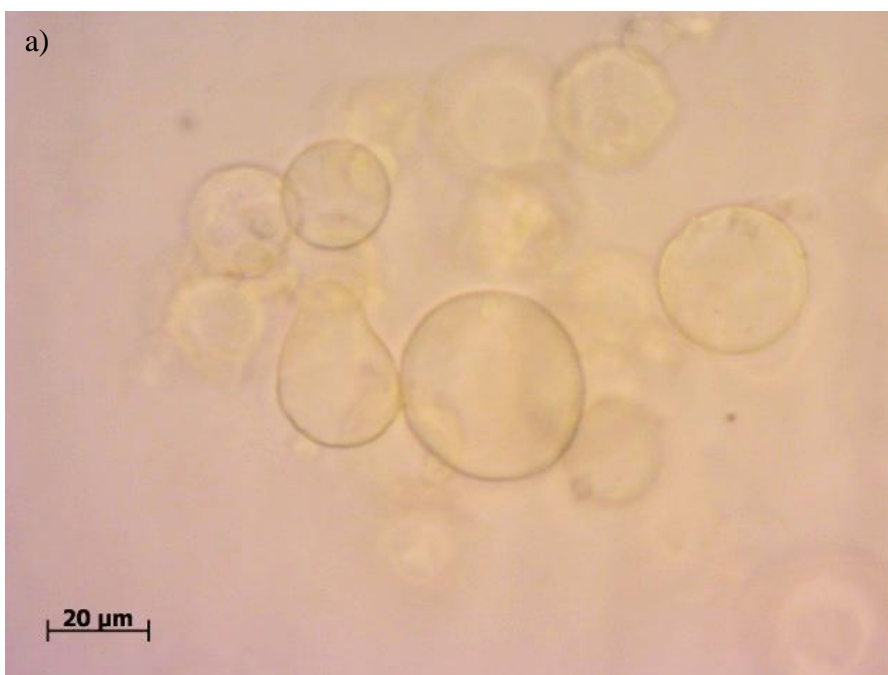


Figure 4.5. Microscope images of 4.63×10^6 (0.1 g) alginate particles and (a) 3.91×10^{12} (800 μL) and (b) 1.56×10^{13} (3200 μL) chitosan particles at a pH of 2.3. The samples are in the agglomerated regime.

Since the interaction regime transition was within the error, this fits the fluorescence spectrometer results where no clear regime boundary exists.

Next, microscope pictures of the pH 3.5 were taken. Alginate particles are clearly agglomerated at 3.91×10^{12} (800 μL) chitosan particles but then disperse at 7.82×10^{12} (1600 μL) chitosan particles (Figure 4.6).



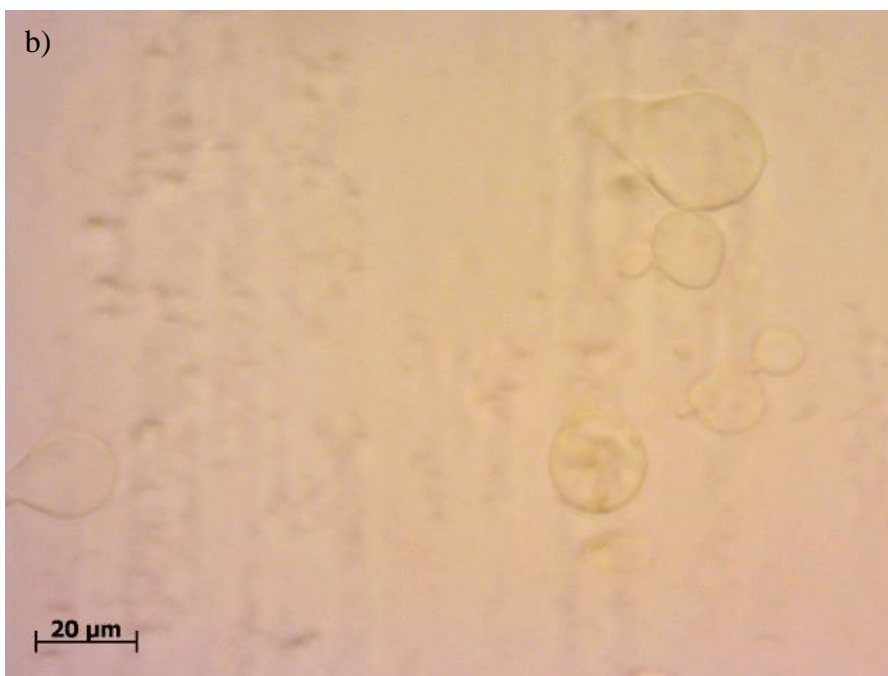


Figure 4.6. Microscope images of 4.63×10^6 (0.1 g) alginate particles and (a) 3.91×10^{12} (800 μL) and (b) 7.82×10^{12} (1600 μL) chitosan particles at a pH of 3.5. This is the agglomerated/dispersed, coated regime.

The agglomerated/dispersed, coated interaction regime boundary is defined in between these levels. Again, the fluorescence spectrometer results are corroborated by the microscope pictures.

Finally, microscope pictures of the pH 4.8 were taken. The alginate particles are clearly agglomerated at a chitosan level of 1.96×10^{12} (400 μL) particles but may or may not be in small agglomerates at 3.91×10^{12} (800 μL) chitosan particles (Figure 4.7).

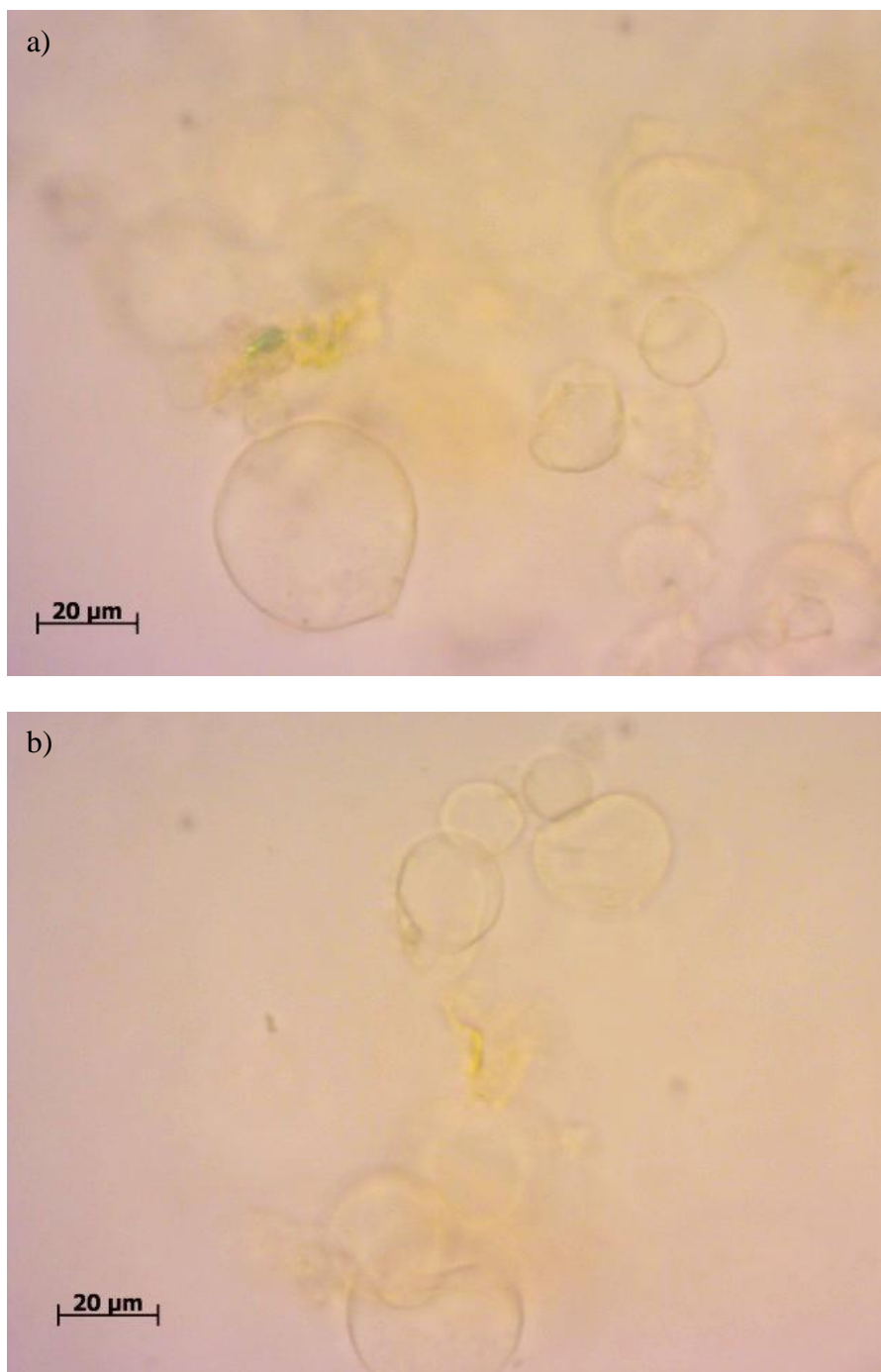


Figure 4.7. Microscope images of 4.63×10^6 (0.1 g) alginate particles and (a) 1.96×10^{12} (400 μL) chitosan particles and (b) 3.91×10^{12} (800 μL) at a pH of 4.8. This is the potential agglomerated/dispersed, coated interaction regime boundary.

The alginate particles are definitely dispersed at the chitosan level of 7.82×10^{12} (1600 μL) particles (Figure 4.8).

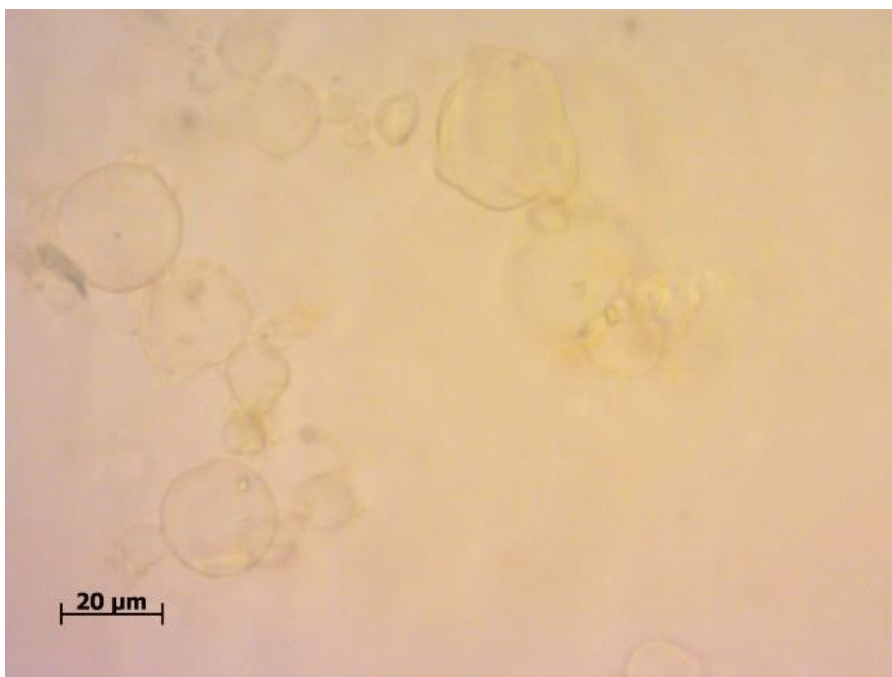


Figure 4.8. Microscope image of 4.63×10^6 (0.1 g) alginate particles and (a) 7.82×10^{12} (1600 μL) chitosan particles. The sample is in the dispersed interaction regime

The uncertainty of the exact location of the interaction regime boundary as seen by the fluorescence spectroscopy results is displayed in the microscope pictures. The interaction regime boundary could be in between 1.96×10^{12} (400 μL) and 3.91×10^{12} (800 μL) chitosan particles or it could be between 3.91×10^{12} (800 μL) and 7.82×10^{12} (1600 μL) chitosan particles. The fluorescence spectroscopy results once again are proven out the microscope pictures.

The trend seems to be that at a lower a pH more particles are needed to disperse the alginate particles. This is probably due to the fact that alginate should be at a near

neutral zeta potential at a low pH being that it is fairly negatively charged at a higher pH. Since the chitosan molecules will not be as attracted to a neutral particle, they are less likely to coat alginate particles and it is harder for the alginate particles to then disperse.

4.3.2 Fluorescence Spectroscopy Results with Buffers

For the each of the generated buffer spectrums, an integral using the trapezoidal rule was taken from the maximum intensity value to the half maximum intensity value. These values were then averaged over three trials per level for pH. These averages were then plotted against the number of chitosan particles to compare how each pH affects the fluorescent intensity when chitosan level is changed (**Error! Reference source not found.a**). Also, these values were normalized against the highest average intensity integral for each pH and also plotted against the number of chitosan particles (**Error! Reference source not found.b**).

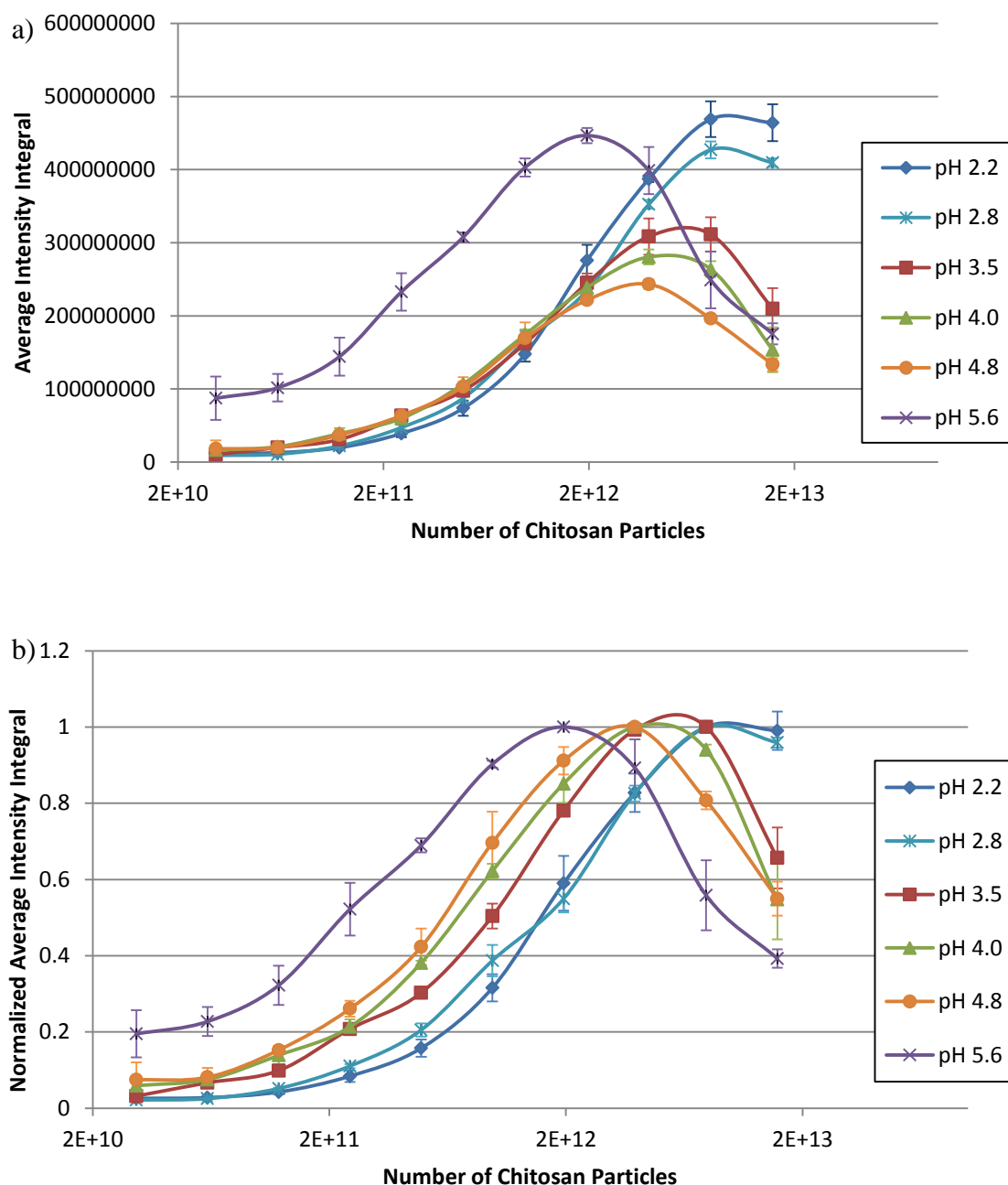


Figure 4.9. (a) Average intensity integral from maximum intensity to half maximum intensity for each pH plotted against number of chitosan particles at an alginate level of 4.63×10^6 (0.1 g) particles. (b) Normalized average intensity integral from maximum intensity to half maximum intensity for each pH plotted against number of chitosan particles at an alginate level of 4.63×10^6 (0.1 g) particles.

Then, the slope of the normalized average intensity integral versus the number of chitosan particles was calculated and then plotted to see where the -0.4 slope boundary was crossed to mark where the interaction regime transition from agglomerated to dispersed, coated occurred according to the fluorescence spectroscopy results (Figure 4.10)

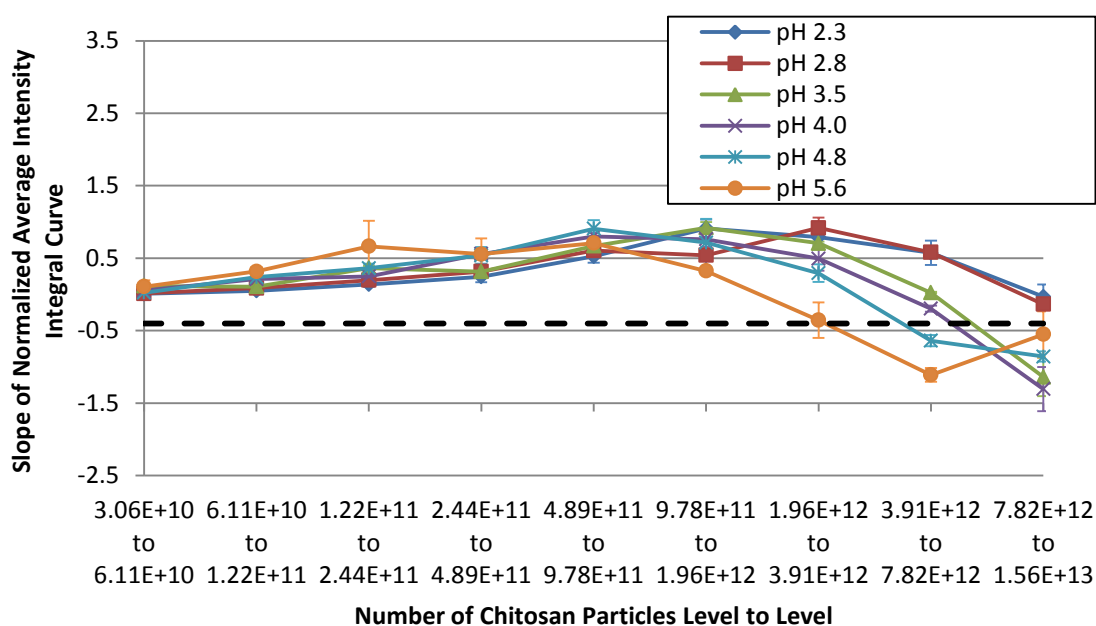
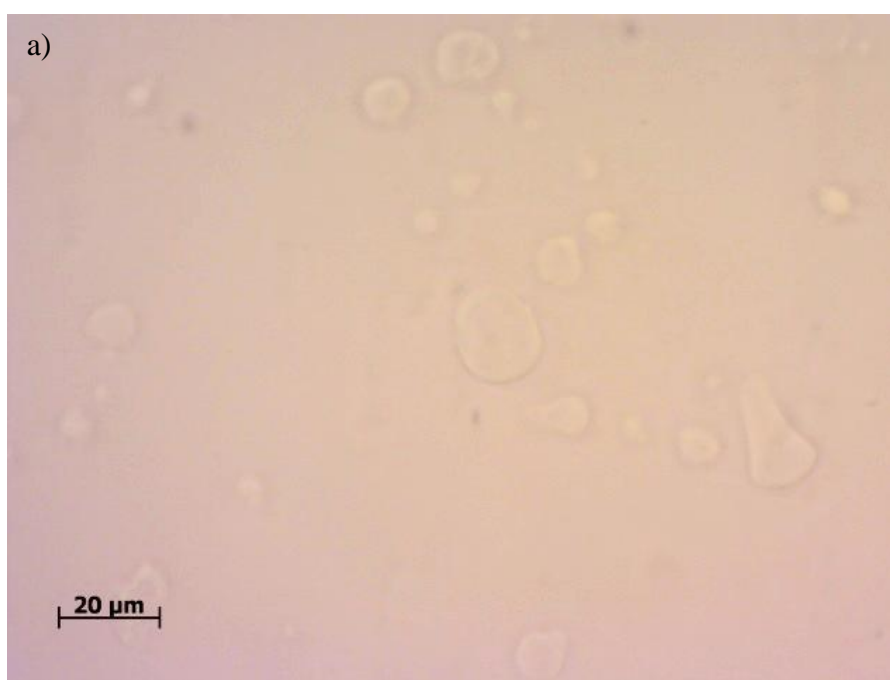


Figure 4.10. Slope of the normalized average intensity integral from maximum intensity to half maximum intensity curve from each chitosan level to level for each pH with a buffer.

From these results it looks like there is no interaction regime transition from agglomerated to dispersed, coated for a pH of 2.2 and 2.8. At a pH of 3.5 and 4.0 the -0.4 slope occurs from 7.82×10^{12} (1600 μL) to 1.56×10^{13} (3200 μL) chitosan particles. Finally at a pH of 4.8 and 5.6 the -0.4 slope occurs from 3.91×10^{12} (800 μL) to 7.82×10^{12}

(1600 μL) chitosan particles although due to error the interaction regime boundary for pH of 5.6 could be in between 1.96×10^{12} (400 μL) and 3.91×10^{12} (800 μL) chitosan particles.

We wanted to compare these results to microscope picture to make sure that we were seeing the interaction regime transition with microscope results. At a pH of 2.2 there was no visible interaction regime transition at all, even one from dispersed, uncoated to agglomerated (Figure 4.11).



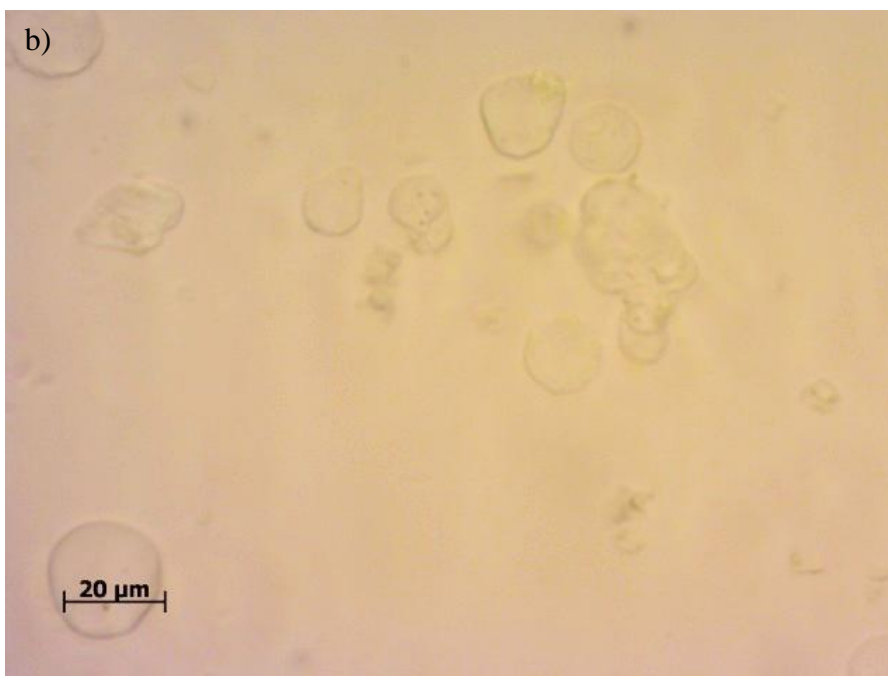


Figure 4.11. Microscope images of 4.63×10^6 (0.1 g) alginate particles and (a) 3.91×10^{12} (800 μL) and (b) 1.56×10^{13} (3200 μL) chitosan particles in a pH 2.2 0.2 M glycine/0.2 M HCl buffer.

Here it seems that the spectroscopy results corroborate the pictures. There is a red flag, however with the fact that the alginate particles are far smaller than their original size.

Next, pictures were taken for samples at a pH of 2.8. There is a clear indication of the agglomerated regime at a chitosan level of 3.91×10^{12} (800 μL) particles (Figure 4.12).

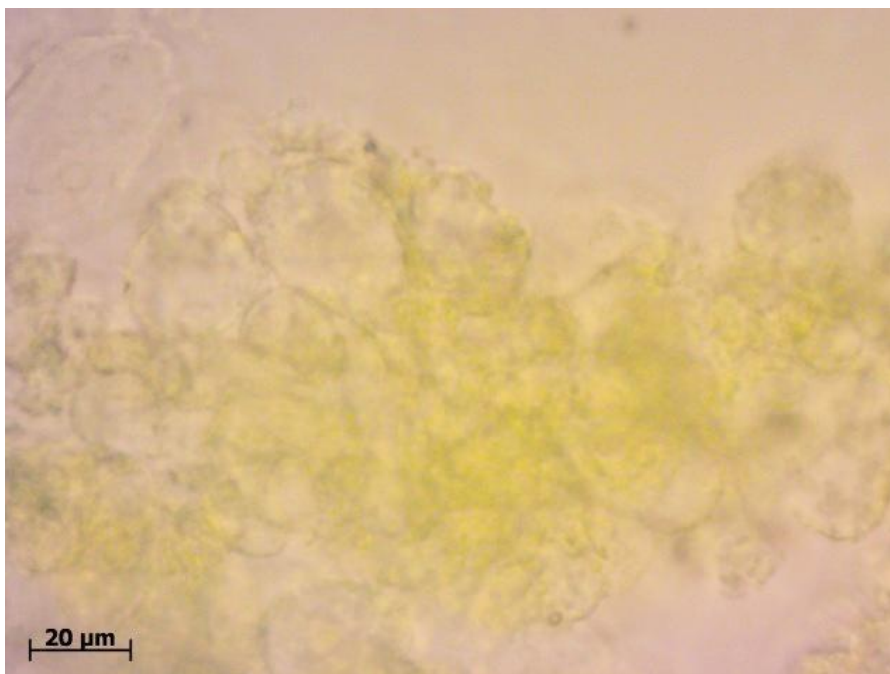


Figure 4.12. Microscope image of 4.63×10^6 (0.1 g) alginate particles and 3.91×10^{12} (800 μL) chitosan particles in pH 2.8 0.2 M glycine/0.2 M HCl buffer.

According to the spectrometer results since there is an agglomerated regime, there should not be an interaction regime transition to dispersed, coated but that is not the case. There is a regime transition from 7.82×10^{12} (1600 μL) to 1.56×10^{13} (3200 μL) chitosan particles (Figure 4.13).

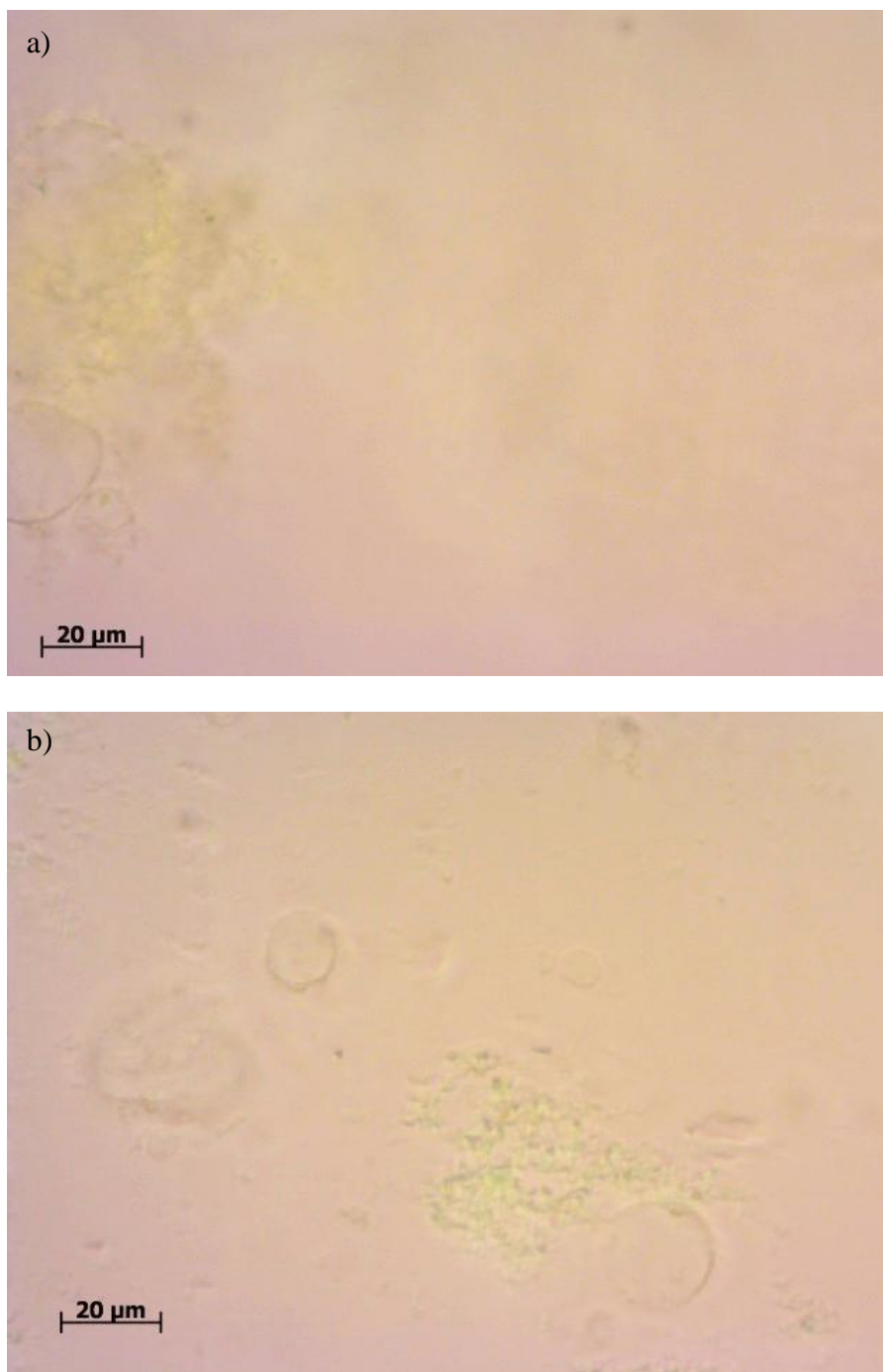
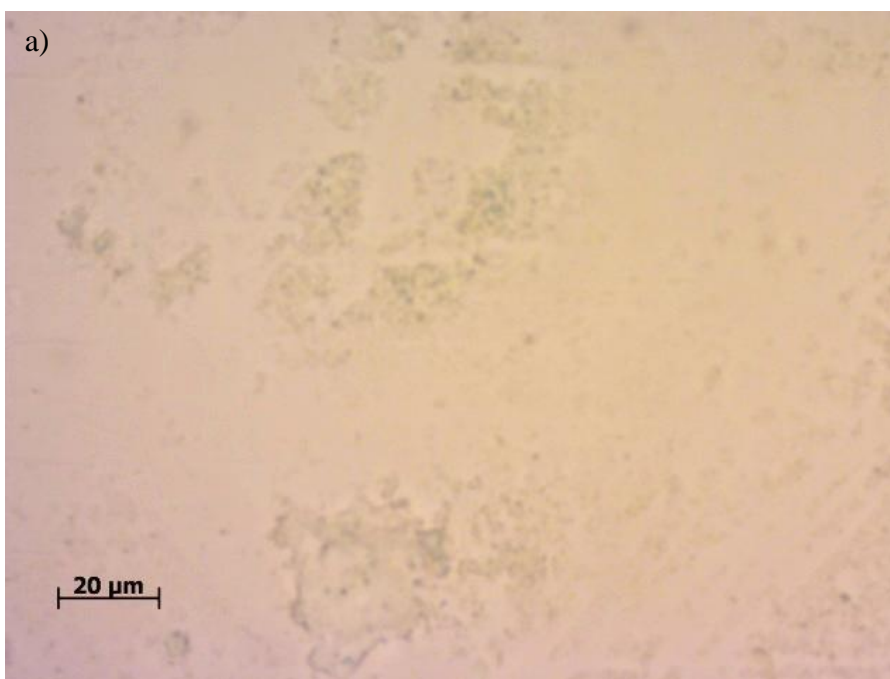


Figure 4.13. Microscope images of 4.63×10^6 (0.1 g) alginate particles and (a) 7.82×10^{12} (1600 μL) and (b) 1.56×10^{13} (3200 μL) chitosan particles in a pH 2.8 0.2 M glycine/0.2 M HCl buffer. This marks an interaction regime transition from agglomerated to dispersed, coated.

While not true in Figure 4.12, the alginate particles in Figure 4.13 again appear to have either shrunk or may have even broken apart. There might be chitosan particles that have reacted together to form larger “nets” as it appears in Figure 4.13b.

At a pH of 3.5 the microscope results look even less like the no buffer results. Some of the alginate particles no longer have a spherical shape Figure 4.14a) and there seem to be chitosan aggregates without very many alginate particles (Figure 4.14b).



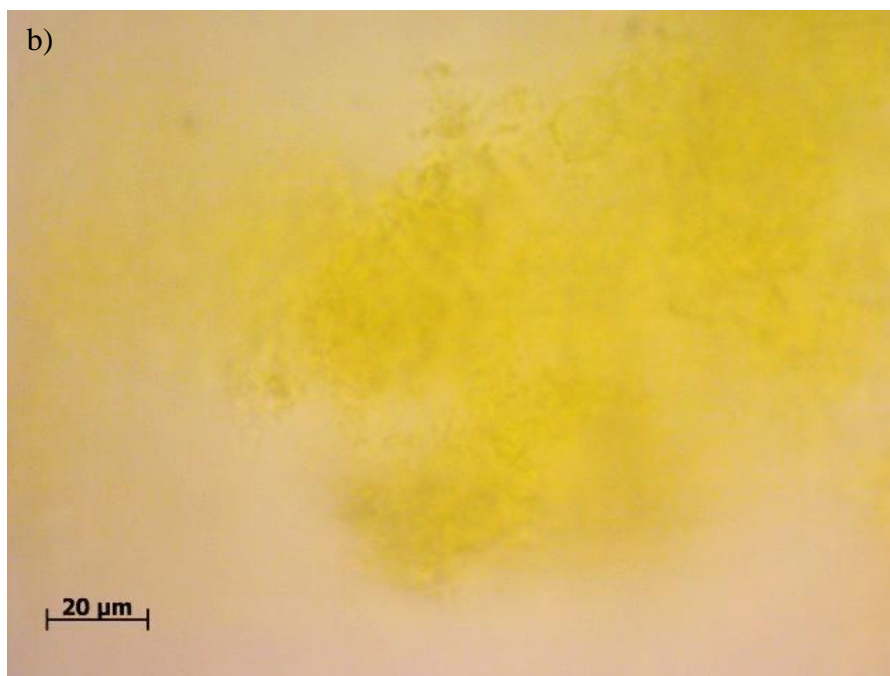


Figure 4.14. Microscope images of 4.63×10^6 (0.1 g) alginate particles and (a) 3.91×10^{12} (800 μL) and (b) 1.56×10^{13} (3200 μL) chitosan particles in a pH 3.5 0.2 M glycine/0.2 M HCl buffer.

When switching to the sodium acetate and acetic acid buffer, alginate particles are not visible at all in the microscope picture which makes it impossible to see what is going on in each sample (Figure 4.15).

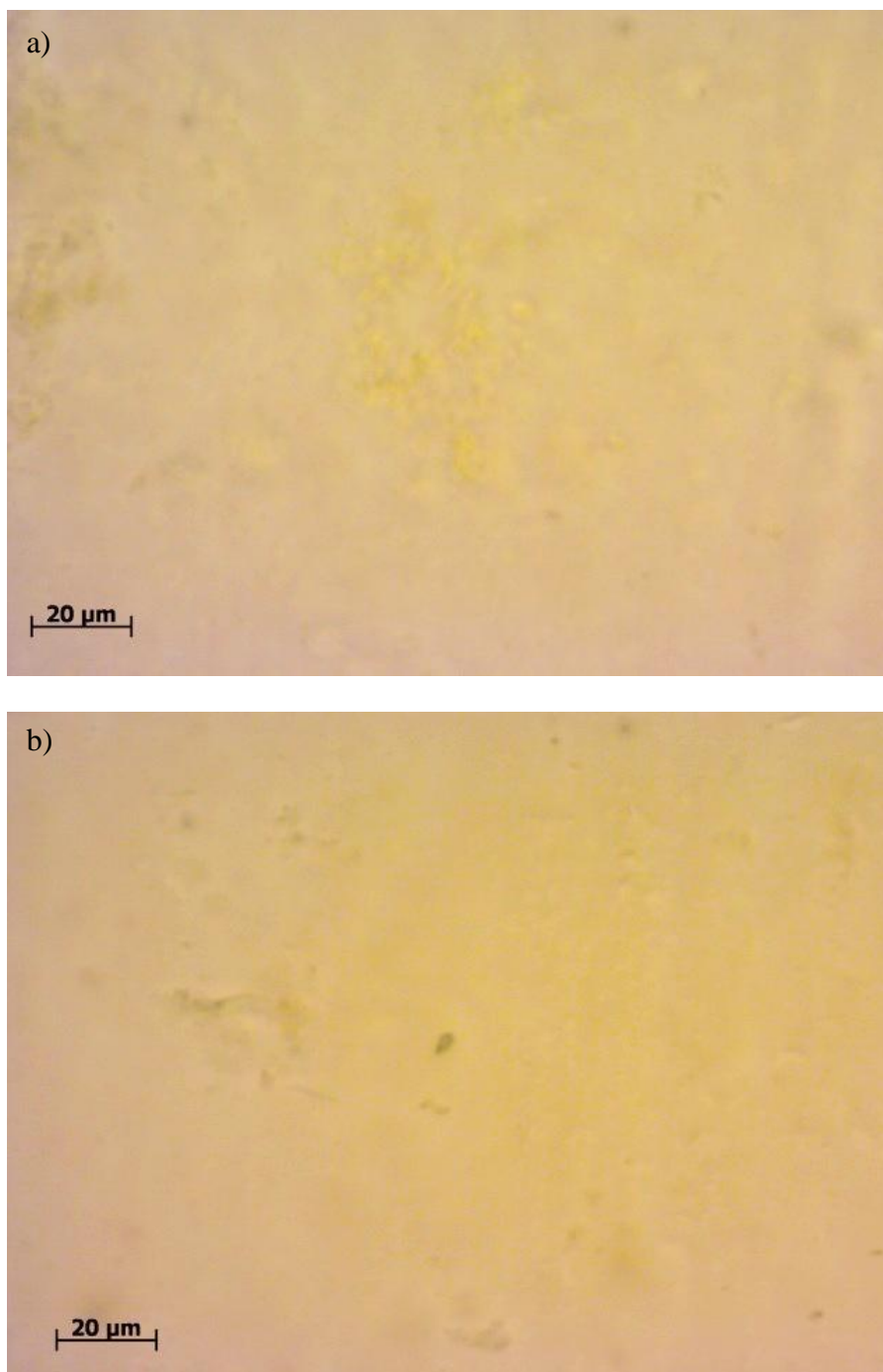


Figure 4.15. Microscope images of 4.63×10^6 (0.1 g) alginate particles and 7.82×10^{12} (1600 μL) chitosan particles in (a) pH 4.8 and (b) pH 5.6 0.2 M acetic acid/0.2 M sodium acetate buffer.

There is either refractive index matching to make the alginate particles invisible or the alginate particles' cross-linking got broken in the buffer. If it is the former, the fluorescence spectrometer results have a chance of being accurate while if it is the latter there is no chance of the spectrometer results being accurate.

The buffer studies show a clear limitation of the fluorescence spectrometer application in the alginate chitosan system. When the primary particles change size, composition, or optical properties from sample to sample the predicted interaction regime transition is not accurate.

4.4 Summary

When pH was manipulated with only 0.2 M HCl the microscope results matched the fluorescence spectroscopy results due to the fact that the primary particles were not changed in any way. The pH indicator property of FITC did not affect the efficacy of fluorescence spectroscopy. Using microscopic and fluorescence spectroscopy techniques together, it was proven that as pH is lowered it is more difficult for alginate particles to shift from the agglomerated regime to the dispersed, coated regime. When the primary particles are no longer the same chemically or optically as they were in pure water, it was proven that the fluorescence spectroscopy method for determining the agglomerated/dispersed, coated regime boundary was a failure. From microscope results it appears that the chitosan and maybe even the alginate undergoes some sort of reaction to a buffer with 0.2 M glycine. 0.2 HCl does not affect the particles. When placed in a 0.2 M sodium acetate and 0.2 M acetic acid buffer the alginate particles were not visible.

It was impossible to tell whether the alginate particles were refractive index matched to the fluid or whether they were actually broken down.

Chapter 5

Conclusions and Future Work

5.1 Conclusions

This work has covered noncolloidal suspension flow and colloidal hydrogel particle interactions. Techniques from particle video imaging to fluorescence spectroscopy were applied to the systems studied. This investigation was done with the goal of developing a basic understanding of observed phenomena in order to better create nanoparticle coated microparticles.

First, a noncolloidal suspension of PMMA particles was studied under moderate oscillatory shear using particle video imaging. It was found that outward particle drift occurred during the course of the applied shear. The velocity of the drift was approximately linearly dependent on strain. There was also a frequency dependence that approximately followed an inverse square relation. Torque measurements collected simultaneously with the particle video imaging showed an increase as strain increased except at intermediate strains as was common with other oscillatory flow experiments. The torque measurements with the drift velocity results suggest competing mechanisms where there is competition between radial shear-induced migration driven by the particle stress balance and a microstructural ordering mechanism driven by local inertial effects layering the particles.

Next, a fluorescence spectroscopy application was created to study a colloidal hydrogel system of negatively charged alginate microparticles and positively charged fluorescently-tagged chitosan nanoparticles. The interaction regime boundaries between dispersed, uncoated and agglomerated and between agglomerated and dispersed, coated were determined by optical microscopy. Then, fluorescence spectroscopy was used to

determine if the interaction regime boundaries could be seen in the variations of the intensity readings. It was found that the dispersed, uncoated and agglomerated regime boundary was not detected when varying chitosan. The agglomerated and dispersed, coated regime boundary was marked in the fluorescence spectroscopy results by a decrease in the slope of the normalized integral from maximum intensity to half maximum intensity plotted against the number of chitosan particles. There was a limitation found due to the inner filter effect as higher chitosan levels yield a lower overall fluorescence signal intensity. DLVO calculations were used in conjunction with the microscope images and the fluorescence results to determine the mechanism behind the interaction regimes. It was found that a surface charge reversal likely caused the transition from the dispersed, uncoated to agglomerated regime. It was found that a limit on the maximum number of unbound chitosan particles that could be packed within an agglomerate was a potential cause of the transition from the agglomerated to dispersed, coated regime.

Finally, a study was done using fluorescence spectroscopy to study the interaction of the alginate and chitosan particles while varying pH. This work was done to not only study how varying pH affects the interaction of alginate and chitosan but to further test the limits of using fluorescence spectroscopy in order to determine the location of the interaction regime boundary. The fluorescence spectroscopy results were then compared to microscope images. It was found when using a buffer to control pH that the particles were reacting with the salts in the buffer, resulting in a change to the primary particle properties. When the reaction happened, the expected results did not match the spectroscopic results. When HCl, which does not react with the primary particles, was

used to manipulate the pH of each individual sample, the fluorescence spectroscopy method accurately predicted the interaction regime transitions again.

5.2 Future Work

Where this work leaves off is at the further exploration of the use of fluorescence spectroscopy to understand more complex particle interaction. Alginate and chitosan were the only particles studied using fluorescence spectroscopy. It would be interesting to explore how a change in primary particle affects the particle interaction and the effectiveness of fluorescence spectroscopy to determine that particle interaction.

Since alginate and chitosan are encapsulating agents, it would be interesting to see how a payload would affect the spectral results. The effectiveness of a multiscale alginate and chitosan particle as a delivery agent could also be further explored. It could be seen whether fluorescence spectroscopy would work when there is a potentially interfering payload.

There was also room left to study how to better optimize the creation of nanoparticle coated microparticles. Shear flow was not explored as an avenue for optimization. One can concurrently study the particle interaction under shear flow with fluorescence spectroscopy.

Another idea is to test interaction regime transitions with fluorescence spectroscopy when switching out the chitosan nanoparticles with some other fluorescently tagged nanoparticles that have a higher van der Waals attraction than electrostatic repulsion. Since quenching due to adsorption seems to be the primary

mechanism for the downshift in intensity during a regime transition it would seem that self-attracting particles would prevent fluorescence spectroscopy from working to show regime transitions.

Finally, another idea would be study the effectiveness of other fluorophores. FITC is a toxic molecule and cannot be used for oral delivery applications. It would be beneficial to study non-toxic fluorophores and see if they can be applied to find the regime boundaries.

References

- Abbott, J. R., Tetlow, N., Graham, A. L., Altobelli, S. A., Fukushima, E., Mondy, L. A. & Stephens, T. S. 1991. Experimental observations of particle migration in concentrated suspension - couette flow. *Journal of Rheology*, 35, 773-795.
- Agnihotri, S. A., Mallikarjuna, N. N. & Aminabhavi, T. M. 2004. Recent advances on chitosan-based micro-and nanoparticles in drug delivery. *Journal of Controlled Release*, 100, 5-28.
- Albani, J. R. 2008. *Principles and applications of fluorescence spectroscopy*, Wiley.com.
- Altobelli, S. A., Fukushima, E. & Mondy, L. A. 1997. Nuclear magnetic resonance imaging of particle migration in suspensions undergoing extrusion. *Journal of Rheology*, 41, 1105-1115.
- Bailey, B. C. & Yoda, M. 2003. An aqueous low-viscosity density- and refractive index-matched suspension system. *Experiments in Fluids*, 35, 1-3.
- Banerjee, T., Mitra, S., Kumar Singh, A., Kumar Sharma, R. & Maitra, A. 2002. Preparation, characterization and biodistribution of ultrafine chitosan nanoparticles. *International journal of pharmaceutics*, 243, 93-105.
- Barr, S. A. & Luijten, E. 2006. Effective interactions in mixtures of silica microspheres and polystyrene nanoparticles. *Langmuir*, 22, 7152-7155.
- Bell, G. M. & Peterson, G. C. 1972. Calculation of the electric double-layer force between unlike spheres. *Journal of Colloid and Interface Science*, 41, 542-566.
- Berthold, A., Cremer, K. & Kreuter, J. 1996. Influence of crosslinking on the acid stability and physicochemical properties of chitosan microspheres. *STP pharmaceutical sciences*, 6, 358-364.
- Breedveld, V., Van Den Ende, D., Jongschaap, R. & Mellema, J. 2001. Shear-induced diffusion and rheology of noncolloidal suspensions: Time scales and particle displacements. *Journal of Chemical Physics*, 114, 5923-5936.
- Breedveld, V., Van Den Ende, D., Tripathi, A. & Acrivos, A. 1998. The measurement of the shear-induced particle and fluid tracer diffusivities in concentrated suspensions by a novel method. *Journal of Fluid Mechanics*, 375, 297-318.
- Bricker, J. M. & Butler, J. E. 2006. Oscillatory shear of suspensions of noncolloidal particles. *Journal of Rheology*, 50, 711-728.

- Bricker, J. M. & Butler, J. E. 2007. Correlation between stresses and microstructure in concentrated suspensions of non-brownian spheres subject to unsteady shear flows. *Journal of Rheology*, 51, 735-759.
- Butler, J. E., Majors, P. D. & Bonnecaze, R. T. 1999. Observations of shear-induced particle migration for oscillatory flow of a suspension within a tube. *Physics of Fluids*, 11, 2865-2877.
- Chan, A. T. & Lewis, J. A. 2005. Electrostatically tuned interactions in silica microsphere-polystyrene nanoparticle mixtures. *Langmuir*, 21, 8576-8579.
- Chan, D. & Powell, R. 1984. Rheology of suspensions of spherical particles in a newtonian and a non-newtonian fluid. *Journal of non-newtonian fluid mechanics*, 15, 165-179.
- Chapman, B. K. 1990. *Shear-induced migration phenomena in concentrated suspensions*. University of Notre Dame.
- Chow, A. W., Sinton, S. W., Iwamiya, J. H. & Stephens, T. S. 1994. Shear-induced particle migration in couette and parallel-plate viscometers: Nmr imaging and stress measurements. *Physics of Fluids*, 6, 2561-2576.
- Cooper, W. D., Fearon, P. & Parfitt, G. D. 1973. Heterocoagulation of graphitized carbon blacks in aqueous solutions of sodium dodecyl sulphate. *Journal of the Chemical Society, Faraday Transactions 1: Physical Chemistry in Condensed Phases*, 69.
- Corbett, A. M., Phillips, R. J., Kauten, R. J. & McCarthy, K. L. 1995. Magnetic-resonance-imaging of concentration and velocity profiles of pure fluids and solid suspensions in rotating geometries. *Journal of Rheology*, 39, 907-924.
- Dambies, L., Vincent, T., Domard, A. & Guibal, E. 2001. Preparation of chitosan gel beads by ionotropic molybdate gelation. *Biomacromolecules*, 2, 1198-1205.
- Derjaguin, B. V. 1954. A theory of the heterocoagulation, interaction and adhesion of dissimilar particles in solutions of electrolytes. *Discussions of the Faraday Society*, 18.
- Derjaguin, B. V. & Landau, L. D. 1941. A theory of the stability of strongly charged lyophobic sols and the coalescence of strongly charged particles in electrolytic solution. *Acta Physicochim USSR*, 14, 633-662.
- Deshpande, K. V. & Shapley, N. C. 2010. Particle migration in oscillatory torsional flows of concentrated suspensions. *Journal of Rheology*, 54, 663-686.
- Dinnar, U. 1981. *Cardiovascular fluid dynamics*, CRC Press Boca Raton, FL:.

- Fang, Z. W., Mammoli, A. A., Brady, J. F., Ingber, M. S., Mondy, L. A. & Graham, A. L. 2002. Flow-aligned tensor models for suspension flows. *International Journal of Multiphase Flow*, 28, 137-166.
- Feng, J. & Joseph, D. D. 1996. The motion of solid particles suspended in viscoelastic liquids under torsional shear. *Journal of Fluid Mechanics Digital Archive*, 324, 199-222.
- Furusawa, K. & Anzai, C. 1992. Heterocoagulation behavior of polymer lattices with spherical silica. *Colloids and Surfaces*, 63, 103-111.
- Furusawa, K. & Velev, O. D. 1999. Electrokinetic behavior in synthatic process of composite particles. *Colloids and Surfaces A: Physicochemical and Engineering Aspects*, 159, 359-371.
- Gadala-Maria, F. & Acrivos, A. 1980. Shear-induced structure in a concentrated suspension of solid spheres. *Journal of Rheology*, 24, 799.
- Gibbs, B. F. S. K. I. a. C. N. M. 1999. Encapsulation in the food industry: A review. *International Journal of Food Sciences and Nutrition*, 50, 213-224.
- Gilchrist, J. F., Chan, A. T., Weeks, E. R. & Lewis, J. A. 2005. Phase behavior and 3d structure of strongly attractive microsphere-nanoparticle mixtures. *Langmuir*, 21, 11040-11047.
- Golden, J. F. & West, S. S. 1974. Fluorescence spectroscopic and fading behavior of ehrlich's hyperdiploid mouse ascites tumor cells supravitally stained with acridine orange. *Journal of Histochemistry & Cytochemistry*, 22, 495-505.
- Gondret, P. & Petit, L. 1995. Viscosity of disordered and ordered suspensions of solid spheres-experimental results and models. *COMPTES RENDUS DE L ACADEMIE DES SCIENCES SERIE II FASCICULE B-MECANIQUE PHYSIQUE CHIMIE ASTRONOMIE*, 321, 25-31.
- Gondret, P. & Petit, L. 1996. Viscosity of periodic suspensions. *Physics of Fluids*, 8, 2284.
- Greene, M. R., Hammer, D. A. & Olbricht, W. L. 1994. The effect of hydrodynamic flow-field on colloidal stability. *Journal of Colloid and Interface Science*, 167, 232-246.
- Gregory, J. 1988. Colloid interactions. *Material Science Forum*, 25-26, 125-143.

- Hampton, R., Mammoli, A., Graham, A., Tetlow, N. & Altobelli, S. 1997. Migration of particles undergoing pressure-driven flow in a circular conduit. *Journal of Rheology*, 41, 621.
- Han, M., Kim, C., Kim, M. & Lee, S. 1999. Particle migration in tube flow of suspensions. *Journal of rheology*, 43, 1157.
- Harris, R., Lecumberri, E., Mateos-Aparicio, I., Mengibar, M. & Heras, A. 2011. Chitosan nanoparticles and microspheres for the encapsulation of natural antioxidants extracted from *ilex paraguariensis*. *Carbohydrate Polymers*, 84, 803-806.
- He, P., Davis, S. S. & Illum, L. 1999. Chitosan microspheres prepared by spray drying. *International Journal of Pharmaceutics*, 187, 53-65.
- Hester-Reilly, H. J. & Shapley, N. C. 2007. Imaging contrast effects in alginate microbeads containing trapped emulsion droplets. *Journal of Magnetic Resonance*, 188, 168-175.
- Heymann, L., Peukert, S. & Aksel, N. 2002. Investigation of the solid-liquid transition of highly concentrated suspensions in oscillatory amplitude sweeps. *Journal of Rheology*, 46, 93-112.
- Hill, C. T. 1972. Nearly viscometric flow of viscoelastic fluids in the disk and cylinder system. II: Experimental. *Journal of Rheology*, 16, 213.
- Hogg, R., Healy, T. W. & Fuerstenau, D. W. 1966. Mutual coagulation of colloidal dispersions. *Transactions of the Faraday Society*, 62.
- Huang, M., Khor, E. & Lim, L.-Y. 2004. Uptake and cytotoxicity of chitosan molecules and nanoparticles: Effects of molecular weight and degree of deacetylation. *Pharmaceutical Research*, 21, 344-353.
- Hunter, R. J. 1987. Polymeric stabilization and flocculation. *Foundations of Colloid Science*, 1, 450-493.
- Hunter, R. J. & White, L. R. 1987. *Foundations of colloid science*, Clarendon Press.
- Ichikawa, H. & Fukumori, Y. 2000. A novel positively thermosensitive controlled-release microcapsule with membrane of nano-sized poly (*N*-isopropylacrylamide) gel dispersed in ethylcellulose matrix. *Journal of Controlled Release*, 63, 107-119.
- Ingber, M. S., Graham, A. L., Mondy, L. A. & Fang, Z. 2009. An improved constitutive model for concentrated suspensions accounting for shear-induced particle

- migration rate dependence on particle radius. *International Journal of Multiphase Flow*, 35, 270-276.
- Islam, A. M., Chowdhry, B. Z. & Snowden, M. J. 1995. Heteroaggregation in colloidal dispersions. *Advances in Colloid and Interface Science*, 62, 109-136.
- Israelachvili, J. N. 2010. *Intermolecular and surface forces*, Elsevier Science.
- James, R. O., Homola, A. & Healy, T. W. 1977. Heterocoagulation of amphoteric latex colloids. *Journal of the Chemical Society, Faraday Transactions 1: Physical Chemistry in Condensed Phases*, 73.
- Jennette, K., Lippard, S., Vassiliades, G. & Bauer, W. 1974. Metallointercalation reagents. 2-hydroxyethanethiolato (2, 2', 2''-terpyridine)-platinum (ii) monocation binds strongly to DNA by intercalation. *Proceedings of the National Academy of Sciences*, 71, 3839-3843.
- Jin, B. & Acrivos, A. 2004. Theory of particle segregation in rimming flows of suspensions containing neutrally buoyant particles. *Physics of Fluids*, 16, 641-651.
- Johnson, I. D. 2010. *The molecular probes handbook: A guide to fluorescent probes and labeling technologies*, Life Technologies Corporation.
- Karanikas, S. & Louis, A. A. 2004. Dynamic colloidal stabilization by nanoparticle halos. *Physical Review Letters*, 93, 248303.
- Kihira, H., Ryde, N. & Matijevic, E. 1992. Kinetics of heterocoagulation .1. A comparison of theory and experiment. *Colloids and Surfaces*, 64, 317-324.
- Kim, C. 2001. Migration in concentrated suspension of spherical particles dispersed in polymer solution. *Korea-Australia Rheology Journal*, 13, 19-27.
- Kim, J. M., Lee, S. G. & Kim, C. 2008. Numerical simulations of particle migration in suspension flows: Frame-invariant formulation of curvature-induced migration. *Journal of Non-Newtonian Fluid Mechanics*, 150, 162-176.
- Knipmeyer, K. M. & Pine, D. J. 2003. *Jamming and flow in concentrated suspensions*.
- Koh, C. J., Hookham, P. & Leal, L. 1994. An experimental investigation of concentrated suspension flows in a rectangular channel. *Journal of Fluid Mechanics*, 266.
- Kolli, V. G., Pollauf, E. J. & Gadala-Maria, F. 2002. Transient normal stress response in a concentrated suspension of spherical particles. *Journal of Rheology*, 46, 321.

- Krieger, I. M. 1972. Rheology of monodisperse latices. *Advances in Colloid and Interface Science*, 3, 111-136.
- Krishnan, G. P., Beimfohr, S. & Leighton, D. T. 1996. Shear-induced radial segregation in bidisperse suspensions. *Journal of Fluid Mechanics*, 321, 371-394.
- Lakowicz, J. & Hylden, J. 1978. Asbestos-mediated membrane uptake of benzo [a] pyrene observed by fluorescence spectroscopy.
- Lakowicz, J. R. 2007. *Principles of fluorescence spectroscopy*, Springer.
- Leighton, D. & Acrivos, A. 1987. The shear-induced migration of particles in concentrated suspensions. *Journal of Fluid Mechanics*, 181, 415-439.
- Liu, J. & Luijten, E. 2004. Stabilization of colloidal suspensions by means of highly charged nanoparticles. *Physical Review Letters*, 93, 247802.
- Lopez-Lopez, J. M., Schmitt, A., Moncho-Jorda, A. & Hidalgo-Alvarez, R. 2006. Stability of binary colloids: Kinetic and structural aspects of heteroaggregation processes. *Soft Matter*, 2, 1025-1042.
- Lyon, M. & Leal, L. 1998. An experimental study of the motion of concentrated suspensions in two-dimensional channel flow. Part 1. Monodisperse systems. *Journal of Fluid Mechanics*, 363, 25-56.
- Mccoy, D. & Denn, M. 1971. Secondary flow in a parallel plate rheometer. *Rheol. Acta*, 10, 411.
- Merhi, D., Lemaire, E., Bossis, G. & Moukalled, F. 2005. Particle migration in a concentrated suspension flowing between rotating parallel plates: Investigation of diffusion flux coefficients. *Journal of Rheology*, 49, 1429.
- Miller, R. M. & Morris, J. F. 2006. Normal stress-driven migration and axial development in pressure-driven flow of concentrated suspensions. *Journal of non-newtonian fluid mechanics*, 135, 149-165.
- Mladenovska, K., Cruaud, O., Richomme, P., Belamie, E., Raicki, R., Venier-Julienne, M.-C., Popovski, E., Benoit, J.-P. & Goracinova, K. 2007. 5-asa loaded chitosan–ca–alginate microparticles: Preparation and physicochemical characterization. *International journal of pharmaceutics*, 345, 59-69.
- Mohraz, A., Weeks, E. R. & Lewis, J. A. 2008. Structure and dynamics of biphasic colloidal mixtures. *Physical Review E*, 77, 060403.
- Moraczewski, T. & Shapley, N. C. 2006. The effect of inlet conditions on concentrated suspension flows in abrupt expansions. *Physics of Fluids*, 18, 123303.

- Moraczewski, T. & Shapley, N. C. 2007. Pressure drop enhancement in a concentrated suspension flowing through an abrupt axisymmetric contraction-expansion. *Physics of Fluids*, 19, 103304.
- Moraczewski, T., Tang, H. & Shapley, N. C. 2005. Flow of a concentrated suspension through an abrupt axisymmetric expansion measured by nuclear magnetic resonance imaging. *Journal of Rheology*, 49, 1409.
- Moreira, A. B., Dias, I. L., Neto, G. O., Zagatto, E. A. & Kubota, L. T. 2004. Solid-phase fluorescence spectroscopy for the determination of acetylsalicylic acid in powdered pharmaceutical samples. *Analytica chimica acta*, 523, 49-52.
- Morris, J. F. 2001. Anomalous migration in simulated oscillatory pressure-driven flow of a concentrated suspension. *Physics of Fluids*, 13, 2457.
- Morris, J. F. & Boulay, F. 1999. Curvilinear flows of noncolloidal suspensions: The role of normal stresses. *Journal of rheology*, 43, 1213.
- Nam, T., Park, S., Lee, S.-Y., Park, K., Choi, K., Song, I. C., Han, M. H., Leary, J. J., Yuk, S. A. & Kwon, I. C. 2010. Tumor targeting chitosan nanoparticles for dual-modality optical/mr cancer imaging. *Bioconjugate chemistry*, 21, 578-582.
- Narumi, T., See, H., Honma, Y., Hasegawa, T., Takahashi, T. & Phan-Thien, N. 2002. Transient response of concentrated suspensions after shear reversal. *Journal of Rheology*, 46, 295-305.
- Narumi, T., See, H., Suzuki, A. & Hasegawa, T. 2005. Response of concentrated suspensions under large amplitude oscillatory shear flow. *Journal of Rheology*, 49, 71-85.
- Pashley, R. M. & Israelachvili, J. N. 1984. Molecular layering of water in thin-films between mica surfaces and its relation to hydration forces. *Journal of Colloid and Interface Science*, 101, 511-523.
- Petit, L. & Gondret, P. 1992. Rectification of an alternating flow. *JOURNAL DE PHYSIQUE II*, 2, 2115-2144.
- Phillips, R. J., Armstrong, R. C., Brown, R. A., Graham, A. L. & Abbott, J. R. 1992. A constitutive equation for concentrated suspensions that accounts for shear-induced particle migration. *Physics of Fluids a-Fluid Dynamics*, 4, 30-40.
- Pine, D. J., Gollub, J. P., Brady, J. F. & Leshansky, A. M. 2005. Chaos and threshold for irreversibility in sheared suspensions. *Nature*, 438, 997-1000.

- Ponche, A. & Dupuis, D. 2005. On instabilities and migration phenomena in cone and plate geometry. *Journal of non-newtonian fluid mechanics*, 127, 123-129.
- Puertas, A. M., Fernandez-Barbero, A. & De Las Nieves, F. J. 2002. Kinetics of colloidal heteroaggregation. *Physica a-Statistical Mechanics and Its Applications*, 304, 340-354.
- Ramachandran, A. 2007. *The effect of flow geometry on shear-induced particle segregation and resuspension*. University of Notre Dame.
- Ramachandran, A. & Leighton, D. T. 2008. The influence of secondary flows induced by normal stress differences on the shear-induced migration of particles in concentrated suspensions. *Journal of Fluid Mechanics*, 603, 207-244.
- Ramachandran, A. & Leighton Jr, D. T. 2007. The effect of gravity on the meniscus accumulation phenomenon in a tube. *Journal of Rheology*, 51, 1073.
- Rao, R. R., Mondy, L. A. & Altobelli, S. A. 2007. Instabilities during batch sedimentation in geometries containing obstacles: A numerical and experimental study. *International Journal for Numerical Methods in Fluids*, 55, 723-735.
- Rao, R. R., Mondy, L. A., Baer, T. A., Altobelli, S. A. & Stephens, T. S. 2002. Nmr measurements and simulations of particle migration in non-newtonian fluids. *Chemical Engineering Communications*, 189, 1-22.
- Ravi Kumar, M. N. 2000. A review of chitin and chitosan applications. *Reactive and functional polymers*, 46, 1-27.
- Rosi, N. L., Giljohann, D. A., Thaxton, C. S., Lytton-Jean, A. K., Han, M. S. & Mirkin, C. A. 2006. Oligonucleotide-modified gold nanoparticles for intracellular gene regulation. *Science*, 312, 1027-1030.
- Sasaki, H., Matijevic, E. & Barouch, E. 1980. Heterocoagulation. Vi. Interactions of a monodispersed hydrous aluminum oxide sol with polystyrene latex. *Journal of Colloid and Interface Science*, 76, 319-329.
- Scheer, E. N. & Schweizer, K. S. 2008. Haloing, flocculation, and bridging in colloid-nanoparticle suspensions. *Journal of Chemical Physics*, 128, 164905.
- Singh, A., Nir, A. & Semiat, R. 2006. Free-surface flow of concentrated suspensions. *International journal of multiphase flow*, 32, 775-790.
- Sinha, V., Singla, A., Wadhawan, S., Kaushik, R., Kumria, R., Bansal, K. & Dhawan, S. 2004. Chitosan microspheres as a potential carrier for drugs. *International Journal of Pharmaceutics*, 274, 1-33.

- Stein, E. W., Volodkin, D. V., Mcshane, M. J. & Sukhorukov, G. B. 2006. Real-time assessment of spatial and temporal coupled catalysis within polyelectrolyte microcapsules containing coimmobilized glucose oxidase and peroxidase. *Biomacromolecules*, 7, 710-719.
- Stickel, J. J., Phillips, R. J. & Powell, R. L. 2007. Application of a constitutive model for particulate suspensions: Time-dependent viscometric flows. *Journal of Rheology*, 51, 1271.
- Stoll, S. & Pefferkorn, E. 1993. Kinetics of heterocoagulation. *Journal of Colloid and Interface Science*, 160, 149-157.
- Strasburg, G. M. & Ludescher, R. D. 1995. Theory and applications of fluorescence spectroscopy in food research. *Trends in Food Science & Technology*, 6, 69-75.
- Subia, S. R., Ingber, M. S., Mondy, L. A., Altobelli, S. A. & Graham, A. L. 1998. Modelling of concentrated suspensions using a continuum constitutive equation. *Journal of Fluid Mechanics*, 373, 193-219.
- Takka, S. & Acarturk, F. 1999a. Calcium alginate microparticles for oral administration: I: Effect of sodium alginate type on drug release and drug entrapment efficiency. *Journal of microencapsulation*, 16, 275-290.
- Takka, S. & Acartürk, F. 1999b. Calcium alginate microparticles for oral administration: Iii. The effect of crosslink agents and various additive polymers on drug release and drug entrapment efficiency. *Pharmazie*, 54, 137-139.
- Thanoo, B. C., Sunny, M. & Jayakrishnan, A. 1992. Cross-linked chitosan microspheres: Preparation and evaluation as a matrix for the controlled release of pharmaceuticals. *Journal of pharmacy and pharmacology*, 44, 283-286.
- Tirumkudulu, M., Tripathi, A. & Acrivos, A. 1999. Particle segregation in monodisperse sheared suspensions. *Physics of fluids*, 11, 507.
- Tohver, V., Chan, A., Sakurada, O. & Lewis, J. A. 2001a. Nanoparticle engineering of complex fluid behavior. *Langmuir*, 17, 8414-8421.
- Tohver, V., Smay, J. E., Braem, A., Braun, P. V. & Lewis, J. A. 2001b. Nanoparticle halos: A new colloid stabilization mechanism. *Proceedings of the National Academy of Sciences of the United States of America*, 98, 8950-8954.
- Tokumitsu, H., Ichikawa, H., Fukumori, Y. & Block, L. H. 1999. Preparation of gadopentetic acid-loaded chitosan microparticles for gadolinium neutron-capture therapy of cancer by a novel emulsion-droplet coalescence technique. *CHEMICAL AND PHARMACEUTICAL BULLETIN-TOKYO*, 47, 838-842.

- Tønnesen, H. H. & Karlsen, J. 2002. Alginate in drug delivery systems. *Drug development and industrial pharmacy*, 28, 621-630.
- Valioulis, I. A. & List, E. J. 1984. Collision efficiencies of diffusing spherical-particles - hydrodynamic, vanderwaals and electrostatic forces. *Advances in Colloid and Interface Science*, 20, 1-20.
- Van Soest, J. J. 2007. Encapsulation of fragrances and flavours: A way to control odour and aroma in consumer products. *Flavours and fragrances*. 439-455. Springer.
- Verwey, E. J. W. & Overbeek, J. T. G. 1948. The theory of the stability of lyophilic colloids. *Elsevier: Amsterdam*.
- Vesaratchanon, S., Nikolov, A. & Wasan, D. T. 2007. Sedimentation in nano-colloidal dispersions: Effects of collective interactions and particle charge. *Advances in Colloid and Interface Science*, 134-135, 268-278.
- Vincent, B., Young, C. A. & Tadros, T. F. 1978. Equilibrium aspects of heteroflocculation in mixed sterically-stabilised dispersions. *Faraday Discussions of the Chemical Society*, 65.
- Wang, Q. 1992. A study on shear coagulation and heterocoagulation. *Journal of Colloid and Interface Science*, 150, 418-427.
- Wiese, G. R. & Healy, T. W. 1970. Effect of particle size on colloid stability. *Transactions of the Faraday Society*, 66.
- Wiese, G. R. & Healy, T. W. 1975. Heterocoagulation in mixed $\text{tio}_2\text{-al}_2\text{o}_3$ dispersions. *Journal of Colloid and Interface Science*, 52, 458-467.
- Won, D. & Kim, C. 2004. Alignment and aggregation of spherical particles in viscoelastic fluid under shear flow. *Journal of non-newtonian fluid mechanics*, 117, 141-146.
- Xi, C. & Shapley, N. C. 2008. Flows of concentrated suspensions through an asymmetric bifurcation. *Journal of Rheology*, 52, 625.
- Yapici, K., Powell, R. & Phillips, R. 2009. Particle migration and suspension structure in steady and oscillatory plane poiseuille flow. *Physics of fluids*, 21, 053302.
- Yu, K., Ho, J., Mccandlish, E., Buckley, B., Patel, R., Li, Z. & Shapley, N. C. 2013. Copper ion adsorption by chitosan nanoparticles and alginate microparticles for water purification applications. *Colloids and Surfaces A: Physicochemical and Engineering Aspects*.

- Zanina, A., Vilesov, A. & Budtova, T. 2002. Shear-induced solvent release from gel particles: Application to drug-delivery systems. *International journal of pharmaceutics*, 242, 137-146.
- Zarraga, I. E., Hill, D. A. & Leighton Jr, D. T. 2000. The characterization of the total stress of concentrated suspensions of noncolloidal spheres in newtonian fluids. *Journal of Rheology*, 44, 185.
- Zhang, F., Long, G. G., Jemian, P. R., Ilavsky, J., Milam, V. T. & Lewis, J. A. 2008. Quantitative measurement of nanoparticle halo formation around colloidal microspheres in binary mixtures. *LANGMUIR*, 24, 6504-6508.
- Zubitur, M. M., Sudol, E. D., Dimonie, V. L. & El-Aasser, M. S. 2009. Monodisperse micron-size polymer core/nanoparticle pigment shell composite particles via heteroaggregation. *Journal of Applied Polymer Science*, 114, 264-274.